Dynamics of rotating suspensions in horizontal cylinders

by

Sudarshan Konidena

Submitted to the Department of Chemical Engineering
in partial fulfillment of the requirements for the degree of
Doctor of Philosophy
under the supervision of

Prof. Anugrah Singh and Dr. K. Anki Reddy

Department of Chemical Engineering
Indian Institute of Technology, Guwahati
India
781039
September, 2018

Abstract

The study of particle laden flows has been an area of interest in academia and industry alike owing to the applications across various areas. The flow of suspensions in simple geometries itself has complex nature due to several parameters like particle-particle interactions, fluid viscosity, etc. Suspensions are known to exhibit several intriguing phenomena such as shear-induced migration, axial pattern formation, among other phenomena. Another fascinating property of particle laden fluids is to form radial and axial patterns when rotated inside a horizontal cylinder.

Numerical simulations of positively buoyant suspension in a horizontally rotating cylinder were performed to study the formation of radial and axial patterns. The order parameter investigated for the low-frequency segregated phase and dispersed phase is similar to that predicted for the settling suspension by Lee and Ladd [J. Fluid Mech. 577, 183 (2007)], which is the average angular velocity of the particles. The particle density profiles for axial bands in the buoyancy-dominated phase shows an amplitude equivalent to the diameter of the cylinder. Axial density profiles show sinusoidal behavior for the drag-dominant phase and oscillating sinusoidal behavior for the centrifugal-force-dominant phase. Results also indicate that the traveling bands are formed as a consequence of the inhomogeneous distribution of particles arising from an imbalance among drag, buoyancy, and centrifugal forces. In the centrifugal limit, particles move towards the center of the cylinder, aggregating to form a dense core of particles with its axis coinciding with that of the rotating cylinder, a behavior which is in contrast to the sedimenting particles. The particle distribution patterns obtained from the simulations are found to be in good agreement with the experiments of Kalyankar et al. [Phys. Fluids 20, 083301 (2008)].

A similar kind of analysis is also performed for a bi-density system. We have studied the phase space, radial and axial patterns in settling as well as floating systems. Each system comprised of particle mixtures of two different densities. As many as eight unique phases are identified for each system along the radial plane. The bi-density system shows similarity to the mono-disperse case only when the radial distribution of the particles is completely uniform. Characteristic behaviour of the bi-density systems is identical at low rotation rates and contrasting when centrifugal force dominates. Expressing the phase boundaries in terms of dimensionless parameters $u_s/\Omega R$ and $g/\Omega^2 R$ gives a linear fit unifying the data in the gravity dominated regime. At high rotation rates, the behaviour is opposing for either systems though linear in nature. In the axial direction, number density profiles of both systems affirm the phenomenon of band formation. Location of the axial bands remains the same for heavy and light particles in both systems. We have also reestablished that an inhomogeneous particle configuration in the radial plane induces growing instabilities in the axial plane which amplify to form particle bands similar to mono-disperse suspensions.

The above two analyses are performed for dilute suspensions using a discrete particle method neglecting the finite sized effects of the particles and also incorporating only the far-field effects of the particle interactions. The Suspension Balance Model (SBM) is implemented to study the possibility of the formation of axial bands for

concentrated suspensions. We have obtained the axial banding phenomena for the experimental conditions of Kalyankar et al. [Phys. Fluids 20, 083301 (2008)] but with suspensions of higher concentration. These numerical simulations include the effect of the end-walls which are neglected in the discrete particle simulations indicate that the formation of axial bands might start because of interation of the suspended particles with the end-walls. Further studies with different particle radius may also be performed.

Acknowledgments

I wish to express my sincere thanks to my supervisors, Prof. Anugrah Singh and Dr. Anki Reddy. They have given me enthusiastic support, professional direction, and constant encouragement, and has inspired a novice like me to overcome the challenges on the road of life and study.

Particular thanks are extended to Dr. Jay Lee for his helpful discussions for this thesis work and also providing the basic source code for Stokesian dynamic simulation of settling suspension. I would also like to thank Mr. Shadab for providing the OpenFOAM based source code and helpful discussion on this thesis.

I am also grateful to our group members: Dr. Yadav, Mr. Bhaskar, Dr. Ashish, Mr. M. Mallikarjuna, Mr. Ajeeth Prabhu, Mr. Jyothi for their assistance in my work. I would also thank all the professors in the department who offered me endless discussions during my graduate studies. Without the assistance of my labmates I could not have completed this dessertation.

Finally, I would thank my family for their understanding, patience and unwavering support as they encouraged me to complete the thesis.

भारतीय प्रौद्योगिकी संस्थान गुवाहाटी
Indian Institute of Technology Guwahati

Contents

List of Figures

भारतीय प्रौद्योगिकी संस्थान गुवाहाटी
Indian Institute of Technology Guwahati

List of Tables

Chapter 1

Introduction

Pattern formations like periodically spaced ripples on sand or water, patterns on a basin floor, and Fibonacci patterns on leaves have been of interest to mathematicians, physicists, and researchers of various disciplines due to their omnipresence in nature. to the fundamental importance of particle suspensions, this has become an active area of research over the past two decades. Systems constituting of rigid spherical particles and a Newtonian fluid, in which the thermodynamic and the Brownian forces are inconsequential to consider form a model for the study of particulate flows. The dynamics of single particle motion is known with high precision but work on the collective behaviour of the particles in a suspension is yet to be completely understood. For the collective behaviour of particles, majority of the work that has been reported is on unbounded suspensions. A considerable amount of work has been done on the bounded suspensions in the recent studies through experiments on rotating cylinders, nevertheless, an adequate understanding on the theoretical aspects (along with numerical simulations) of the problems of this nature is yet to be accomplished. The progress that has been done on bounded suspensions is discussed below in little detail to give a basic understanding of the development so far and to justify the requirement for further evolution of work in the area. A horizontal rotating cylinder geometry is known to show various patterns even with pure fluids [43]. Another common phenomenon observed in the rotating cylinder geometry is that the particles segregate along the rotating axis. Both wet and dry granular media behave as complex fluids

showing an extent of similarity under certain conditions.

1.1 Dry Granular Matter

In the case of dry granular matter, axial segregation is observed when there is a difference in either density of the particles or size or both. Several studies performed in the radial and axial directions of the cylinder with dry granular particles reported various segregation patterns [45, 12, 6, 11, 4]. It is also understood that phenomena such as percolation (for size difference) and buoyancy (for density difference) are responsible for particles to segregate [15]. Fig. 1-1 shows the axial and radial patterns obtained by the flow of ternary granular mixtures in rotating cylinders. The particles in the mixture differ in size. It can be observed that an initially homogeneous mixture gets segregated in both radial and axial directions. In the radial direction, particles are seen to show core formation whereas along the axial plane band within band formation of the particles is evident.

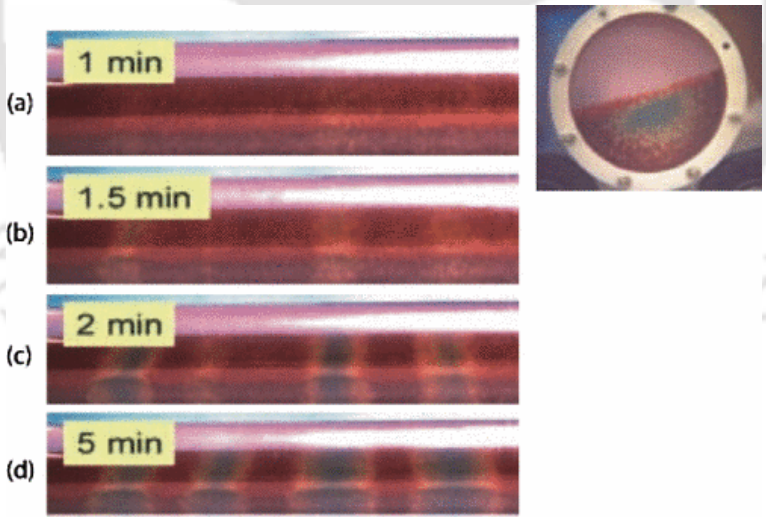

Figure 1-1: Radial and axial patterns of ternary granular mixtures in rotating cylinders at various instances showing the evolution of axial bands. Image adapted from [43]

These experiments revealed that the particles separate axially into a series of bands which were stacked along the horizontal axis. Hill et al. [46] were the first to report of a mysterious property of granular materials such as sand or powders. It

was about the tendency of the segregation of these mixtures even in situations when mixing was expected. They reported that the horizontal drum mixtures segregate the individual species present in the mixtures and that in cases of axial segregation, the components segregate into bands of relatively pure concentration along the axis of the cylinder (rotational axis). Their observations showed that if the rotational velocity is reduced, the components remix and the segregated state is restored when the rotational speed is increased again.

Hill et al. [11] used Magnetic Resonance Imaging (MRI) technique in their attempts to develop a complete and consistent description of the axial and radial segregation phenomena within the bulk of the material as it related to surface observations. It was thought that the above intriguing phenomena are due to the surface effects but they demonstrated that the segregation and remixing is more complicated in the inside of the surface that may intimidate the axial segregation. They analyzed images that were taken parallel and perpendicular to the cylinder prior to rotation and also after experiments were performed. These images demonstrated that the surface observations do not exactly the complexity of the segregation within the bulk. In a series of their experiments Jain et al. [15] observed that sometimes there were more axially segregated regions within the bulk of the suspension that could be visible from the surface which on prolonged rotation developed into bands and reached the surface. First, it supported their belief that the radial segregation occurs as the system attempts to minimize its compactivity. Then, it reinforced that the axial segregation may not exclusively be driven only by surface phenomena such as differences in the angles of repose as believed earlier. The segregation effect in the rotating drums may be a result of the fluctuations in the radially segregated small bead concentration within the bulk of the fluid. This segregation effect extends to the free surface.

In their subsequent work Hill et al. [11], as an extension to their initial work (Hill et al. [11]), analyzed the digital images taken of the surface segregation in conjunction with the subsurface measurements with the MRI technique. This analysis provided information of high significance about the details of the evolution of the surface pattern. Indications of interactions beneath the surface that drive the evolution

of bands were evident as the data from the surface segregation showed that a band merging event occurs which reiterated the presence of local mixing. At various rotational speeds, systematic studies of the pattern formation were done. These studies indicated that these subsurface interactions must fluctuate with the rotation speeds respectively. The initial conjecture that the subsurface dynamics drives the pattern evolution was supported by the MRI data results. Those MRI images revealed a relationship between the axial segregation and the radial segregation when the axial bands were merging. Hill et al. [44] also suggested future studies with the MRI technique to measure the velocity beneath the surface and within it so as to determine the mechanisms that would be responsible for the change in dynamics with rotation speed. Subsequently, other works which are briefed in table 1 aimed at understanding the mechanism responsible for the axial segregation phenomenon. When the granules differed by size, it was reported that percolation was the dominating effect to cause axial segregation. If the density difference or angle of repose are the parameters which vary among the granules then buoyancy is the driving mechanism for axial bands.

1.2 Suspension in Partially Filled Cylinder

Further, rimming flows of suspensions in the horizontal drum also displayed a tendency to segregate along the rotating axis [48, 47, 46, 16]. These experiments also put forth that in the presence of a free surface, all classes of particles i.e. sedimenting, neutrally buoyant and positively buoyant particles form axial bands. It is also reported that an increase in the concentration of the suspended particles considerably enhances the rate of band formation.[48] performed experiments with particles in the particle-laden rimming flow. They discovered that the particles initially showed a tendency to segregate. These particles were initially mixed so that they were uniformly distributed throughout the liquid. The banding patterns that were established took considerable time for low concentrated suspensions and appeared soon when the concentration of the particles in the suspension was high. The patterns that were observed after the experiments were equally spaced and successive. These patterns were

author	year	contribution
Hill and Kakalios	1994, 1995	performed experiments with glass beads and stated that axial segregation is reversible
Hong et al.	2001	studied the Brazil nut problem for bi-disperse particles in the radial plane
D.C. Rapaport	2002	applied DEM to study axial segregation and reported that percolation dominates
Fiedor and Ottino	2003	studied experimentally the coarsening of bands in square cross-section cylinder
Jain et al.	2005	investigated on bidisperse particles for combined size and density segregation
Alexander et al.	2004	the effects of particle size and tube diameter were investigated to provide scaling laws
D.C Rapaport	2007	investigated the effects of the length of the cylinder, angle of repose on axial bands
Juarez et al.	2010	investigated the patterns in wet conditions with an interstitial fluid (used water and NaI)
Inagaki and Yohsikawa	2010	experimented with 96% filled drum and observed stationary as well as travelling bands

Table 1.1: Literature for dry granular matter.

made up of particle rich regions separated by pure liquid (liquid devoid of particles).

In another independent study Tirumkudulu et al. [48] conducted experiments in a Taylor-Couette system. They partially filled the horizontal Taylor-Couette system with a suspension in which the suspended particles were neutrally buoyant. Subsequently Tirumkudulu et al.[48] reported that the segregation bands are not only pertained to the suspensions in which particles are denser than the fluid but are also observed when neutrally buoyant particles are suspended in a fluid. When conducting experiments using particles with density considerably lower than the carrier liquid it was understood that the band formation observed earlier by Tirumkudulu et al. [48] could develop into a compound structure. On close observations it was seen that the compound structure is an integration of three narrow secondary rings. These experiments also highlighted a waviness of the contact line in the homogeneous system. The observations from these experiments showed the equivalence in the wavelengths of the contact line deformation and the banding pattern. This waviness of the contact was also reported by Tirumkudulu et al. [47].

Thomas et al. [46] conducted experiments also by varying the sizes of the particles, the results depicted that the wavelength of the banding pattern is not related to the particle size. Tirumkudulu et al. [48] as a concluding remark of their work on the partially filled Taylor-Couette system mentioned that the cause for the phenomenon observed might be shear-induced diffusion. In their subsequent work too (Tirumkudulu et al. [48]) they were unable to identify an apt explanation to the mechanism observed but speculated that the reason could be the effect of the fluctuations of the local particle concentration on the local effective viscosity.

Study of the dynamics of suspensions consisting of micrometer and submicrometer particles holds many applications in industrial, and environmental avenues. For instance, polymer solutions,food processing, sedimentation phenomena and transport of particles etc. Systems constituting of rigid spherical particles and a Newtonian fluid, in which the thermodynamic and the Brownian forces are inconsequential to consider, form a model for the study of suspension dynamics. The dynamics of single particle motion is known with high precision but the collective behaviour of the

particles in a suspension is yet to be investigated for different flow geometries.

In another attempt, Raiskinmaki et al. [41] coupled the variable viscosity approach with direct numerical simulations to probe the formation of axial bands. From the Fig. 1-2 it can be observed that bi-disperse particle suspensions also display band within band phenomena similar to ternary dry granular mixtures. Govindarajan et al. [7] explained the observations of the experiments performed by Tirumkudulu et. al [48] using the concept of shear-induced diffusion of the suspended particles.

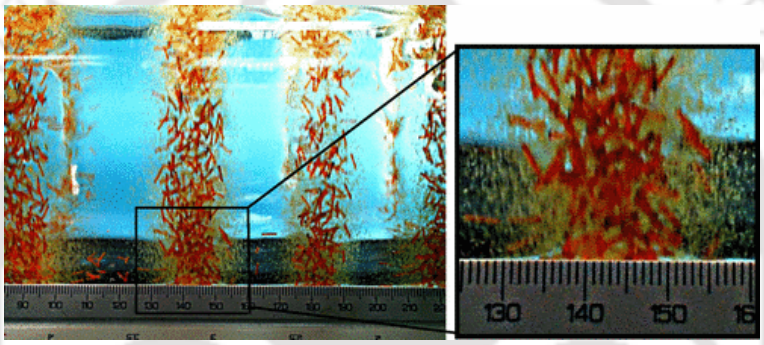

Figure 1-2: Band within band formation of bi-disperse particle suspensions in a partially filled cylinder. Image adapted from [43]

It is known that the particles experience the shear-induced migration phenomenon when there is a presence of gradients in viscosity, collision rate and flow curvature [40, 23]. In formulating a mathematical model, Govindarajan et al. [7] accounted for the flux due to gradient in particle volume fraction and gradient in deformation rate but the contribution of flux due to flow curvature was neglected. Though the shear-induced migration was studied in various geometries such as Couette cell [40, 44] in which particles usually migrate from high shear rate regions near the rotating inner-wall to low shear rate regions near the stationary outer-wall. In circular pipes [8, 9] and rectangular channels [20, 30, 31] in which the particles showed a tendency to migrate towards the centre of the pipe or the channel. More recently, Ramachandran and Leighton [42] showed through simulations that the second normal stress differences instigate secondary flows within the cross-section if the flow geometry is

author	year	contribution
Tirumkudulu et al.	1999	experimentally found out that suspensions in partially filled cylinders exhibit axial bands
Tirumkudulu et al.	2000	reported that the wavelength of the axial bands is equal to that of the deformed free surface
Timberlake and Morris	2002	studied the effect of gravity on axial bands using inclined cylinders,encountered travelling bands
Govindarajan et al.	2001	used shear induced migration of particles and the stability analysis to explain axial bands
Jin and Acrivos	2004	theoretically explained bands by inducing fluctuations in the effective local viscosity
Seiden et al.	2005	encountered a faint spatiotemporal movement of bands along the rotational axis
Guyez and Thomas	2008	reported rigorous spatiotemporal behaviour that emerges as the bands drift along the rotational axis
Guyez and Thomas	2009	identified eight different non-dimensional parameters to describe the travelling bands

Table 1.2: Literature for partially filled cylinders.

non-axisymmetric. Later, it was deduced by Zrehen and Ramachandran [51] that the secondary currents influence the particle migration in anisotropic geometries than the shear-induced self diffusion phenomena. However, not much work was performed to understand the phenomenon of shear-induced diffusion in fully filled horizontal rotating cylinders. Other works which aimed at investigating the axial banding phenomenon of suspension in partially filled cylinders are tabulated in table 2.

1.3 Suspension in Fully Filled Cylinder

The segregation mechanisms for the partially filled suspensions are governed strongly by the free-surface dynamics [16]. Nonetheless, dilute suspensions placed in rotating drums without the presence of a free surface exhibit axial particle bands as well [43]. To start, it is to be noted that most of the studies which explored the parameter space of the axial banding phenomenon for the case of fully filled cylinders were conducted with sedimenting particles. Lipson [28] reported alternating concentration bands of particles along the axial direction of the rotating cylinder. Experiments in [28] were directed at measuring the average spacing of bands as a function of the ratio of length and radius of the cylinder. Millimeter-sized particles which constitute the suspension are responsible for the high-particle-based Reynolds numbers ($Re_p = 2au_0/$ where a is the particle radius, u_0 is the settling velocity of an isolated particle, and is the kinematic viscosity of the carrying fluid) ranging from 6.5 to 735 in the experiments, whereas the effect of high rotational frequencies is reflected in the high-flow-based Reynolds number ($Re_f = \Omega R^2/$, where Ω is the rotational velocity of the cylinder and R is radius of the cylinder).

Breu et al. [2, 3] performed extensive studies with interstitial fluids having low viscosity and using glass beads as the suspended particles. These studies were performed at high rotational frequencies of the cylinder. They observed instabilities which highlight the hysteric character of the transition states as the rotational velocity is lowered. The axial bands also periodically expand and shrink along the axis depending on the rotation rate of the cylindrical drum. A particle-based Reynolds

number for the experimental conditions of Breu et al. [2, 3] is $Re_p \sim 20$, clearly implicating that inertia plays a significant role in band formation.

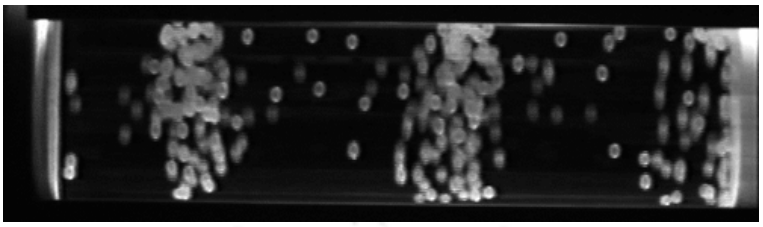

Figure 1-3: Axial banding phenomenon for mono-disperse particle suspensions in fully filled cylinders. Image adapted from [43]

Matson and co-workers [33, 35, 34] used various carrier fluids with viscosities in the range from 0.05 to 1 cm^2/s. A series of experiments were performed to identify the phase space of the various nonequilibrium states. For their experimental conditions, in the low rotational frequency limit and for various fluid viscosities, the particle-based Reynolds number Re_p should be < 0.1. Therefore, in this limit inertia is negligible, and without loss of generality one can apply the Stokes flow approximation. At low rotational frequencies, the alternate concentrated particle stripes were sinusoidal in nature, while at higher frequencies they were more pronounced but asymmetric. Lee and Ladd [25] proposed a theory to comprehend the underlying particle dynamics for the nonequilibrium patterns observed by Matson et al. [33]. They claimed that for a suspension of centrifuging particles, different centrifugal forces on particles at different radial positions produce an attractive interaction and relative motion between the particles along the axial direction. The relative motion between the particles in turn amplifies the axial density fluctuations, forming concentrated particle bands along the rotational axis. Their claim also suggests that for a suspension of non-Brownian buoyant particles, differential centrifugation produces a repulsive interaction between the particles which stabilizes any axial density fluctuations if present. Note that Lee and Ladd [25] approximated the canceling field of the cylindrical wall with a flat wall. However, it was later realized that the correct treatment of the no-slip cylindrical boundary condition should exactly nullify any interaction between ring Stokeslets due to differential centrifugation, which, therefore, cannot amplify any

axial density perturbation [26]. In their follow-up works [26, 27] Stokeslet simulations were used to reproduce the low-frequency patterns obtained in the experiments done by Matson et al. [33] and they reported that the axial banding might be a result of the secondary flow caused by sedimenting clusters during the dynamic phase transition in the radial plane. Motivated by the theory put forward by Lee and Ladd [25], Kalyankar et al. [18] conducted experiments with buoyant non-Brownian suspension and performed a comparative study with the settling suspension. Except for the densities of the suspended particles, most other parameters like the cylinder diameter, length, and particle sizes were similar to those used in Matson et al. [33, 35, 34]. These experiments with positively buoyant particles also showed evidence of axial banding. However, a mechanism for the above said system is not yet established.

A few more works were performed with suspensions in which the particles differ by size (henceforth referred to as bi-disperse suspensions). Introduction of particles of different properties into the same suspension generates a complex flow field due to the change in nature of particle-particle interactions. The experiments of Thomas et al. [1] and Joseph et al. [17] with bidisperse particles showed band within band phenomenon though in completely different flow regimes. The banding structure reported was finer in the experiments of Thomas et al.[1] as compared to the study of Joseph et al. [17] due to the prominence of centrifugal force in the flow regimes. Kumar and Singh [24] from their experiments using particles bi-dispersed by size showed that band formation occurs at much lower rotation rates than in partially filled cylinders. These experiments also evinced of band merging phenomenon where the number of bands decrease over long period of time after initial appearance. Recent developments on the theoretical front include the calculation of hydrodynamic forces on two different sized particles in a cylindrical tube to obtain the drag force and torque tensors [36], Stokesian simulations of two particles freely moving inside a cylinder by basis transformation method [37]. The aforementioned analyses do not reveal the flow field around the particles; however, Yao et al. [50] quantified the par-

author	year	contribution
Lipson	2001	measured band spacing as a function of cylinder dimensions
Breu et al.	2003,2004	observed both travelling and oscillating bands
Matson et al.	2003, 2005, 2008	extensively studied the phase space of sedimenting suspensions
Lee and Ladd	2002	concluded that only sedimenting particles form axial patterns
Raiskinmaki et al.	2003	reported that at higher Re the particle clusters break down and shows shear thickening
Seiden et al.	2005, 2007	reported travelling bands for larger particle suspension with inertial effects
Lee and Ladd	2005,2007	modelled particles as Stokeslets and deduced that radial perturbation amplifies bands
Kalyankar et al.	2008	obtained the phase space for floating particle suspension and reported travelling bands
Thomas et al.	1999	observed fine structures of band within band phenomenon for bi-disperse suspension
Joseph et al.	2003	obtained coarse bands with bidisperse suspension in centrifugal force dominated regime
Kumar and Singh	2010	reported that for bidisperse suspensions bands form at much slower rate

Table 1.3: Literature for Fully filled cylinders.

ticle interactions and provided a detailed flow field around the neighborhood of two particles using the method of reflections. Investigations with more number of particles in the cylinder were performed by Pesche et al. [39] by including hydrodynamic interaction of the particles. This method predicted the shear induced migration of particles with considerable accuracy in a two dimensional Taylor-Couette flow. Jain et al. [14] successfully employed Stokesian dynamics to compare radial segregation at low rotational speeds of the cylinder with experimental results. Though there are various industrial applications to the rotating flow of bi-density suspensions in horizontal cylinders, it can be seen that the knowledge of the characteristics of various phases a suspension could experience is yet to be explored. Therefore, it is evident that the suspension system in which the particles differ in their properties should be more comprehensively addressed owing to its vast areas of application.

From the literature tabulated in table 3, one get understand that the contributions in the dynamics of suspensions in rotating cylinders clearly identifies the areas which are yet to be comprehensively understood. Primarily, an explanation for the radial and axial patterns exhibited by a positively buoyant suspension is lacking. Secondly, not much experimental or simulation work was devoted to explore the dynamics of suspension in which the particles differ by density (henceforth referred to as bi-density suspension). Finally, most of the investigations performed in the case of fully filled cylinders belong to the dilute suspension limit. Effect of higher concentrated suspensions and the possibility of migration of the suspended particles by secondary flows or shear-induced self diffusion is yet to be explored. The objective of the current thesis work is to address each of the above three discussed problems, therefore the thesis is organized in the following manner. In the proceeding chapter, the methodology applied to simulate the horizontal rotating suspension is detailed. A discrete particle method based on point particle approach at very low Re which could be used to simulate a horizontal rotating suspension is described. Chapter 3 discusses in detail the radial and axial patterns formed for a mono-disperse positively buoyant suspension rotating in a horizontal cylinder. In Chapter 4, the dynamics of a bi-density suspension along with scaling relations for the phase transitions is

presented. Chapter 5 deals with the CFD simulations of a concentrated positively buoyant suspension rotating in a horizontal cylinder based on the Suspension Balance Model (SBM) proposed by Nott and Brady [38]. Ultimately, in Chapter 6 conclusions of the present work and future perspectives are discussed.

Chapter 2

Simulation Methodology

This chapter contains the details of the methodology followed to simulate the monodisperse and bi-density particle suspensions in a horizontal rotating cylinder. This method which approximates the suspended particles as point sized was proposed by Lee and Ladd [27]. The suspension under the experimental conditions of Kalyankar et al. [18] comprised of monodisperse hard spheres distributed in a viscous fluid. This suspension supposedly fills completely a cylinder which is held horizontal and rotated with a very low angular velocity. The radius of the rotating drum $R \sim 100a$, where a is the radius of an isolated rigid sphere. Due to the above said conditions, most of the phases exhibited by the systems fall in the Stokes flow regime.

Therefore we start by considering the situation of particles suspended in an incompressible Newtonian fluid in the Stokes (creeping) flow regime. In this formulation, each suspended particle is assumed to be point sized and there is a total of N such particles in the cylindrical domain. A representation of the particles suspended in a horizontal cylinder is shown in the schematic diagram below.

It is well known that the Navier-Stokes equations govern the fluid motion whereas the motion of the particle is given by the N-body Langevin equation as written below.

$$m\frac{dU}{dt} = F^H + F^P + F^B \tag{2.1}$$

The above equation is simply a form of the Newtons second law of motion. The

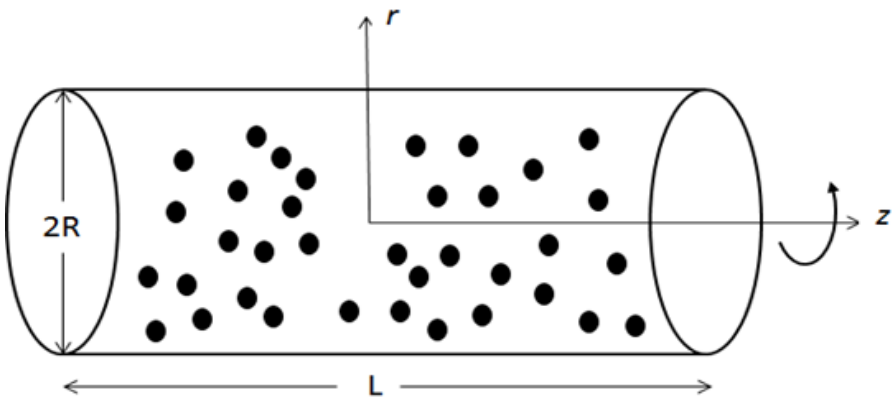

Figure 2-1: Schematic diagram of particles in a horizontal rotating drum

forces included in the equation are hydrodynamic, inter-particle or external, and Brownian forces. However, in the present model since the fluid is Newtonian and sufficiently viscous the inertial forces are neglected. The particles are assumed to be large enough to bypass any effects due to Brownian forces. The hydrodynamic forces are limited to only far-field effects since the suspension is assumed to be very dilute. The ratio of the particle radius (a) to the cylinder radius (R) was 100 in all the simulations.

In a rotating frame of reference which is rotating with an angular velocity Ω the term $\frac{d\boldsymbol{U_i}}{dt}$ is written as

$$\frac{d\boldsymbol{U_i}}{dt} = \frac{d\boldsymbol{U_i}}{dt}_{rot} + 2\Omega \times U_i + \Omega \times (\Omega \times r) \tag{2.2}$$

The above modified equation includes the effect of centrifugal and Coriolis forces which arise due to rotation. Other forces which influence the particle are gravitational force and a drag force which is dependent on the configuration of the particles in the neighbourhood. The drag force is an results from the summation of the fluid stress on the surface of the particle.

In a non-rotating frame, the equation of motion is a balance of the inertial forces,

gravitational forces and drag which is given as,

$$m\frac{d\boldsymbol{U_i}}{dt} = m\boldsymbol{g} + \int\int \sigma d\boldsymbol{s_i} \tag{2.3}$$

On including the effects of rotation, and accounting for the effect of buoyancy by correcting the mass as $m_B = V(\rho_f - \rho_p)g$ the above equation transforms to

$$m\frac{d\boldsymbol{U_i}}{dt} + 2m\boldsymbol{\Omega} \times \boldsymbol{U_i} = m_B\boldsymbol{g} + m_B\boldsymbol{\Omega} \times (\boldsymbol{\Omega} \times \boldsymbol{r_i}) + \int\int \sigma d\boldsymbol{s_i} \tag{2.4}$$

where, m_B is the buoyancy corrected mass given by $m_B = (\rho_f - \rho_p)Vg$; V being the volume of the spherical particle; σ is the fluid stress.

From the experimental conditions of Kalyankar et al. (2008) the inertial forces are negligible compared to the gravitational or centrifugal forces experienced by the particles. Since the Coriolis force is a form of inertial force even it is neglected. On neglecting the inertial forces the equation (2.4) becomes

$$m_B\boldsymbol{g} + m_B\boldsymbol{\Omega} \times (\boldsymbol{\Omega} \times \boldsymbol{r_i}) + \int\int \sigma d\boldsymbol{s_i} = 0 \tag{2.5}$$

The viscous forces term in the above equation can be written as $\xi[\boldsymbol{U} - \boldsymbol{u}(\boldsymbol{r})]$, where $\xi = 6\pi\eta a$ is the friction coefficient. In the rotating frame of reference, the term $\boldsymbol{u}(\boldsymbol{r})$ = 0 for a single particle. However, in a fixed frame of reference $\boldsymbol{u}(\boldsymbol{r}) = \boldsymbol{\Omega} \times \boldsymbol{r}$. Finally, the equation (2.4) is reduced to a balance between the gravitational, centrifugal and viscous forces acting on a single particle as given by the equation (2.5).

$$\boldsymbol{F} = m_B\boldsymbol{g} + m_B\Omega^2\boldsymbol{r} = \xi[\boldsymbol{U} - \boldsymbol{u}(\boldsymbol{r})] \tag{2.6}$$

where $\xi = 6\pi\mu a$, $\boldsymbol{U}$ is the particle velocity and $\boldsymbol{u}(\boldsymbol{r})$ is velocity of the fluid at particle location $\boldsymbol{r}$. It is evident from equation (2.5) that for a point particle the viscous, gravitational and the centrifugal forces govern the motion. The detailed procedure to calculate the particle velocities is provided in the Appendix. This procedure follows from the method elaborated in [10] for the wall effects on the motion of a single particle bounded by a circular cylindrical wall.

2.1 Single Particle Dynamics

A positively buoyant particle placed in a viscous fluid which rotates along its horizontal axis experiences a buoyancy corrected gravitational force and a centrifugal force given by $m_B g\hat{\boldsymbol{y}}$ and $m_B \Omega^2 r\hat{\boldsymbol{r}}$ respectively. These forces cause the particle to rise with a velocity $u_f\hat{\boldsymbol{y}}$ and a centrifuging velocity $u_c\hat{\boldsymbol{r}}$, where $u_f = m_B g/\xi$ and $u_c = m_B\Omega^2 r/\xi$. The velocity of the isolated particle could be obtained on solving the instantaneous force balance equation. Let us consider a single particle held in a viscous fluid rotating in a horizontal cylinder. The motion of this particle is effected by three forces namely; gravitational, centrifugal and viscous drag. The buoyancy corrected mass of the particle $m_B = \pm(\rho_p - \rho_f)g$ changes sign depending on whether the system is settling or otherwise. The particle settling/floating velocity due to density difference between the particle and the fluid is $\pm(-U_s\hat{\boldsymbol{y}})$ where, $U_s = m_B g/(6\pi\mu a)$. Action of centrifugal force on the particle gives rise to centrifuging velocity $U_c(r/R)\hat{\boldsymbol{r}}$ where, $U_c = m_B\Omega^2 R/(6\pi\mu a)$. On resolving these velocities into the (r, θ) coordinate systems, we obtain the following expressions.

$$u_r = u_c(r/R) + u_f sin\theta \tag{2.7}$$

$$u_\theta = \Omega r + u_f cos\theta \tag{2.8}$$

On further simplification, we will have

$$u_r = u_f[(u_c/u_f)r/R + sin\theta] \tag{2.9}$$

$$u_\theta = u_f[(\Omega R/u_f)r/R + cos\theta] \tag{2.10}$$

From the above two equations, we can now define two dimensionless numbers D_1 and D_2 which describe the relative magnitude of the three forces gravitational, centrifugal and viscous drag acting on the particle. On substituting the dimensionless numbers

$D_1 = u_f/u_c = g/\Omega^2 R$ and $D_2 = u_f/\Omega R$ into the above equations we finally obtain,

$$u_r = u_f[r/(D_1 R) + sin\theta] \tag{2.11}$$

$$u_\theta = u_f[r/(D_2 R) + cos\theta] \tag{2.12}$$

Trajectories on which the radial and the angular velocities become zero for the particle under consideration can be obtained by equating u_r and u_θ to zero. The loci so obtained are circles with diameters $D_1 R$ and $D_2 R$ as shown in Fig. 2-2(a) which henceforth are referred to as C_1 and C_2. A particle which usually migrates along with the stream velocity goes against it in the circle C_2, this happens because the upward Stokes drag is large enough to overcome the gravitational force. Likewise, a particle usually moves towards the cylinder wall but inside the circle C_1, it migrates towards the central axis as the centrifugal force adds to the Stokes drag. The circles C_1 and C_2 intersect at a point denoted as P. The point P signifies balance of all three forces acting on the particle implicating an unstable equilibrium. If the particle is initially placed near this point, it spirals inwards ending up with a limiting closed trajectory determined by the strength of the centrifugal force. Thus P could well be a dynamical centre of this system. The limiting trajectories for the particle can be easily determined from the diameters of these circles within the rotating cylinder. If $D_1 > 1$ as shown in Fig. 2-2(b), a particle directly moves towards a point of stagnation A (upper intersection point of circle C_2 with the cylinder wall) i.e., that particle is devoid of having a closed trajectory.

The above critical observation implicates that the condition $D_2 = 1$ might establish a bound to the angular velocity of the cylinder in order for the suspension to be homogeneous in the radial plane. At lower angular velocities the centrifugal force is overcome by the drag force and consequently the particle stagnates at a fixed point. Correspondingly, for a dilute suspension rotating at low rotational velocities ($D_2 > 1$), the particles will flock as a pack near this point. This conglomeration of particles around the stagnation point needs larger angular velocities to be mobilised,

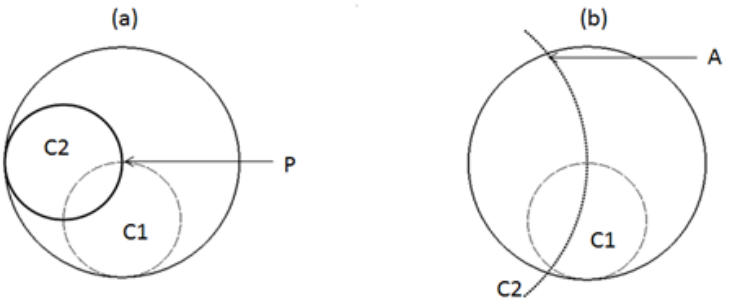

Figure 2-2: The circles C_1 and C_2 describe the locus of zero radial and angular velocities, respectively. Panel (a) corresponds to the drag dominant phase with the point P indicating the dynamical center of the system, and panel (b) corresponds to centrifugal dominant phase; here the point A indicates the stagnation point.

therefore a lesser critical value of D_2 is expected. Experimental conditions under which band formation was reported have their $D_1 \sim 10^3$ and $D_2 \sim 0.01$ i.e., the Stokes drag is much larger than the centrifugal force when $D_1 \gg 1$, but much smaller than the centrifugal force exerted by the rotating fluid if $D_2 \ll 1$.

Since the circle C_1 has a large radius compared to the circle C_2, the upper point of intersection of the circles (unstable equilibrium) is placed almost at the centre, i.e.

$$r(P) = (D_2 R)\hat{x} + O(D_2^2 R/D_1)\hat{y}, \tag{2.13}$$

then the velocity of a particle relative to the stream is given by,

$$\frac{v}{\Omega R} = \frac{u - \Omega r\hat{\theta}}{\Omega R} = D_2(\frac{r}{D_1 R} - \hat{y}), \tag{2.14}$$

has a small centrifuging component in addition to the much larger rising velocity.

On increasing the rotational velocity, the circular orbit is perturbed by the strong centrifugal velocity and the particle eventually approaches the limiting closed trajectory, but with a very long time scale $\sim \frac{D_1}{D_2\Omega}$. These considerations suggest that for the purpose of determining the onset of the axial instability, it will be sufficient to assume that the suspension is homogeneous in the transversal plane, which is in fact consistent with the experimental observations. In lieu of the above arguments and from Fig. 2-2 and Fig. 2-3, it is justified to divide the segregated phases into

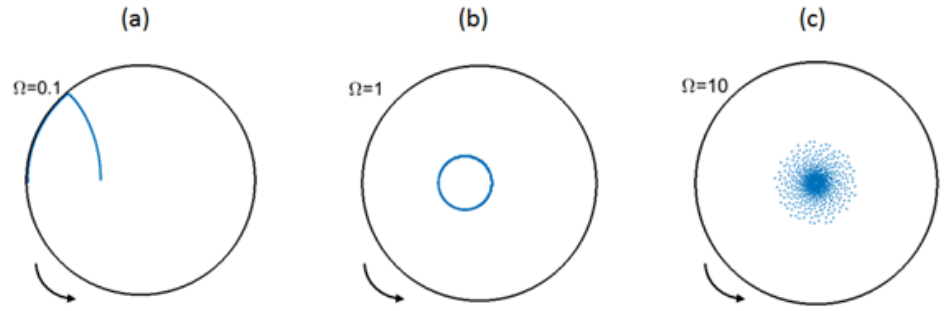

Figure 2-3: Particle trajectories at different velocities of the cylinder rotating counter-clockwise as indicated by the arrow. Initial position of the particle in all three cases is $(r, \theta, z) = (0.5, 0, 0)$. (a) $\Omega = 0.1\ rad/s$: drag dominant regime, the particle rises to reach the cylinder and gets dragged down because of rotation (b) $\Omega = 1\ rad/s$: balance of gravity, drag and centrifugal forces imposing a closed trajectory to the particle (c) $\Omega = 10\ rad/s$: centrifugal force dominant regime, the particle swirls inward to the centre.

a) buoyancy dominated b) a balance between buoyancy and centrifugal forces and c) centrifugal force dominating regime. Experimental results are in tandem to the above observation as the homogeneous phase occurs in between two different phases which exhibit axial banding.

2.2 Stokeslets confined in a cylinder

Having understood the behaviour of a single particle in a rotating cylinder, the actual interest in suspension dynamics lies in comprehending the collective behaviour of particles constituting the suspension. Starting from the fundamental solution for Stokes flow termed as the Stokeslet, we can construct a general solution for the dynamics of N-Stokeslets confined in a cylindrical boundary. A schematic representation of the cylinder fully filled with a suspension is shown in Fig. 2-1, with its rotational axis aligned along the z-axis. Fig. 2-4 gives the schematic of a particle generating Stokeslets (the source field and the cancelling field). An exact mirror image of the source satisfies the no-slip condition imposed on the wall of the rotating cylinder. For a multi-particle system, the hydrodynamic interactions between Stokeslets give rise to perturbations in the flow field which result in additional contributions to the

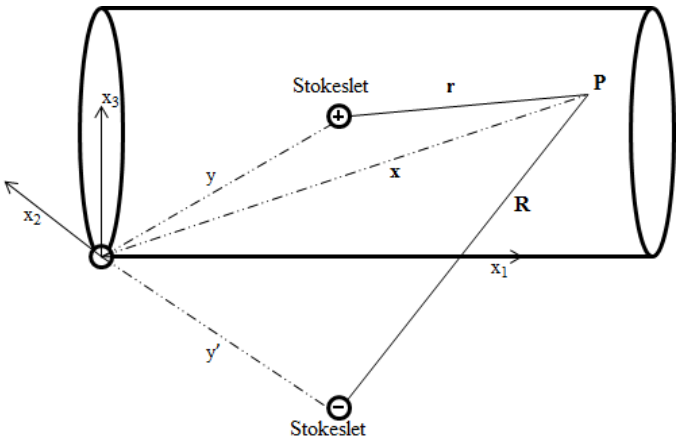

Figure 2-4: Image system for the source field and the cancelling field in a cylinder

particle velocities. This resultant flow field due to the presence of a point force $\boldsymbol{F}$ at $\boldsymbol{r_0}$ is

$$\boldsymbol{u}(\boldsymbol{r}) = \boldsymbol{G}(\boldsymbol{r}, \boldsymbol{r}_0).\boldsymbol{F} \tag{2.15}$$

$\boldsymbol{G}(\boldsymbol{r}, \boldsymbol{r}_0)$ is the Green's function of Stokes flow due to the presence of Stokeslet in an unbounded cylindrical domain. To calculate the perturbations due to the presence of a number of Stokeslets bounded by a cylindrical boundary, one needs to evaluate the Green's function for the flow field bounded by a cylinder of infinite length. Lee and Ladd [27] evaluated expressions for the Greens function for N-Stokeslets starting from the Fourier-Bessel expressions provided by Liron and Shahar[29] for an isolated Stokeslet in a cylinder. Lee and Ladd [27] also showed through their simulations that the Fourier-Bessel type expression is more suitable for a periodic system along the axial direction while a residual sums method would be more suitable for a tube of infinite length. On evaluation of the Green's function, the particle velocity can be bifurcated corresponding to the contributions from the hydrodynamic interactions and the Stokes velocity. Hydrodynamic interactions are a result of essentially the inter-particle interactions and due to the presence of the cylindrical boundary.

$$u_j = \frac{\boldsymbol{F_j}}{\xi} + \sum_{i \neq j} \boldsymbol{G}(r_j, r_i).\boldsymbol{F_i} \tag{2.16}$$

Neglecting the Stresslets and other higher order contributions to the force density

on the particle surface eases the computational effort and allows us to simulate 10^4 particles in most of the cases. Eq. (2.9) is valid in the experimental conditions of Kalyankar et al. [18] as the suspension is very dilute allowing the mean inter-particle distance to be large compared to the particle size. The simulations make use of a Runga-Kutta method to determine the particle positions. An image system is essential to fulfil the no-slip boundary condition on the cylindrical domain binding the suspension. Lee and Ladd [27] constructed expressions for the additional flow field generated by the no-slip condition on the surface of the cylinder and used the general solution of the Stokes equations for a cylindrical geometry in the construction of Fourier-Bessel coefficients. The overall velocity field $u(r)$ can be divided into a source field $v(r)$ and a cancelling field $w(r)$ which can be independently calculated and the cancelling field also satisfies the equation $w(R) = -v(R)$ at every point on the surface of the cylinder.

The source field consists of nine components v_β^α corresponding to the three directions of the Stokeslet α and three directions of the velocity β, here α and β are components (r, θ, z) in cylindrical coordinates. The coordinate system of Liron and Shahar [29] had its origin situated at the Stokeslet as the prime interest was in the flow field due to one Stokeslet, but for an N-particle case this form of a coordinate system is not conducive. Therefore, expressions are evaluated after transforming them into the usual cylindrical coordinate system. The source field *v(r)* and the canceling field *w(r)* can be independently evaluated to calculate the overall velocity field by imposing a no-slip velocity boundary condition at all points on the surface of the cylinder. Thereby, at every point on the wall of the rotating cylinder the canceling field satisfies the equation $w(R) = -v(R)$. The source field consists of nine components (v_α^β) corresponding to the three directions of the Stokeslet α and three directions of the velocity β; here α and β are components (r,θ,z) in cylindrical coordinates. In order to ease the computational effort, Stresslets and higher order multipole contribution to the force density on the particle surface are neglected.

Liron and Shahar (1978) provided two alternative expressions for the velocity field due to the presence of a Stokeslet in a pipe. One as a doubly infinite sum

of residues and the other in terms of Fourier-Bessel expansion. Though the doubly infinite sum of residues is an exponentially decaying series, it is more suitable for studies where the cylinder is of infinite length. The Fourier-Bessel sum is effective in handling periodically bound systems. The Fourier-Bessel expression determines the unbounded fluid velocity and the additional reflected velocity field independently, thereby reducing the computational cost to scale with the number of particles N (the doubly infinite residues scales as N^2). The computer code divides the Fourier-Bessel sum among 16 processors (typically) and can simulate a few hundreds of rotations of the horizontal cylinder with ≈ 12000 particles in about a week's time. This Fourier-Bessel sum related algorithm for N particles in a cylinder was first developed originally by Lee and Ladd (2007).Further details regarding the issues of numerical convergence, number of Fourier modes required for convergence, etc. are provided in [27]. The expressions for the components of the velocity thus evaluated are used to study the dynamics of dilute suspensions in horizontal rotating cylinders. The derivation of these expressions is given in the Appendix of the current thesis as mentioned earlier.

Throughout all chapters in the thesis the size of the particles constituting the suspension is 100μ unless mentioned otherwise (a few simulations consist of particles with 50μ and 200μ). The velocity of a positively buoyant particle rising in a fluid of viscosity 55cP (in all simulations except for DB and CL phases where it is 80cP) is calculated using the formula $u_f = 2(a^2\Delta\rho g)/9\mu$. The value of the velocity thus calculated is $u_f = 0.0373\ cm/s$. Density of the particle used in the simulations is 0.30 g/cc. Two Reynolds numbers are defined in the work $Re_p = \rho_p a u_f/\mu$ and $Re_f = \rho_f \Omega R^2/\mu$ which correspond to particle and flow based Reynolds numbers. The value of Re_p is determined to be 0.002 and the flow Reynolds number ranges from 0.18 to 41 dependent on the rotational velocity.

From the above details it is clear that the parameter space of most of the phases studied in the work falls into the Stokes flow limit. With the above detailed method the behaviour of a positively buoyant suspension in rotating cylinder is investigated and analysed in Chapter 3, then the phase space of a bidensity suspension is explored in Chapter 4.

Chapter 3

Particle dynamics and pattern formation in a rotating suspension of positively buoyant particles

3.1 Motivation

Numerical and experimental works which dealt with the case of a mono-disperse suspension in a horizontal rotating cylinder were mainly concerned with the suspended particles to be sedimenting. In order to provide a theory for the experimental observations of [33] with sedimenting particles, Lee and Ladd [25] stated that settling particles always have an attractive motion while sedimenting thus forming clusters. Intuitively, the claim also supposed that if the particles are buoyant then there would be a repulsive motion between the particles which would hinder any cluster formation. Motivated by this theory, Kalyankar *et al.* [18] conducted experiments with buoyant non-Brownian suspension and performed a comparative study with the settling suspension. Except for the densities of the suspended particles, most other parameters like the cylinder diameter, length, and particle sizes were similar to those used in Matson et al. [33, 35, 34]. It was found from their experiments that when the action of gravity overcomes centrifugal forces, nonequilibrium states for the buoyant and the

settling suspensions can be correlated. Reference [18] used glycerine-water mixtures as the carrier fluid with kinematic viscosities ranging from 0.25 to 1 cm^2/s.

3.2 Numerical Method and Simulation set-up

In the case of multiparticle dynamics, the hydrodynamic interactions also play a role in addition to the forces detailed in single-particle dynamics. Since the interest lies in comprehending the collective behavior of particles in the suspension, the additional contribution to the particle velocities from interactions is incorporated. The approach followed to understand collective particle dynamics is similar to the molecular dynamic simulation. First, the particle positions are initialized using a Monte Carlo method to generate random initial configuration for the particles. The initial configuration is generated by maintaining the volume fraction of the particles $\phi \sim 0.2$ pertaining to the experimental conditions. In the second step the velocity field for the system is computed from Eq. (2.16); this is done by approximating the particles as Stokeslets and summing up with the flow field due to the cylinder surface. Finally, from the knowledge of the particle velocities a fourth order Runga-Kutta method is used to solve the differential equation so that the new positions of the particles are determined. This process is looped over until a steady state configuration is reached. All the simulations irrespective of the value of L/R have the axially periodic boundary condition imposed in the present work.

The simulation parameters used in this study are tabulated in the table given below.

3.3 Results and Discussion

Our simulations were inspired by the experimental results in Ref. [18]. Therefore, the parameters necessary for the simulations were maintained similar to the conditions of their experiments. In our simulations the particle radius a was $100\mu m$ and the

parameter	Symbol	Value
cylinder radius	R	$1.0cm$
particle radius	a	$0.01cm$
particle density	ρ_p	$0.30g/cc$
fluid density	ρ_f	$1.16g/cc$
fluid viscosity	μ	$55cP$ (80 cP for DB/CL)
cylinder length	L	$0.2cm$ radial, $5cm$ axial
number of particles	N	2300 radial, 12465 axial

Table 3.1: Simulation parameters used in the study.

radius of the cylinder (R) was $100a$. The length of the cylinder (L) for radial and axial segregation studies was 0.2R and 5R, respectively. The fluid viscosity () was $55cp$ (except for Discontinuous Banding (DB) and Centrifugal Limit (CL) phases, which was 80 cp), and its density (ρ_f) was 1.16 g/cc. The particle density (ρ_p) in all but one simulation was 0.15 g/cc. Simulations were performed for various rotational frequencies (Ω). The flow Reynolds number ($Re_f = \rho\Omega R^2/\mu$) varied between 0.18 (for GB case) to 41 (for the CL case). Kalyankar et al. [18] observed as many as nine independent steady states, which can be distinguished by the exhibition of various radial and axial patterns. It is to be noted that in their experiments for recording observations in the radial plane a shorter cell with a diameter 1.97 cm but with a length of 2.25 cm was used corresponding to the average length of a single band observed in the studies of axial pattern in much longer cylinders. Starting from the Granular Bed (GB) phase to the CL phase, both the settling and buoyant systems contain a large array of identical properties and phases. Our simulations could reproduce most of the phases observed in the experimental results. In the discussion below, radial and axial segregation patterns obtained from simulation results are presented exclusively.

3.3.1 Radial Patterns

Several patterns distinct in the radial plane occur for different rotational rates of the cylinder. Simulations performed could reproduce most of the patterns that form in the radial plane for a buoyant suspension. To observe radial patterns, a cylinder with

R = 1cm and L = 0.2R (to nullify axial density variations) is considered with around 2300 particles; the fluid viscosity is maintained at 55 cP at all times, but for DB and CL phases the viscosity was 80 cP. The density of the fluid and particles were taken to be 1.16 g/cc and 0.15 g/cc respectively. The discussion below details the steady state dynamics of the particles for a wide range of rotation rates which fall into the three regimes as discussed in Chapter 2.

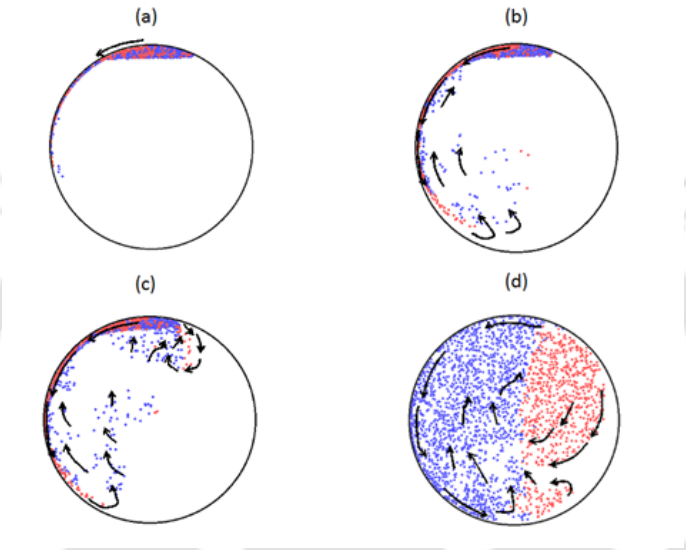

Figure 3-1: Velocity vectors and particle distribution at steady state for a buoyancy-dominated regime. Red particles move downwards, whereas the blue particles move against gravity. (a) $\Omega = 0.09\ rad/s$, particles form a bed at the top (GB); (b) $\Omega = 0.12\ rad/s$, particles which are dragged along the cylinder tend to rise (F1); (c) $\Omega = 0.15\ rad/s$, more particles are dispersed into the cylinder (F1/F2); (d) $\Omega = 0.3\ rad/s$, particles transit into the right half of the cylinder (LT)

Granular Bed

At very low rotational frequencies of the cylinder, the particles are stacked near the upper section of the cylinder forming a bed as shown in Fig. 3-1(a). This bed formation is because the dominant force in this phase is the buoyancy. As the cylinder rotates, particles from the bed are carried down along the rotating wall in a thin layer which has a thickness equivalent to the diameter of the suspended particles. At a certain downward location the vertical component of the viscous drag is overcome by the upward buoyancy force, and the particles rise back into the bed with a much

higher rising velocity. As the particles are dragged upwards by the buoyant force they set a clockwise current near the bed. It is evident from Fig. 3-1(a) that GB for the floating system is similar to that of the settling system (Fig. 3-4(a) in Lee and Ladd [27]), which is because the effective direction of bed formation is reversed.

Fingering Flow I (F1)

As the rate of rotation of the cylinder is slightly increased one can observe the elongation of the tail of GB with not much change in the properties of the bed. There is a decrease in the concentration of particles in the bed since more particles get dragged along the wall of the cylinder. The particles which are dragged down along the wall begin to move towards the bed once they reach near the bottom of the cylinder. The particles are dragged downward along the rotating wall till the point where the vertical component of the drag force is greater than the buoyancy force. Near the bottom of the cylinder the buoyancy force overcomes the drag, and the particles escape from the downward velocity imposed by the wall. The rising particle drags its neighboring particles as it passes through the fluid. The region of the circulating counter currents which started to grow in the GB phase develops further in this phase owing to the increase in the rotational frequency as shown by the velocity vector plot in Fig 3-1(b). The F1 phase too is identical to that of the settling suspension.

Fingering Flow II (F2)

The F2 phase appears at slight higher velocities from F1; in this phase the particle distribution can be divided into three zones based on the circulation currents in the cylinder. It is evident from the particle distribution in Fig 3-1(c) that the flow is clockwise to the left of the rotating axis as the particles that get detached from the wall tend to float back to the top. As there is no presence of particles to the right of the rotating axis, the fluid follows the course of the cylinder wall and imparts a counter-clockwise flow. These opposite currents in the left and right sections if the cylinder distort the bed further by creating another clockwise circulation near the top as shown in Fig 3-1(c).

Low-rotation-rate transition (LT)

This phase is a result of continuous evolution from the F2 phase as the rotational velocity is increased. A small increase in the rotational speed is enough to destroy the secondary flows associated with the fingering flow phases. The particle bed at the upper section of the cylinder which is prominent in the first three phases is completely destroyed. The circulation shown for F2 phase near the particle bed in Fig. 3-1(c) becomes fully blown, spreading the particles as depicted in Fig. 3-1(d). Instantaneous particle positions at different times are shown in Fig. 3-2 to illustrate the evolution of steady state nonequilibrium patterns in the drag-dominated phases from initially homogeneous distribution of particles. It is apparent that in the radial direction, the system does not take much time to attain steady state for a corresponding rotational velocity. Evolution to the GB phase illustrates the gradual movement of particles towards the top due to the dominance of drag. In the evolution to F1 phase, it can be observed that the rotation of the cylinder provides the necessary impetus for the particles to be slightly dispersed away from the cylinder. The GB, F1, and F2 phases do not require too many rotations of the cylinder to reach steady state since the rotational velocity is very low. It is also obvious from the figure that the LT phase evolves to steady state configuration much faster owing to the increased rotational velocity.

Homogeneous region (HR)

From Fig 3-3(a) we can see that there are absolutely no secondary flows associated to the rotational flow of the suspension. This leads to almost uniform distribution of particles along the radial plane. The bed formed due to particle aggregation near the top due to buoyancy in the previously observed phases is destroyed completely. Velocity vectors and particle distribution indicate that the flow is equivalent to rigid body rotation as a majority of particle trajectories have a fixed axis of rotation. The occurrence of the HR phase coincides with the balance between the buoyancy and centrifugal forces since the phases before this show the dominating nature of buoyant

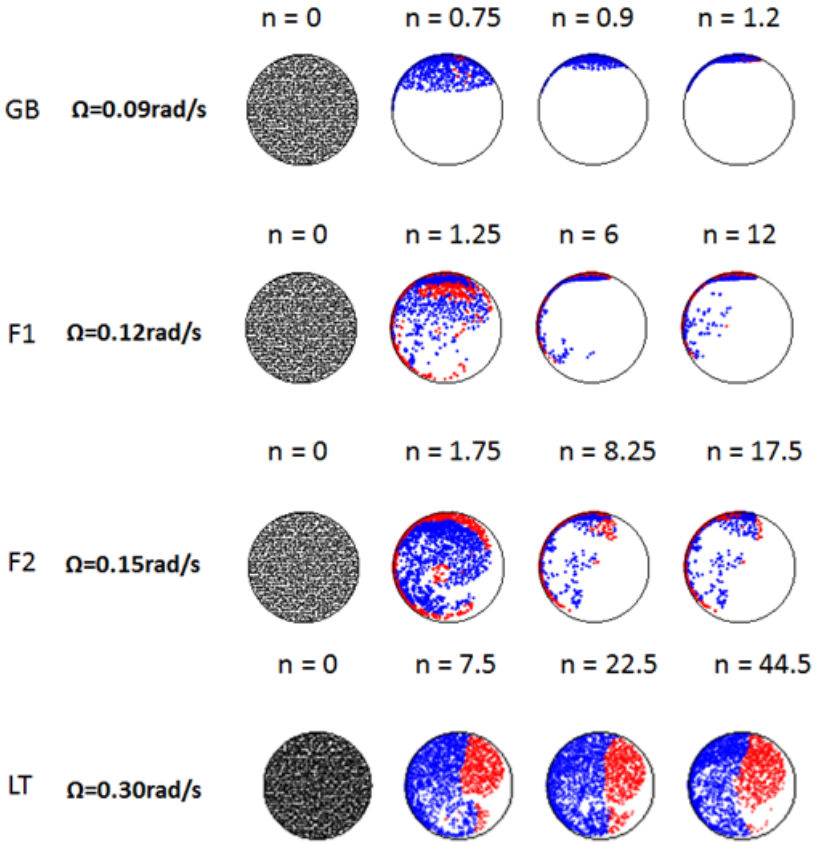

Figure 3-2: Phase evolution for drag-dominated regime. Here n_r represents the number of rotations of the cylinder, red particles move down and blue particles move up. Black particles indicate initial configuration ($n_r = 0$).

force while the phases which occur after HR indicate that centrifugal forces have stronger influence.

Discontinuous banding (DB)

Figure 3(b) shows the radial pattern observed at 15 rad/s. Since the particles are less dense than the suspending fluid, centrifugal force draws the particles radially towards the center of the cylinder. As these particles are drawn towards the center of the cylinder, they tend to form a core around the rotational axis with the remaining particles forming a cloud around the central core.

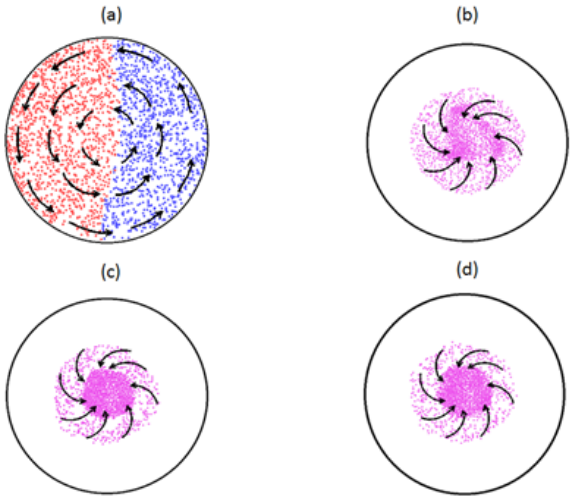

Figure 3-3: Velocity vectors and particle distribution at steady state for the centrifugal-force-dominating regime. (a) $\Omega = 0.75\ rad/s$, particles are dispersed throughout the cylinder (HR); (b) $\Omega = 15 rad/s$, increased centrifugal force propels particles towards the rotating axis (DB); (c) $\Omega = 30\ rad/s$, (CL) particles congregate around the center of the cylinder; (d) $\Omega = 35\ rad/s$, (CL) further increased velocity produces no change in the qualitative behavior of the particles. Red particles move downwards, whereas the blue particles move against gravity. Magenta indicates radially inward motion.

Centrifugal Limit (CL)

In the case of settling suspension the particles swirl out to the wall of the cylinder, whereas the particles in this system form a cluster around the rotating axis of the cylinder. Our simulations reproduced the fact that the fraction of particles which constitute the central core is ~ 0.6 of the total number. Direction of motion of the particles indicated by arrows show similar behavior to the DB phase as the qualitative behavior of particles remains the same in both the phases.

Fig. 3-4 gives the evolution of steady state nonequilibrium patterns in the centrifugal force dominated phases. It is clearly observed that the qualitative behavior of the particles in DB and CL phases is mostly similar. Change in the direction of the particle motion (as to where they settle at steady state) owing to the increase in the rotation rates is evident. Moreover, we can also understand that the increase in the rotation rates in turn tends to increase the centrifugal forces as particles show more affinity to form clusters at the center of the cylinder. The increase in the number of

rotations of the cylinder to attain steady state is because it takes a while to form a dense core of particles.

Fig. 3-5 shows the radial-concentration profile at different frequencies along the positive y axis. In the GB phase the buoyancy force is much larger compared to the viscous drag and centrifugal forces. This causes all the particles to rise and accumulate near the top. For the HR phase the profile is almost flat, suggesting nearly homogeneous distribution of particles throughout the cylinder. In this regime the magnitude of different forces is comparable. The DB and CL phase profiles indicate the build-up of particle beds along the rotating axis of the cylinder.

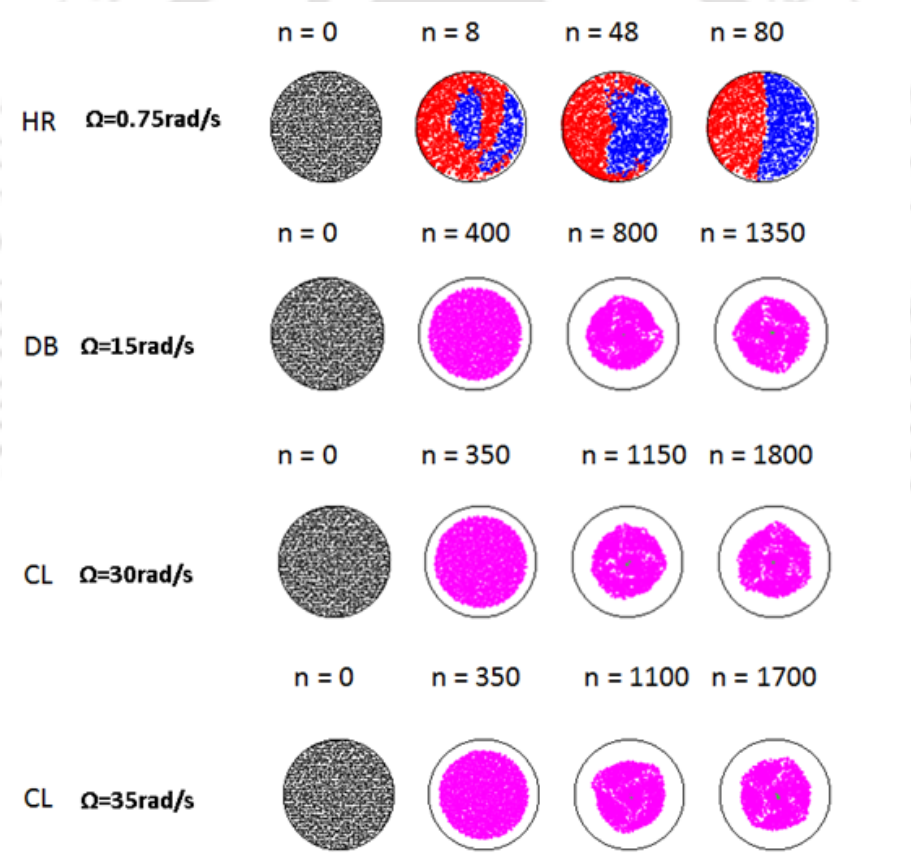

Figure 3-4: Phase evolution for centrifugal force dominated regime. Black is used for the initial configuration. Here n_r represents the number of rotations of the cylinder; red particles move down, and blue particles move up. Magenta indicates inward motion towards the center of the cylinder.

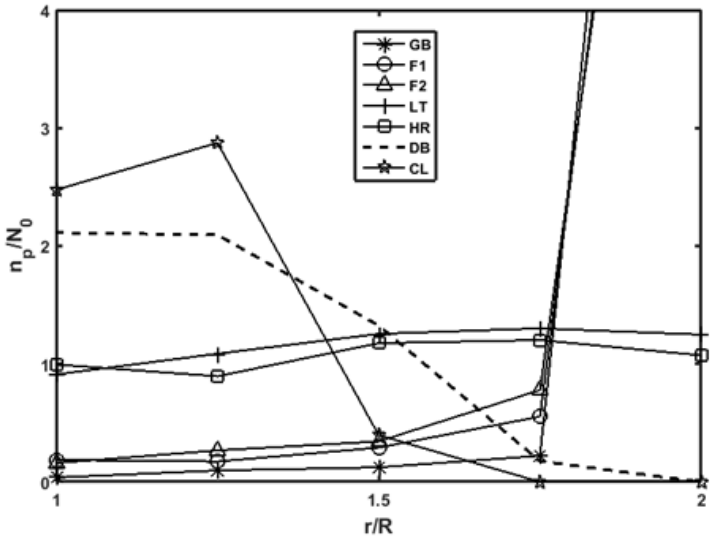

Figure 3-5: Equilibrium concentration profiles in the radial direction for different frequencies of rotation. Here n_p and N_0 are the number of particles after reaching steady state and at t = 0, respectively.

3.3.2 Order parameter

The particle distribution and the direction of particle motion from Fig. 3-1 suggest that the order parameter can be defined as $\left\langle \dot{\theta} \right\rangle = \left\langle \sum_{i=1}^{N} \dot{\theta}_i \right\rangle / N$ based on the time-averaged angular velocity. It could distinguish between the drag-dominating segregated phases where the particle returns to the bed soon after getting detached from it and homogeneously distributed. The order parameter given by the expression $Q = \left\langle \dot{\theta} \right\rangle / \Omega$ was defined in Ref. [26] for the sedimenting particle system. Since the experimental conditions for both the settling and the floating particle systems are identical, the postulation in Ref. [26] could be used for the present work. The significant quantities which characterize Q are the velocity of the fluid and the rising velocity of the particle ($u_f = m_B g/\xi$) as defined in the single-particle dynamics, with l being the characteristic length. Therefore, flow under the experimental conditions can be categorized by the dimensional ratios $u_f/\Omega l$ and $u_c/\Omega l$. As discussed earlier all phases prior to the occurrence of the homogeneous region fall under the buoyancy or gravity-dominated regime, and the phases which follow after HR fall under the influence of centrifugal force due to the rotational velocity of the cylinder. Hence the

dimensionless ratio $u_f/\Omega l$ is used in the determination of the order parameter for the buoyancy-dominated regime. Fig. 3-6 shows the variation of the order parameter Q with the rotational frequency of the drum. Fig. 3-6(a) shows that the size of the cylinder has no influence on the transition frequency. However, it can be seen that the mean particle concentration affects the transition frequency, as it affects the mean rising velocity of particles in the buoyancy-dominated regime. The numerical value of Q lies between 0 and 1, each representing completely segregated and fully dispersed phases. In Ref. [26] it is suggested that for a settling system, the mean interparticle separation $d = 1/n_0^3$ is the characteristic length, where $n0$ is the average particle concentration. Fig. 3-6(b) affirms the claim that even for the floating system the mean interparticle separation is the characteristic length. Choice of mean interparticle distance for the characteristic length is supported mathematically by a mass balance over the low rotational frequency phases. The up-flux of the particles due to buoyancy scales as $M \sim u_f nRL$ (here n is the number of particles in the monolayer), whereas the down-flux of a monolayer of particles getting dragged down by the rotation of the cylinder scales as $M \sim \Omega anRL$ (the monolayer of particles have a thickness proportional to their radius a). A balance over these fluxes shows that the resulting dimensionless number is $\Omega a/u_f$ [26].

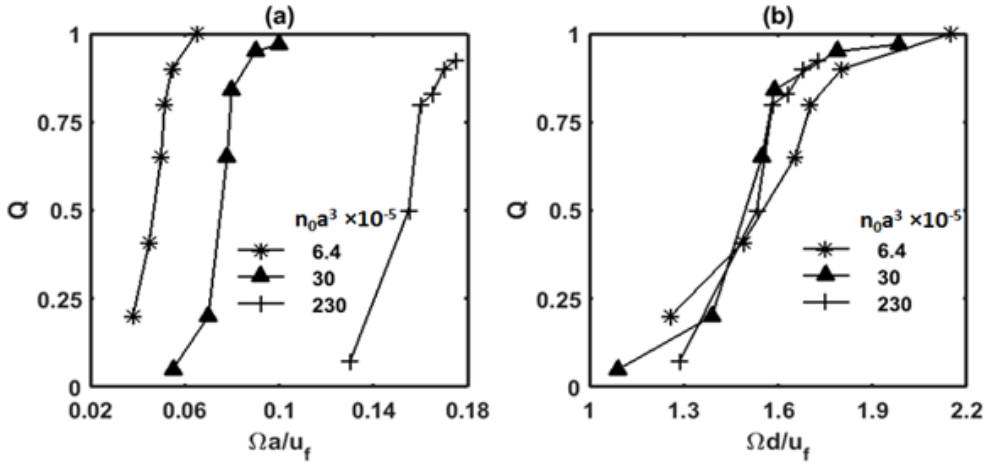

Figure 3-6: Order parameter (Q) for various particle concentrations is plotted versus the two dimensionless numbers (a) $\Omega a/u_f$ and (b) $\Omega d/u_f$, where n_0 is the average particle concentration, a is the particle radius, and d is the mean interparticle separation ($d = 1/n_0^3$).

3.3.3 Axial Segregation

To observe axial segregation, simulations were performed with $L = 5R$ and with a total of 12465 particles. All the studies in this section are performed with a random initial configuration of particles as shown in Fig. 3-7(a). Several distinct phases such as HR, LD, SB, and CL observed experimentally were reproduced through the simulations. HR shows complete mixing, whereas LD and SB exhibit axial particle bands. Fluctuations of particle density in the radial plane induce additional movements of particles in the axial direction. These additional movements in the axial direction serve as a perturbation to the axial particle density. As steady state is reached, the perturbations grow into large axial density variations, thereby leading to the formation of axial banding patterns. The observations are detailed in the description of LD and SB phases.

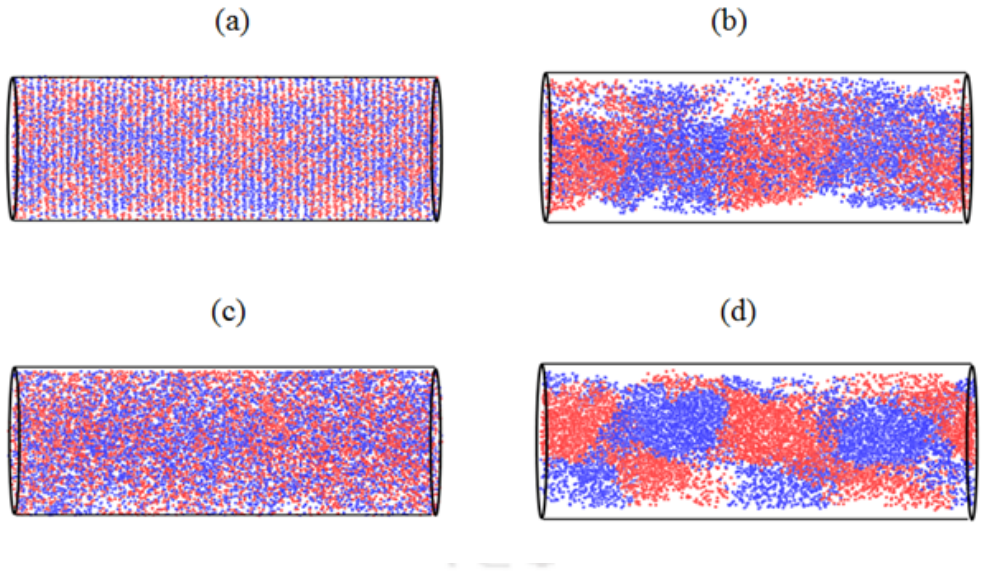

Figure 3-7: Axial patterns observed in the centrifugal-force-dominated regime. Red particles move towards the right, and the blue particles move to the left. (a) Random initial configuration of particles suspended in the cylinder; (b) HR phase, = 1.25 rad/s, uniform distribution of particles throughout the cylinder; (c) LD, = 2.5 rad/s (top view, gravity is pointing into the plane of the paper), and particles converge into high-concentration regions while rising and spread out as they reach the top; (d) LD, = 2.5 rad/s (front view, gravity is pointing downward).

Homogeneous region (HR)

From Fig. 3-7(b) it is evident that the particle distribution in the cylinder shows uniformity. The particle clusters which remain near the wall which appear for GB, F1, and F2 phases are completely destroyed as the particles mix uniformly. The influence of drag seen in LD is absent in this phase as the particle motion becomes identical to rigid body rotation. The particles can be seen to be moving both in the positive and negative z direction, signifying particle mixing leading to a homogeneous distribution.

Local-structure dropout (LD)

Unlike the previous phases the LD does not show any form of resemblance to the settling system. The settling system which is characterized by the redistribution of particles spreads from one location along the axial direction, but for the buoyant system there is spatiotemporal chaos. The phase is characterized by exchange of particles between the bands and oscillation in bands with time observed as a consequence. This oscillation of bands and their nonuniform structure is well illustrated in

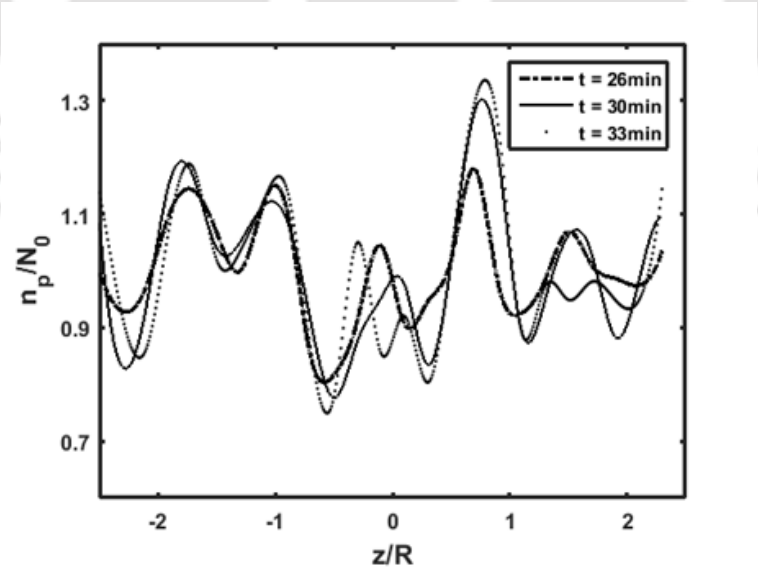

Figure 3-8: Concentration profiles at three different instants indicating exchange of particles (traveling bands) along the axial direction for particle density, $\rho_p = 0.15$ g/cc and $\Omega = 2.5$ rad/s. Here n_p and N_0 are the number of particles after reaching steady state and at t = 0, respectively.

Fig. 3-8; particle concentration for different number of rotations indicates the drifting mechanism experienced by the particles. In this phase, the centrifugal forces are not as weak as in the case of phases prior to the HR phase. As the particles are less dense than the fluid, these particles are pulled in towards the center of the cylinder. The interplay between a relatively strong centrifugal force and the buoyant force causes these particles to apparently spiral inwards and outwards, causing exchange of particles and oscillation of bands. This form of oscillation in bands is similar with the phenomenon reported in Ref. [3]. The axial patterns shown in the associated Fig. 3-7(c) and Fig. 3-7(d) are obtained after 750 rotations of the cylinder at 2.5 rad/s.

Centrifugal Limit (CL)

On the occurrence of the CL phase, most of the particles concentrate around the axis of rotation of the cylinder. Along the axial direction Fig. 3-9 shows the central particle core, which has a fraction (~ 0.6) of the total particles, while the rest of the particles form a cloud surrounding the central core. However, the simulations were unable to reproduce bands in the DB phase and during the transition from DB to CL phase, which were reported experimentally. These observations could

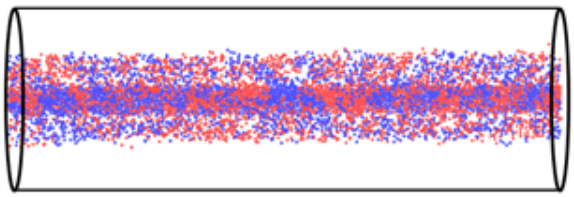

Figure 3-9: Central core formation in the centrifugal limit (CL) for $\Omega = 30\ rad/s$. Particles congregate around the rotational axis of the cylinder reaching the maximum packing limit for a suspension.

lead us to a conclusion that hydrodynamic interactions involved in the dilute system influence particles closer to each other to develop a buckling instability, which leads into clustering of particles. It can now be firmly implicated that the axial differences in

particle concentration are catalyzed by these particle clusters, which become denser as more particles get drawn into the already formed clusters. The curved cross section of the rotating vessel also enhances the growth of this instability, which results in axial banding. This is reinstated by the fact that the fluid down-current due to the rotation of the drum enhances the rate at which particles rise to the top of the cylinder. Nevertheless, occurrence of the HR phase between phases where axial banding was evident implies that the balance among forces acting on the suspension and the cross section of the cylinder are pivotal for the instability to develop. Any imbalance among these forces leads to a buckling instability causing periodic clustering of particles in the cylinder. The imbalances among the centrifugal and buoyancy (gravity and drag) cause a variation in the radial concentration of particles, eventually leading into particle clustering and banding along the axial direction. Both numerical and experimental results reestablish that there would be no axial concentration bands when there is homogeneity in the concentration of particles in the radial plane.

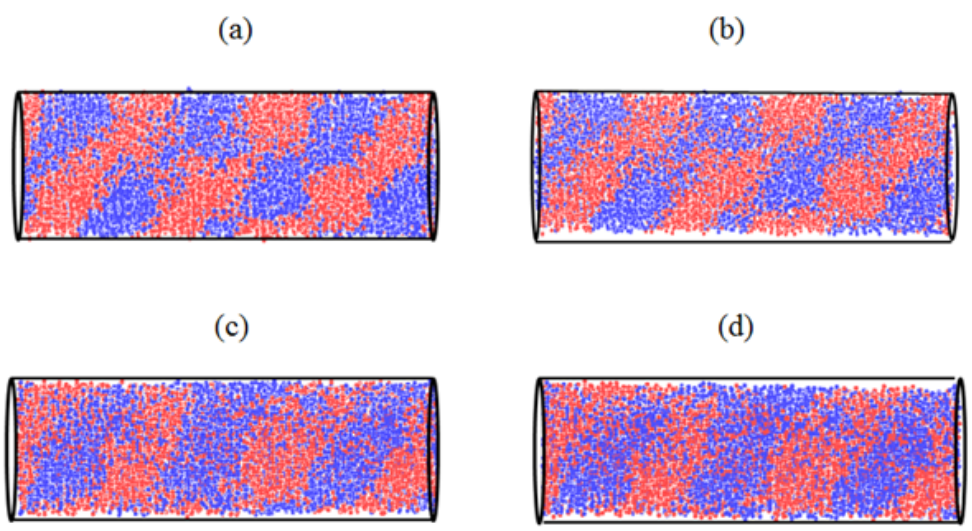

Figure 3-10: Axial segregation (rho_p = 0.19 g/cc) in the stable band phase for Ω = 2.25 rad/s: (a) front view at 800 rotations of the cylinder; (b) top view at 800 rotations; (c) front view at 900 rotations; (d) top view at 900 rotations. Red particles move towards the right, and the blue particles move towards the left. Gravity points downward on the plane of the paper in front view and into the plane of the paper in top view.

Stable bands (SB)

We have carried out one simulation where the density of particle was increased to 0.19 g/cc and the rotational frequency was 2.25 rad/s as indicated in Fig. 3-10. Fig. 3-11 shows the plot of particle number density along the axial direction. Unlike the travelling bands in the LD phase (Fig. 3-8), the stripes of particles in SB phase remain stationary as steady state is reached. This indicates that in the SB phase there may not be any exchange of particles between consecutive bands. This reinforces the statement made earlier that the traveling of bands is observed only for certain imbalance between buoyancy and centrifugal forces. It is also evident that the number of bands is increased to three from the LD phase ($\rho_p = 0.15\ g/cc$, $\Omega = 2.5\ rad/s$), which contains only two bands. We are unable to provide any explanation for the difference in the number of bands between the LD and SB phase.

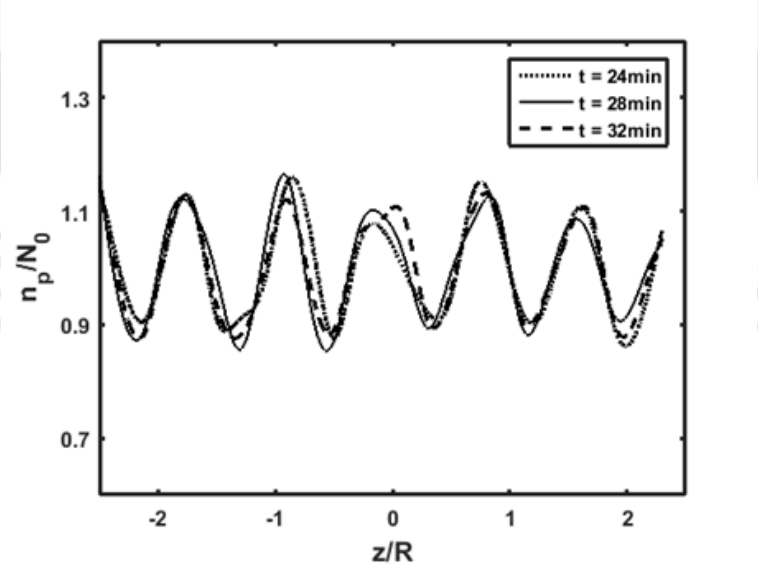

Figure 3-11: Equilibrium concentration profiles of particles for $rho_p = 0.19\ g/cc$ at $\Omega = 2.25\ rad/s$. There is almost no exchange of particles along the rotating axis over time indicating stable band patterns. Here n_p and N_0 are the number of particles after reaching steady state and at t = 0, respectively.

3.4 Comparison With Experiment

As reported earlier, nine independent nonequilibrium states were observed in the experiments of Kalyankar et al. [18] for positively buoyant suspensions. Our simulation studies could reproduce the characteristic behavior of almost all the phases. For the three regimes classified earlier, the radial patterns were reproduced quite convincingly. he comparison between experimental works of Kalyankar and the current simulation work in this thesis are compared. The figure is also added in the thesis for better understanding and comparison. Seven radial phases which are distinct are compared in Fig. 3-12 given below. It can be observed that there is good agreement between the experimental and simulation results.

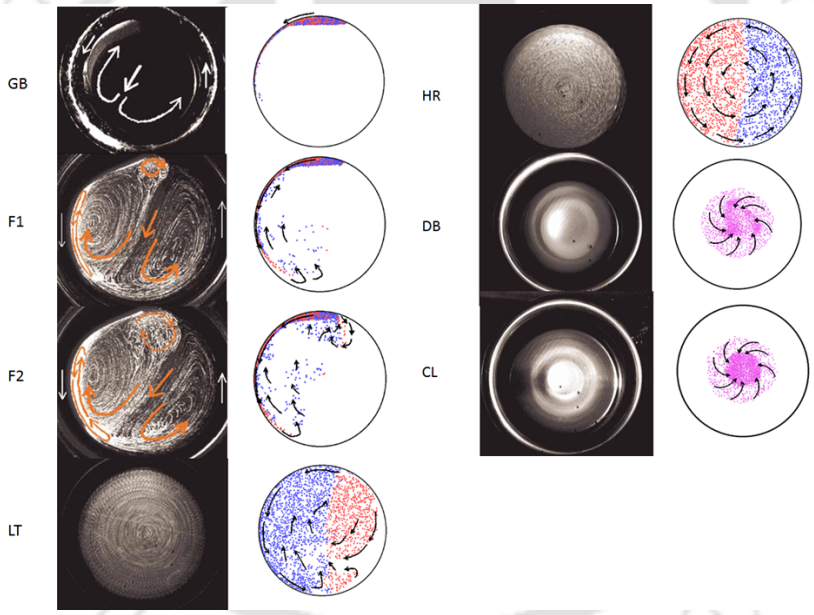

Figure 3-12: Comparison between experimental and simulation results for phases in the radial plane.

Along the axial direction, we tried to study the dynamics of SB, HR, LD, DB and CL phases. We had obtained axial profiles with good agreement with the experiments of Kalyankar et al. (2008) except for the DB phase as indicated by Fig. 3.13 below.

The axial banding patterns observed in the SB and LD phase have both qualitative and quantitative agreement with the experimental results. However, for the axial bands for the high-frequency DB phase and in the low-frequency regime for

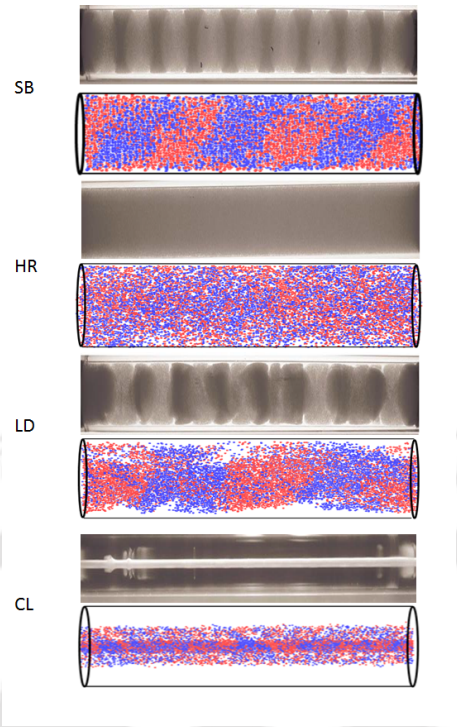

Figure 3-13: Comparison between experimental and simulation results for phases in the axial plane.

the GB/F1 phases, the simulations do not capture completely the experimentally reported behavior. These discrepancies with the experimental observations evidently occur when the concentration of the particle is relatively high. In the simulations the particles are approximated as Stokeslets, and the contribution from higher order multipoles arising from the finite size of the particle is neglected. Reasonable agreement of radial patterns was observed for GB and CL phases where the particle concentration in certain regions goes up. In the granular bed regime, though the particle concentration is very high, there is not much movement of the particles, and the hydrodynamic drag is weaker compared to the buoyancy force. On the other hand, in case of the centrifugal limit, though the particle velocities are higher the radially symmetric distribution may ensure that the results from point particle simulations would be qualitatively similar to the case of finite-sized particles at higher volume fractions.

Recent studies [36, 37, 32] incorporated higher order multipolar solutions to analyse the case of many-body dynamics inside a cylinder by applying proper no-slip

boundary conditions on the particle surface. Unlike the case of point particles, inclusion of higher order multipoles takes into account the effects of the finite size of the particle. Addition of the effects of the particle size would probably capture the dynamics in the low- and high-frequency regimes where the phases exhibit high concentration as these interactions are primarily due to mutual hydrodynamic influence or direct contact in collision. These short-range lubrication forces are expected to cause enhanced diffusivity as indicated by Zurita-Gotor *etal*. [32].The enhanced diffusivity is a prime factor for the observed difference in the value of the dimensionless frequency ($\Omega* = \Omega d/u_f$), which ranges between 1.1 and 1.5 for experiments and 1.35 and 1.75 for simulations. The deviations of the simulation results from experimental observations and the axial patterns in the DB phase arise due to the exclusion of Stresslets and lubrication forces. Another reason for the deviation from experimental results could be due to the periodic boundary conditions in the simulations, which is different from the experimental boundary conditions of no-slip rotating end-walls. It can be expected that the no slip rotating end wall might strengthen the rigidly rotating fluid field near the wall. However, the simulation methodology is currently not equipped with providing an end wall with no slip condition. The convective contribution to band formation might also be a factor for the band formation in DB phase, but it has no effect on the low-frequency phases. Inclusion of convective effects may capture the dynamics of particles in the DB phase, and the study might as well be extended to understand the patterns reported in Refs. [28, 2].

3.5 Conclusion

Most of the distinct patterns which appeared in both radial and axial directions obtained by Kalyankar et al. were reproduced by this simulation technique, which includes only the far-field hydrodynamic interactions. The oscillation of bands with time in the LD phase was also observed. The order parameter Q and the characteristic length l are comparable with the settling system in Ref. [27] in the buoyancy-dominated regime. Axial banding observed in Ref. [18] in the DB phase could not

be reproduced in the simulations.

According to Lee and Ladd [25], buoyant system would not be able to produce axial patterns as there would be repulsive interactions among floating particles, unlike settling particles, which always have attractive interactions. However, this theory seriously underestimated the strength of a canceling field with a flat wall approximation. Although the source field interaction should be indeed attractive or repulsive for heavier or lighter particles than the medium, the canceling field exactly nullifies the source field interaction between ring Stokeslets along the axial direction. Both experiments and simulations could recover banding patterns in the axial direction for a buoyant particle system. This can be ascribed to the inhomogeneous distribution of particles in the radial plane due to imbalance in the forces acting on the particle as explained for settling particles in Ref. [27].

Though there is a difference in the direction of centrifugal force for the settling and floating particle suspensions, it is clear that the axial banding phenomenon is observed in either system. Simulation results show that to achieve complete mixing of particles there must be perfect balance of all the forces acting on them. Therefore it is apparent that the axial bands are formed only when there is a certain imbalance in the forces acting on the particles. This imbalance in both the systems changes due to the change in the direction of the centrifugal force, causing the appearance of HR phase before the SB phase in the buoyant system. If we recall from the single-particle dynamics, the HR phase is apparently a balance between the forces in the system. As the domination of forces shifts from buoyant to centrifugal there is formation of HR phase and hence the shift in position from the settling system.

Chapter 4

Dynamics of bi-density particle suspension in horizontal rotating cylinder

4.1 Motivation

As mentioned earlier, there only a few works which concentrated extensively on understanding the behaviour of particles differing in size or density. The phase evolution of such kind of particle systems in a horizontal rotating cylinder is yet to be determined. This chapter is devoted to comprehend the characteristics of bi-density suspensions when rotated at different angular velocities of the cylinder. The suspended particles could be either settling or floating or a mixture of both. However, in the present work only the settling and floating suspensions are investigated. It is established through the experimental findings of Kumar and Singh [24] that for bi-disperse particles, the particles do segregate axially into bands of particles and clear fluid. The current work also focusses on investigating the capability of these systems to form axial bands.

4.2 Numerical Method and Simulation set-up

A representation of the bi-density particles suspended in a horizontal cylinder is shown in the schematic diagram below in Fig. 4-1.

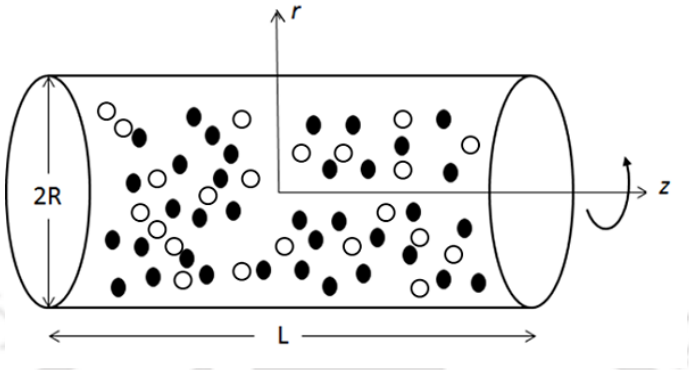

Figure 4-1: Schematic sketch of the rotating cylinder system.

We performed numerical investigations on two systems; settling and floating. As the name indicates, in the settling system particles are denser than the suspending fluid and vice-versa in the floating system. In either of the systems, densities of the heavy and light particles are denoted by ρ_{p_2} and ρ_{p_1} respectively. The number of heavy, light particles in the system was 1150 each for radial simulations and 6232, 6233 respectively for axial studies. Three density ratios of the particles $\rho_{p_2}/\rho_{p_1} = 2, 3, 5$ were studied in the radial direction to estimate the effect of density ratio on the observed phases; however only one density ratio 2 was used for the axial studies. The fluid viscosity μ was $55cp$ (except in centrifugal force dominant regime where it was $80cp$), and its density ρ_f was $1.16g/cc$. The particle density $\rho_{p_1} = 2.18g/cc$ was for the sedimenting system while for the floating system it was $\rho_{p_1} = 0.30g/cc$ (It should be noted that ρ_{p_2} changes according to the density ratio). The cylinder length L for radial and axial simulations was $0.2R$ and $5R$ respectively. Simulations were performed over a wide range of rotational velocities Ω. The flow Reynolds number $Re_f = \rho_f \Omega R^2/\mu$ varied between 0.18 to 41. The initial configurations for the simulations in radial and axial planes are provided in Fig. 4-2(a) and Fig. 4-2(b) respectively. The particle Reynolds number is calculated using the formula $Re_p = \rho_p 2r u_{s/f}/\mu$ where $u_{s/f}$ denotes sedimenting/floating velocities respectively. This velocity is calculated

using the formula $u_{s/f} = \pm[2a^2(\rho_p - \rho_f)g/9\mu]$. For the reference particle, this velocity is $u_{s/f} = 0.0458/0.0373 cm/s$. The corresponding Reynolds numbers for sedimenting and floating systems (for the reference particle) are $Re_p \approx 0.001, 0.0001$ respectively. With five-fold increase in the density of the particle, the Reynolds number will increase by twenty five times.

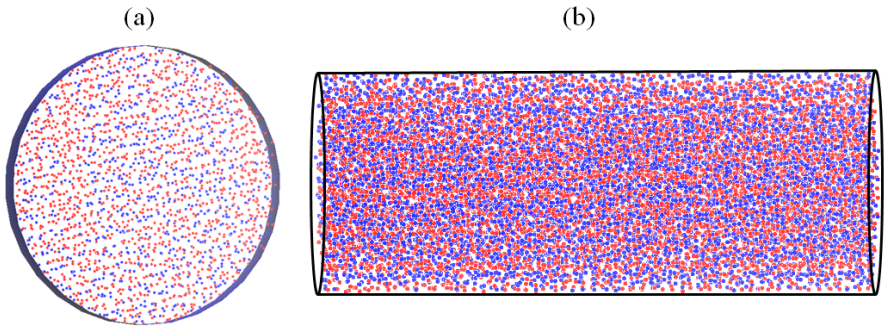

Figure 4-2: Initial configuration in (a) radial direction (b) axial direction; Particles are colour coded as red|light and blue|heavy. The number of particles in the radial and axial simulations were 2300 and 12465 respectively.

4.3 Results and Discussion

As mentioned in the previous section, several simulations were performed to understand the dynamics of settling and floating systems. In either of the systems (for all density ratios), we observed that they exhibit eight independent steady states from the radial studies. It is known that the forces acting on the particles are drag, gravitational and centrifugal. The phases exhibited by both systems are classified into two regimes; gravitational and centrifugal based on whichever force is dominant. Our observations also show evidence of band formation for both systems in the axial direction. The results are described below explicitly for the settling and floating systems.

4.3.1 Settling System

Radial Patterns

Fig. 4-3 and Fig. 4-5 show the phases of the settling system which fall into the gravitational and centrifugal regimes respectively. Column I in these figures refers to the configuration of the heavy and light particles combined; whereas columns II and III are the configurations of heavy and light particles respectively. The behaviour of particles in the phases exhibited is detailed here.

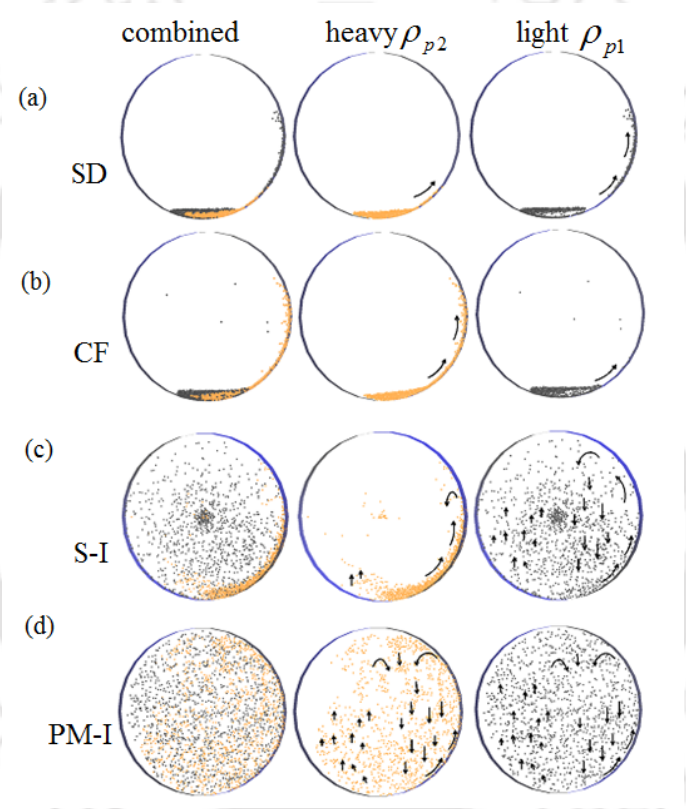

Figure 4-3: Phases in the gravity dominated regime for the settling system with a density ratio 2. (a) Sedimenting phase at $\Omega = 0.1\ rad/s$, (b) formation of the heavy particle core at $\Omega = 0.13\ rad/s$, (c) heavy particles segregated from the light particles at $\Omega = 0.6\ rad/s$, (d) ascending values of Ω (at $0.9\ rad/s$) cause the segregated particles in the previous phases to mix partially.

Sedementing (SD) : When the cylinder is at a very low rotational velocity, particles fall through the fluid under the action of gravity. Since gravity has the predominant influence, heavy particles settle prior to the light particles. This leads to

the formation of two layers of particles at the bottom of the cylinder with heavy particles occupying the lower layer. A few particles from the upper light particle layer are dragged with the rotation of the wall. Since the particles essentially settle it is termed as Sedimenting phase (SD).

Core Formation (CF) : On slight increase in the rotational frequency of the cylinder, a core of heavy particles is formed which is surrounded by light particles. The core formation could be comprehended from the cavity created due to the core of heavy particles in the image of the light particles in Fig. 4-3(b). This phase shows similar characteristics to that of dry granular media [19]. Akshat et al.[14] also reported identical core formation for bi-density sedementing suspensions. Though the heavy particles form a core a few of them are dragged along the wall while the light particles remain intact in the bed. Increase in the density ratio of the particles enhances core formation.

Segregation-I (S-I) : In this phase, rotation of the cylinder causes both heavy and light particles to rise along the wall. After losing contact with the wall, the heavier particles fall back through the fluid into the heavy particle bed under the influence of gravity. However, the light particles are scattered through the carrier fluid since they experience less gravitational force. As the particles in the right section of the cylinder fall down they set up a counter current in the left section. This counter current induces an upward movement of the light particles as shown in the Fig. 4-3(c). It is also clear that the heavy particles are segregated from the light particles.

Partial Mixing-I (PM-I) : This is the final phase in which the gravitational force is dominant. As the name indicates, the heavy and light particles are in a partially mixed state. Both heavy and light particles which get lifted along the wall fall under gravity in the right section. This sets a counter current in the left section forcing the particles to move upwards in a manner similar to the motion of light particles in S-I. The heavy particle bed that is present in S-I is completely destroyed.

Fig. 4-4 shows the number density plots for phases which fall into the gravitational

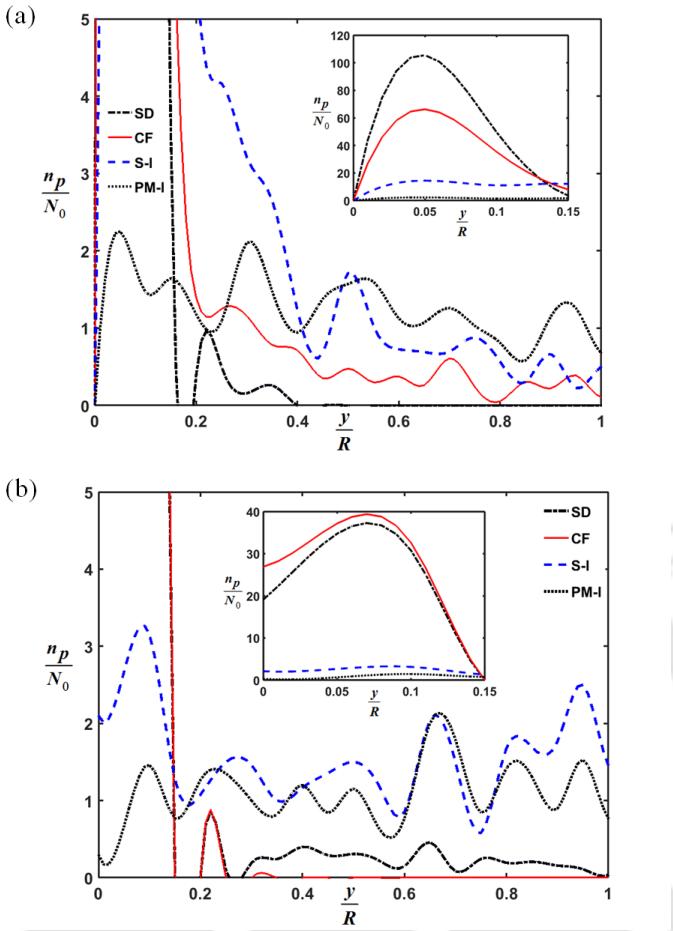

Figure 4-4: Number density plots in the gravity dominated regime for (a) heavy and (b) light particles, here n_p and N_0 are the number of particles at steady state and $t = 0$ respectively.

force dominated regime. The x-axis of the plot is the vertical direction (y) in Cartesian plane with 0 representing the bottom and 1 representing the centre of the rotating cylinder. Concentration of heavy particles is higher at the bottom of the cylinder in SD and CF phases compared to the light particles as indicated in the Fig. 4-4. Segregation of heavy particles in the S-I phase is clearly depicted in the figure. Both heavy and light particles distribution do not show sharp variations in concentration hinting at the onset of mixing.

Mixing (M) : As the rotational velocity increases further, the influence of gravity on the particles is no more dominant. Fig. 4-5(a) shows that the particles are

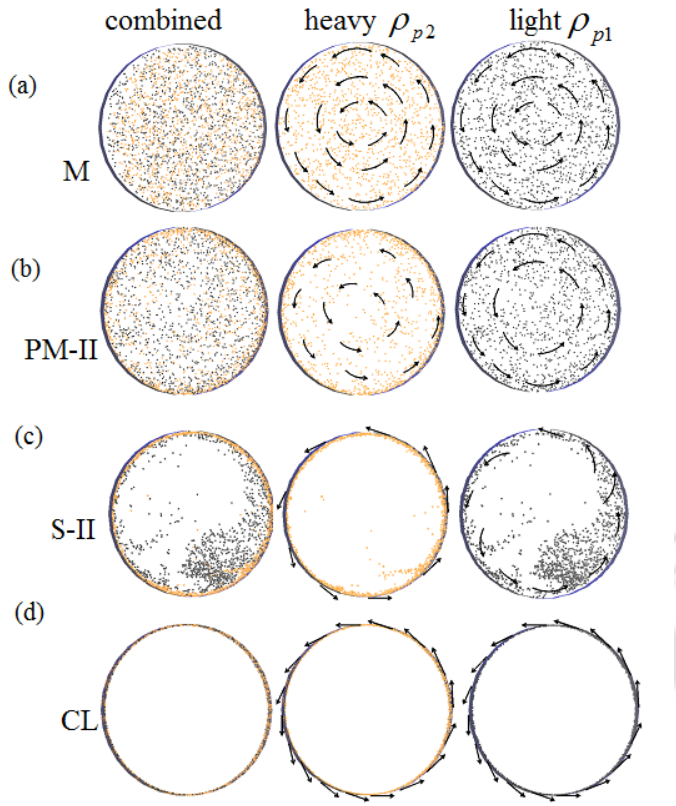

Figure 4-5: Centrifugal force dominated regime for settling system with density ratio 2: (a) complete mixing of heavy and light particles due to balance in the forces ($\Omega = 1.2\ rad/s$) (b) PM-II phase at $\Omega = 2.5\ rad/s$ heavy particles guided towards the wall (c) S-II occurs at $\Omega = 7.5\ rad/s$ segregating the heavy particles from the light ones due to increased centrifugal force (d) complete centrifugation of either of the particles at $\Omega = 12\ rad/s$.

distributed uniformly in the cylinder. Forces acting on the particles are balanced in such a way that both heavy and light particles remain completely dispersed through the fluid. This is the only phase where the heavy and light particles move in tandem.

Partial Mixing- II (PM-II) : This phase occurs when the centrifugal force begins to show its impact on the heavy particles. As a result the heavy particles tend to swirl out towards the cylinder wall leading to partial mixing with lighter ones as in Fig. 4-5(b). It is interesting to know that the light particles remain fully dispersed in PM-I, M and PM-II but it is the change in the dynamics of heavy particles which cause the occurrence of these phases.

Segregation-II (S-II) : On further increase in the rotational velocity, heavy particles get settled on the inner wall of the cylinder. Whereas, light particles which experience lesser centrifugal force still rotate with the suspending fluid as in Fig. 4-5(c). Difference in the magnitude of centrifugal force on the particles leads to segregation which is a characteristic similar to dry granular systems [5]. The level of segregation increases as the density ratio of the particles is increased.

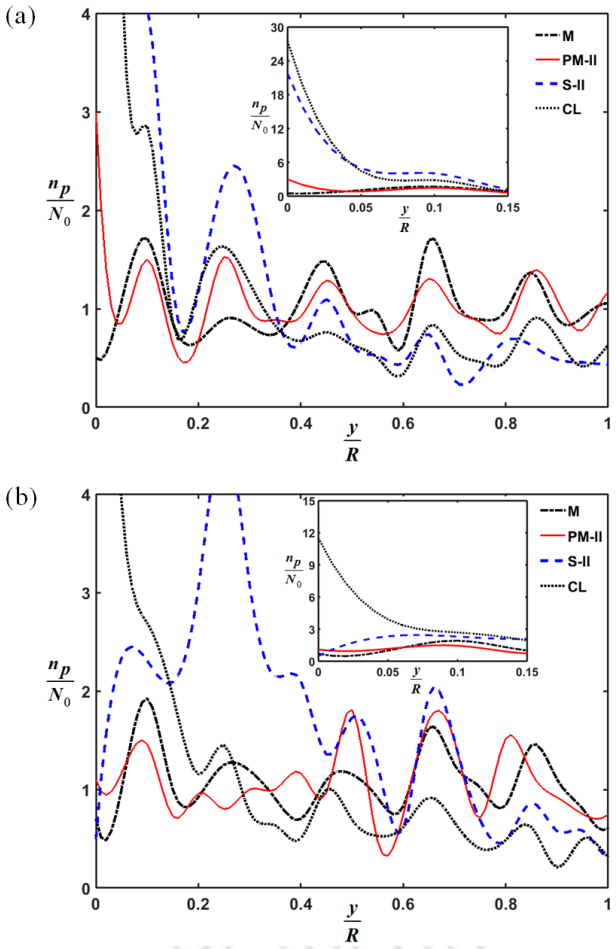

Figure 4-6: Number density plots in the centrifugal force dominated regime for (a) heavy particles (b) light particles, here n_p and N_0 are the number of particles at steady state and $t = 0$ respectively.

Centrifuging Limit (CL) : This is the last of all the distinct phases displayed by the settling system. Both particles experience high centrifugal force effecting them to adhere to the rotating wall. There is no layering or any segregation between the

particles unlike the previous phases.

From Fig. 4-6 (inset) it is clear that the concentration of particles at the wall due to the centrifugal force is lesser than that due to gravity in sedimenting phase. This is because particles are distributed all along the wall in the CL phase. S-II phase from Fig. 4-6 shows that heavy particles are at the wall whereas the light ones still rotate with the fluid. However, in M and PM-II phases since particles are more dispersed in the fluid the number density curves do not show sharp variations.

Axial Patterns

Several phases like PM-I and PM-II in the discussion above exhibited partial mixing(or segregation) phenomenon. It is hypothesized through simulations in [26, 27] that for a mono-dispersed suspension, an inhomogeneous distribution of particles in the radial plane leads to axial perturbations eventually developing into axial particle bands. Such inhomogeneities in the radial plane are also present in the bi-density settling suspension as shown in Figs. 4-3(c) and 4-5(b). Therefore, a few simulation

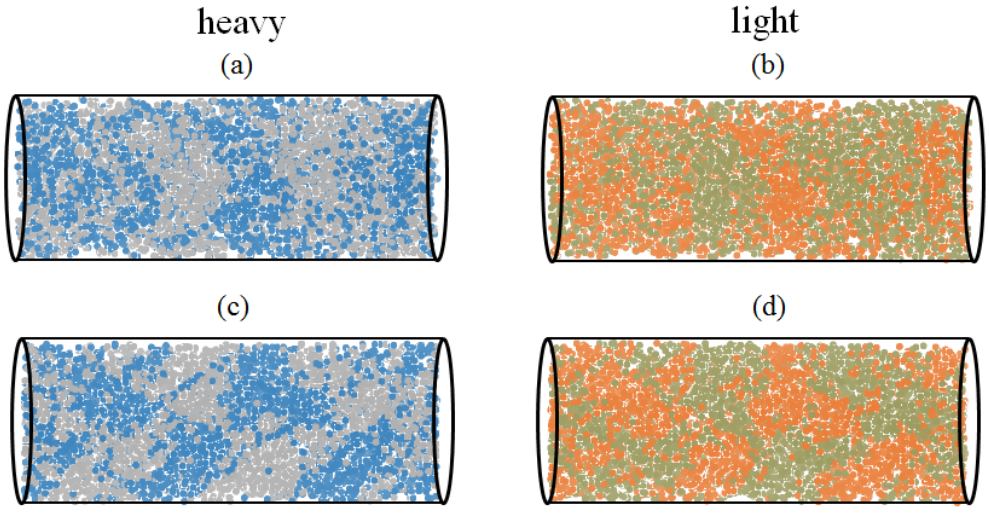

Figure 4-7: Axial banding particle configurations of heavy (column I) and light (column-II) particles after 1050 rotations of the cylinder. Direction of gravity is into the plane of the paper in (a) and (b) implying a top view and is downward in (c) and (d) which represent front view. Blue and orange particles have rightward motion while silver and grey particles move leftwards. $\Omega = 3.5\ rad/s$ and density ratio is 2.

studies were performed in the axial plane with $L = 5R$. In a total of 12465 particles considered for axial studies, the number of heavy and light particles were 6232 and 6233 respectively. The density ratio of heavy to light particles was 2 in all the simulations carried out. The rotational frequencies of the cylinder were chosen from the PM-I and PM-II phases in accordance to the hypothesis of Lee and Ladd [27].

In the Fig. 4-7(a) and Fig. 4-7(b), top view of heavy and light particles with axial bands after 1050 rotations of the cylinder is shown. As indicated by the colour code in Fig. 4-7, blue and orange particles move towards right whereas silver and grey particles move towards left. This opposing motion creates alternate regions of high and low particle concentrations interspersed in the fluid. The high and low concentration regions thus formed evolve into axial banding patterns. From the front view in Figs. 4-7(c) and 4-7(d), it can be understood that particles concentrate while settling from the top and disperse at the bottom wall. This concentration and dispersion of particles generates secondary flows which grow into axial bands.

Evidence of axial banding patterns is also supported by the axial number density profiles in Fig. 4-8(a) and 4-8(b) for heavy and light particles after 1050 and 1100 rotations of the cylinder. Fig. 4-8 demonstrates that the axial bands are prominent for heavy particles than for light particles. However, location of the high particle concentration regions is almost the same for both types of particles.

4.3.2 Floating System

Radial Patterns

Figs. 4-9 and 4-11 show the phases in the gravitational and centrifugal force dominant regimes respectively for the particle density ratio 2. The characteristics of these phases are elaborated below.

Floating (FT) : This phase occurs at very low rotational frequencies of the cylinder. The slight rotation of the cylinder does not have much impact on the movement of the particles as they are influenced by dominant gravitational force. This is clear

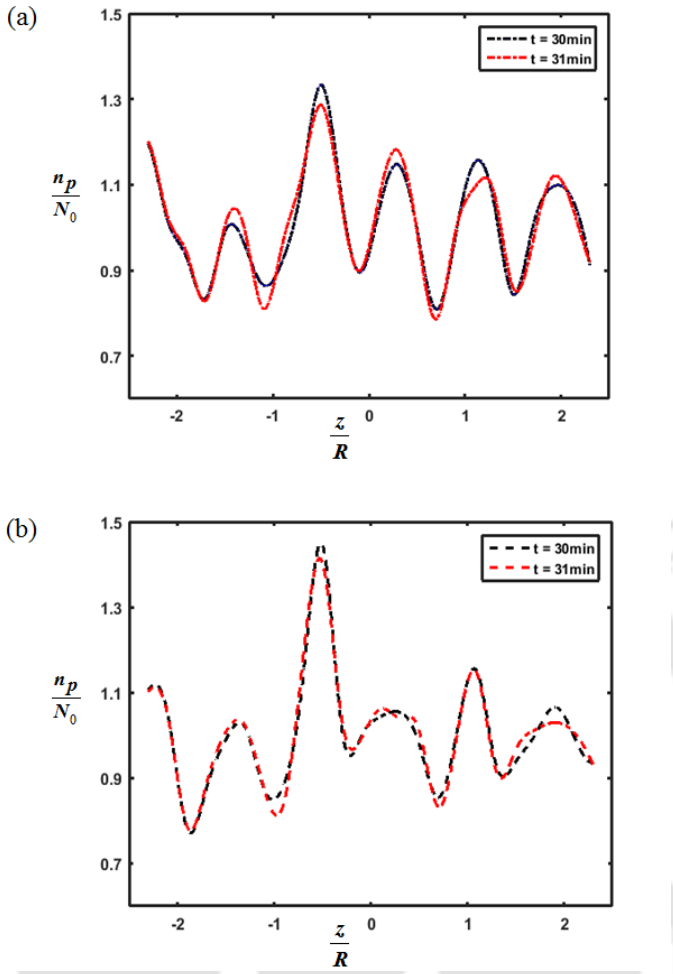

Figure 4-8: Number density plots for axial bands in the settling system (a) heavy particles (b) light particles, here n_p and N_0 are the number of particles at steady state and $t = 0$ respectively.

from Fig. 4-9(a) as the light particles float to the top of the cylinder sooner than the heavy particles. As a result two layers are formed with the light particles on top of the heavy ones. It can also be seen that the rotation of the cylinder drags a thin layer of heavy particles along the wall. This phase is similar to the Sedimenting phase in the settling system.

Core Formation (CF) : The floating system also displays the core formation phenomenon after the FT phase. A light particle core is formed which is engulfed by the heavy particles. Nevertheless a sheet of light particles are dragged down with the

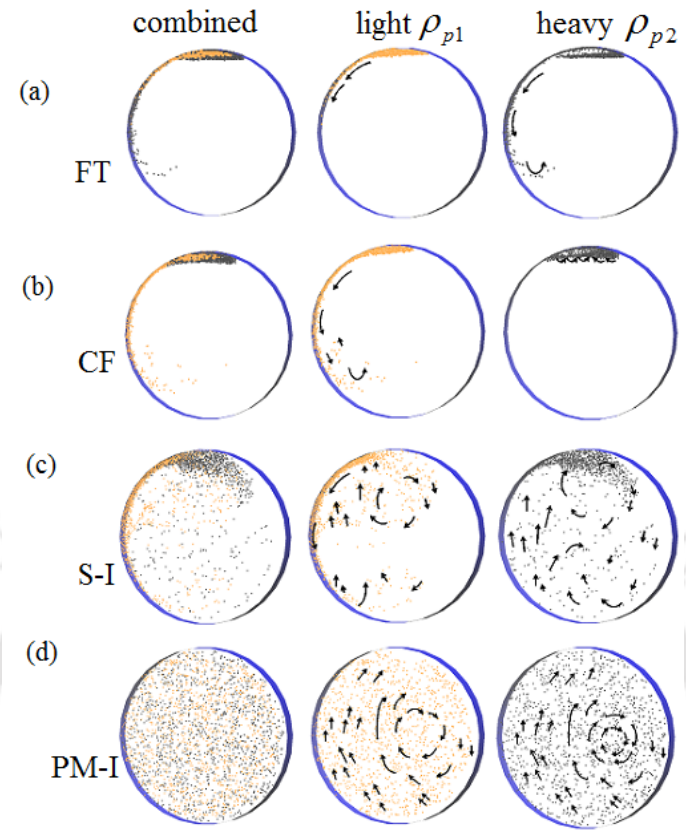

Figure 4-9: Phases exhibited by the floating system with density ratio 2 when gravity dominates (a) Floating at $\Omega = 0.1\ rad/s$, (b) CF which occurs at $\Omega = 0.125\ rad/s$ is also mirror image to CF of the settling system, (c)S-I at $\Omega = 0.5\ rad/s$ with undisturbed heavy particle pool, (d) PM-I with almost fully dispersed particles at $\Omega = 1.0\ rad/s$.

rotating wall as depicted in Fig. 4-9(b).

Segregation-I (S-I) : Further increase in the rotational velocity of the cylinder disturbs the core that is formed in the previous phase. Since light particles experience higher buoyancy, they remain in the vicinity of the cylinder wall segregated from the heavy particles. In contrast, heavy particles are more dispersed into the suspending fluid. Rotation of the cylinder drags either of the particles down but drag pushes them upwards as soon as they lose contact with the wall. As the particles reach near the top they set a clockwise current by displacing a few particles in the downward direction. A circulation which is developed near the top as a result is shown for S-I in Fig. 4-9(c). The segregation of light particles is more pronounced at higher density

ratios.

Partial Mixing (PM-I) : The light particle bed which exists in the first three phases is fully disturbed. The circulation which is developed at the top due to the upward movement of particles in S-I phase becomes fully blown in this phase. This is because those particles which are carried upwards by drag set an opposite current in the right portion of the cylinder moving the particles in the downward direction.

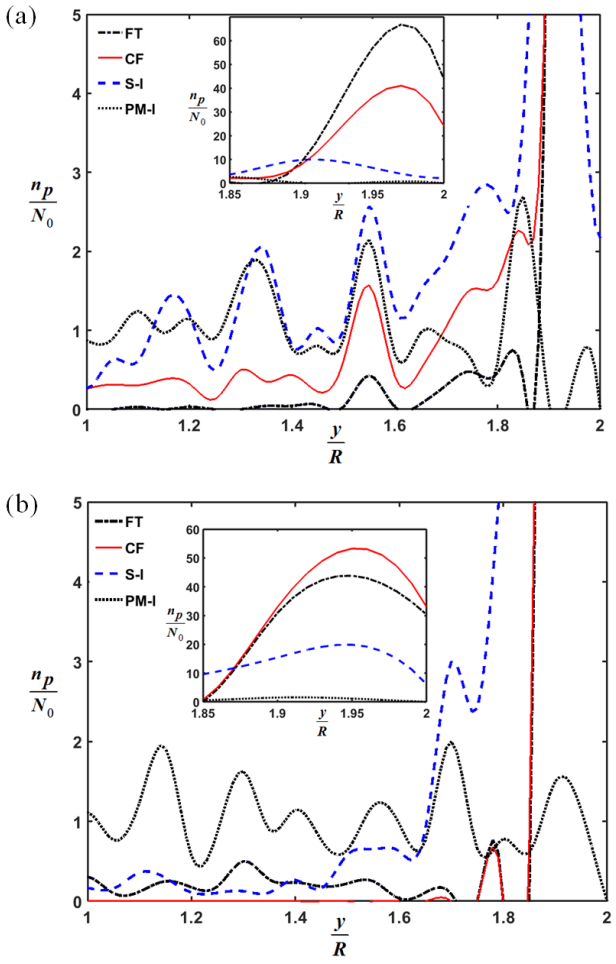

Figure 4-10: Number density plots in the gravity dominated regime for (a) light particles (b) heavy particles, here n_p and N_0 are the number of particles at steady state and $t = 0$ respectively.

For the floating system, radial particle distribution is quantitatively depicted by the number density plots for gravity and centrifugal force dominated regimes in the Figs. 4-10 and 4-12 respectively. Since the particles tend to move up the cylinder,

the number density is calculated from the centre to the top of the rotating cylinder denoted by values $1, 2$ on the x-axis. Since the particles form a bed at the top of the cylinder in contrast to the settling system, the peaks in the particle distribution graphs shift towards the right. Here it is noticeable that the overall behaviour of both heavy and light particles in either of the systems is identical in the gravity dominated regime.

Mixing (M) : In this phase both the heavy and the light particles are distributed homogeneously throughout the cylinder. The floating and settling systems show exact similarity in behaviour with each other and with the HR (homogeneous regime) phase in non-neutrally buoyant mono-disperse suspensions [34, 27, 18, 21] . From Fig. 4-9 and Fig. 4-11 we can observe how the phases range from segregated to mixed states and vice versa. This is the only phase where most of the particles (either heavy or light) have a common axis of rotation.

Partial Mixing - II (PM-II) : This phase marks the dominance of the centrifugal force on the particles. Since light particles experience greater centrifugal force compared to the heavy particles they are expected to start moving towards the centre sooner. The steady state configuration shown in Fig. 4-11(b) is as expected where the light particles start to percolate.

Segregation - II (S-II) : The centrifugal force further escalates the percolation of lighter particles in this phase. Though most of the light particles assemble around the centre there is also a thick cloud of heavy particles intertwined among the light particles. The dynamics of the light particles resemble the discontinuous banding (DB) phase as in the case of mono-disperse floating particles studied by Kalyankar et al. [18] and Konidena et al. [21].

Centrifugal Limit (CL) : An interesting observation from this phase is that the particles again experience core formation. In this phase, the light particles which now almost completely accumulate around the centre of the cylinder behave similarly to a

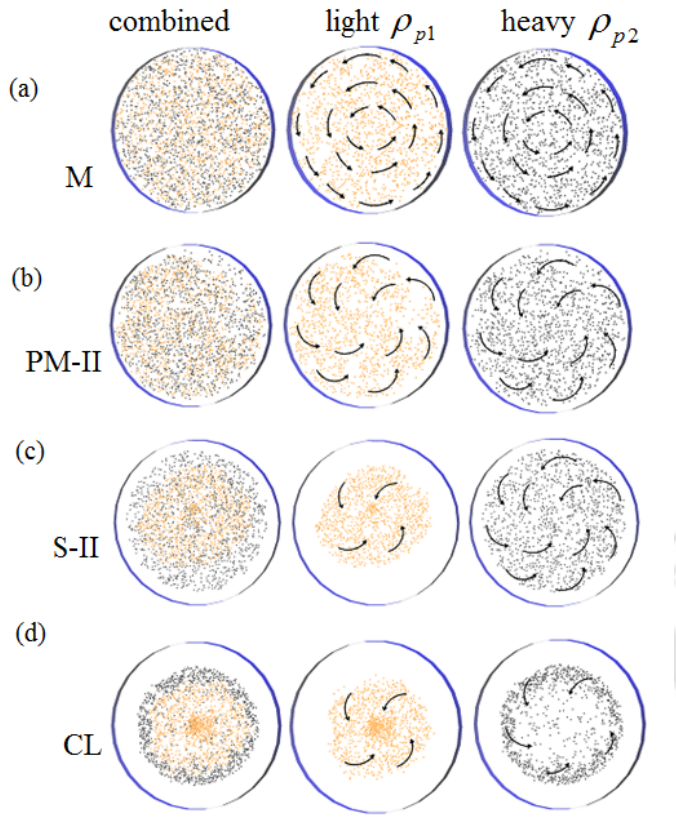

Figure 4-11: Phases exhibited with density ratio 2 when centrifugal force dominates (a) M at $\Omega = 1.0\ rad/s$ complete mixedness, (b) PM-II at $\Omega = 2.75\ rad/s$ inhomogeneous distribution of light particles, (c)S-II at $\Omega = 7\ rad/s$, (d) CL at $\Omega = 12\ rad/s$ maximum packed radial core.

mono-disperse system in centrifugal limit (CL) reported in Kalyankar et al. [18] and Konidena et al. [21]. However, the heavy particles get displaced from the centre and form a blanket around the light particles.

From the above results it can be observed that the influence of the predominant force among gravitational and centrifugal forces plays a significant role in the segregation or mixing of the floating system. These forces also play a major role in determining where the particles settle at steady state.

Axial Patterns

For a mono-disperse floating particle suspension in a horizontal rotating cylinder, it is already understood through experiments and numerical simulations [18, 21] that

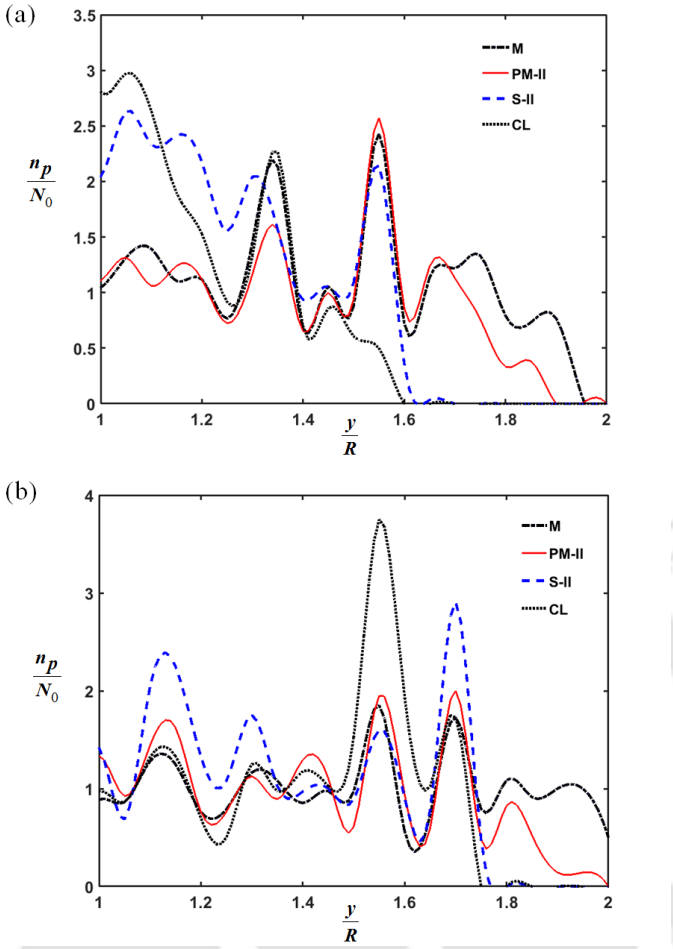

Figure 4-12: Number density plot for phases in the centrifugal force dominated regime (a) heavy particles (b) light particles, here n_p and N_0 are the number of particles at steady state and $t = 0$ respectively.

axial banding phenomenon is exhibited. Fluctuations in the radial particle density develop into inhomogeneous particle distribution which induce perturbations in the axial density profiles. However, the presence of axial banding for a bi-density floating system is yet to be established. All the simulation conditions for axial studies are same as that for the settling system described previously except for the density of particles.

Fig. 4-13 shows the axial profiles of light and heavy particles at 1050 rotations of the cylinder at $\Omega = 4.25\ rad/s$. The colour code, blue and orange correspond to particles moving right whereas silver and grey represent particles moving left. Due to this contrasting motion of the particles, the particles get arranged in alternate regions

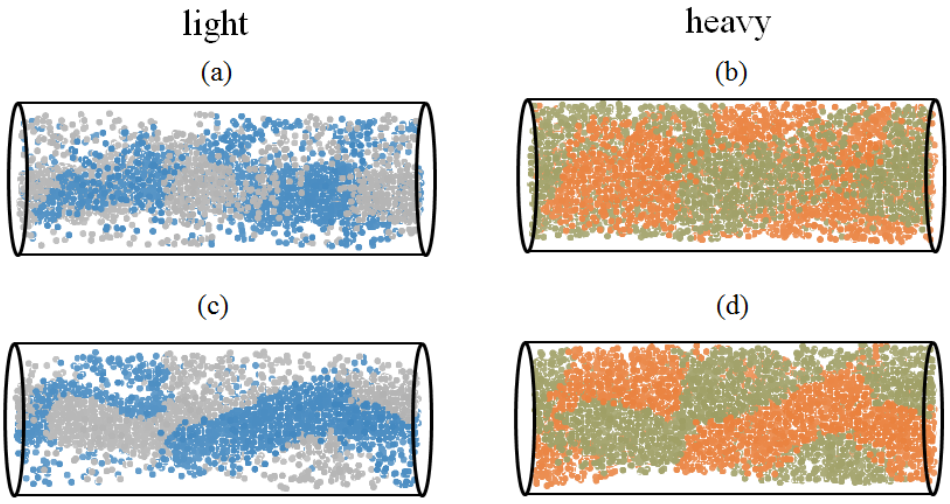

Figure 4-13: Axial configuration for floating system after 1050 rotations. Direction of gravity is into the plane of the paper in (a) and (b) implying a top view and is downward in (c) and (d) which represent front view. Blue and orange particles have rightward motion while silver and grey particles move leftwards.

of high and low concentrations depicted by Figs. 4-13(a) and 4-13(b) in a manner similar to the settling system. In the Figs. 4-13(c) and 4-13(d) the front view of the cylinder is shown which provides affirmation about secondary flows that aid band formation.

Axial number density profiles in Fig. 4-14(a) and 4-14(b) verify that there is exchange of a few particles between axial bands over the 200 rotations of the cylinder. Another interesting observation here is that bands are formed at the same location for either of the particles unlike suspensions of particles differing by size which exhibit band within band formation.

4.3.3 Scaling relations at phase transition boundaries

Knowledge of phases exhibited by the mono-disperse particle suspension in a rotating cylinder and their scaling properties at phase boundaries is available via the experimental and simulation studies in [34, 18, 21]. However, such information is not available for the bi-density systems (settling/floating) that are investigated in the present work.

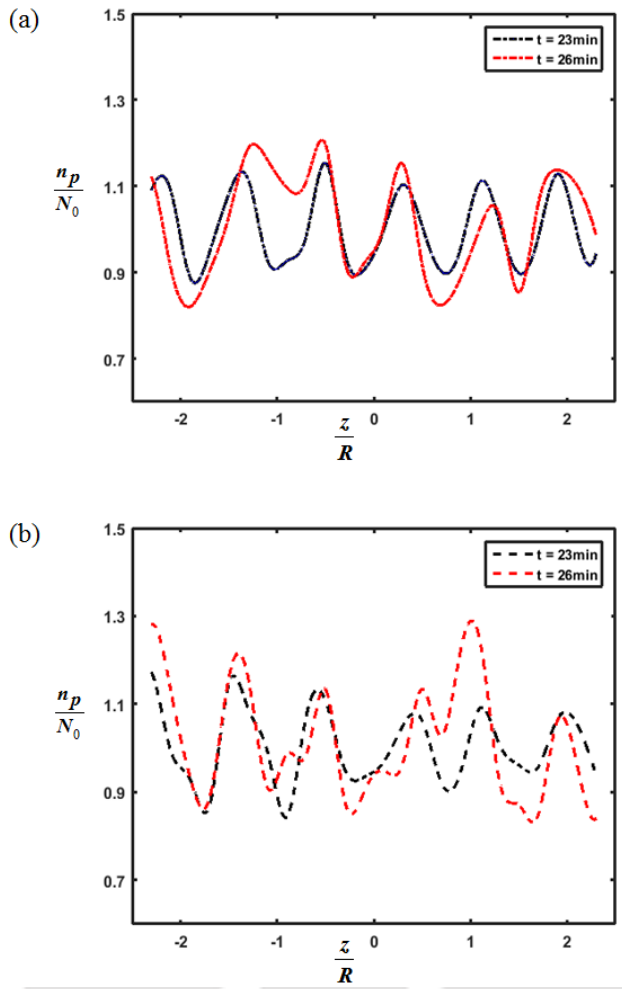

Figure 4-14: Number density profiles for the floating system in the axial direction at 850 and 1050 rotations of the cylinder for (a) light and (b) heavy particles at $\Omega = 4.25\ rad/s$, here n_p and N_0 are the number of particles at steady state and $t = 0$ respectively.

Since the task is to determine the scaling relations, we need to identify various dimensionless parameters. Let us consider a single particle held in a viscous fluid rotating in a horizontal cylinder. The motion of this particle is effected by three forces namely; gravitational, centrifugal and viscous drag. The buoyancy corrected mass of the particle $m_B = \pm(\rho_p - \rho_f)g$ changes sign depending on whether the system is settling or otherwise. The particle settling/floating velocity due to density difference between the particle and the fluid is $\pm(-U_s\hat{\boldsymbol{y}})$ where, $U_s = m_B g/(6\pi\mu a)$. Action of centrifugal force on the particle gives rise to centrifuging velocity $U_c(r/R)\hat{\boldsymbol{r}}$

where, $U_c = m_B\Omega^2 R/(6\pi\mu a)$.

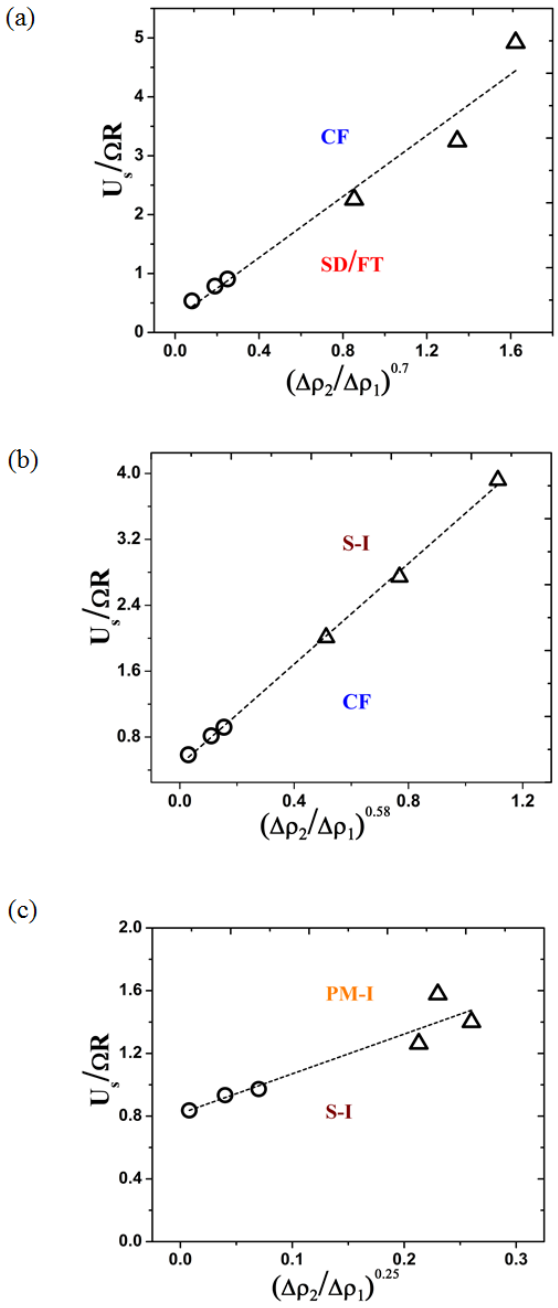

Figure 4-15: Transition boundaries for settling and floating systems in the gravity dominated regime. Open circles and triangles denote the floating and settling system, while the dotted line is a linear fit. (a) SD(FT)|CF (b) CF|S-I (c) S-I|PM-I.

Solving equation (2) on the particle located at $\boldsymbol{r}$ provides the velocity $\boldsymbol{U}$. This velocity $\boldsymbol{U}$ can be expressed in terms of two dimensionless numbers U_c/U_s and $U_s/\Omega R$

according to the relative magnitude of the three forces which the particle experiences.The components of this velocity resolved in the r, θ directions are given by

$$U_r = \begin{cases} U_s[(U_c/U_s)r/R - sin\theta], & \text{settling} \\ U_s[(U_c/U_s)r/R + sin\theta], & \text{floating} \end{cases} \tag{4.1}$$

$$U_\theta = \begin{cases} U_s[(\Omega R/U_s)r/R - cos\theta], & \text{settling} \\ U_s[(\Omega R/U_s)r/R + cos\theta], & \text{floating} \end{cases} \tag{4.2}$$

On substituting U_c and U_s into eq. (6) and eq. (7), the parameters $U_s/(\Omega R)$ and $g/(\Omega^2 R)$ are obtained. Fig. 4-15 and Fig. 4-16 illustrate how the phase boundaries scale with the change in density ratios for the two systems.

From the results of the radial studies, one can understand that a particle is not dispersed into the liquid once it overcomes the influence of the rotating wall in SD/FT, CF and S-I phases. Rather it follows a curvilinear path with almost fixed radius until it reaches back to the particle bed. The effect of U_θ would be prominent in this regime, hence variation of $U_s/(\Omega R)$ with the difference in density ratios provides information about phase transitions.

On the other hand, motion of the particle is in the radial direction when the centrifugal force has more influence. Therefore U_r would be prominent indicating that the variation of the dimensionless number $g/(\Omega^2 R)$ with the difference in density ratios gives the S-II|CL transition boundary. Figs. 4-15 and 4-16 represent the phase transition boundaries for gravitational and centrifugal regimes respectively. The observations from the radial studies that the two systems display similar characteristics when gravity dominates are supported by the linear fits in Fig. 4-15 for each of the boundary. Although there is resemblance among the settling and floating systems in the gravity dominated regime, an opposite behaviour in the centrifugal force dominant regime also is reflected in Fig. 4-16. This change in the sign of the slope for otherwise linear fits is attributed to the reversal in the action of centrifugal force.

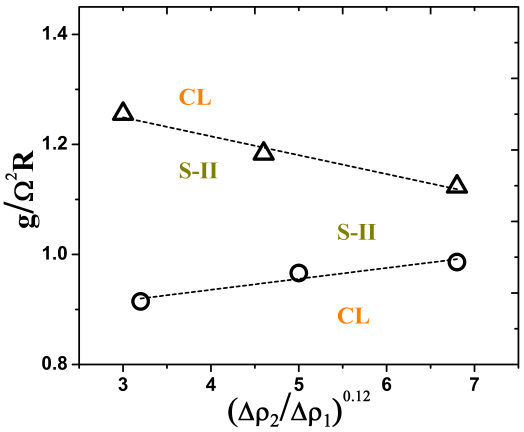

Figure 4-16: Transition boundaries for the systems in centrifugal force dominated regime S-II|CL. Open circles and triangles denote the floating and settling system, while the dotted lines are linear fits.

4.4 Summary

The simulation studies conducted in this work comprise of two kinds of bi-density suspensions; settling and floating particle systems rotating in a horizontal rotating cylinder. Several radial and axial investigations were performed using the method for N Stokeslets in a cylinder as described in [27]. The results display a wide spectrum of eight phases for both the systems, four each in the gravity and centrifugal force dominated regimes. Resemblance among the phases of the two systems in the gravity dominated regime is exhibited. However, a difference in behaviour is noticed when centrifugal force dominates owing to the change in direction of its action on settling and floating particles. It is also clearly established that it is the interplay between gravity, viscous drag and centrifugal forces which is responsible for the formation of distinct phases. An interesting aspect is that the systems also exhibit partial segregation and partial mixing phenomena in S-I,PM-I and PM-II,S-II phases. The scaling relations established between the governing forces expressed as dimensionless numbers and the ratio of buoyancy of the particles predicts certain phase transitions with considerable accuracy.

In the axial direction, the occurrence of alternate high and low concentration

particle bands takes place in both settling and floating systems. Formation of particle bands happens only when there is an inhomogeneous distribution of particles in the radial plane in a manner similar to the monodisperse suspension. This inhomogeneity in the radial plane excites fluctuations in the axial direction which grow into high particle concentration bands. Imbalance of forces is therefore the fundamental reason for this phenomenon. The imbalance may either be caused by the dominance of gravity or centrifugal force. There is no evidence of band within band formation which occur in systems which differ in particle size. This is because of the absence of any percolation effects for the bi-density systems considered in the current study.

Chapter 5

CFD Simulation of a buoyant suspension in horizontal rotating cylinder

5.1 Motivation

All experimental and simulation studies that are discussed earlier are confined only to the dilute suspension limit in the fully filled cylinder. Effect of higher concentration of particles on the axial band formation is also an area that could be investigated. Stokesian simulations for either of mono-disperse or the bi-density suspensions in Chapters 3 and 4, incorporated the point particle approach. However, if the finite size effects of the particle are to be included, the simulation becomes very complex owing to the higher order multipole terms involved (Stresslets). This difficulty could be overcome by the use of simulations based on the continuum model for particle transport.

5.2 Mathematical Model

The Suspension Balance Model proposed by [38] applies the principles of conservation of mass and momentum for both the fluid and the particle phases. The physical

concept of the SBM is that a non-homogeneous stress exists due to the presence of the particle phase in the suspension. This inhomogeniety induces the migration of particles in order to nullify itself. The suspension balance model is chosen over other shear-induced flux models as it is the least parametric and the most quantitative. For the bulk suspension, assuming the particle size is sufficiently large to bypass the effects of Brownian motion and the fluid is sufficiently viscous to neglect inertia, the steady state mass and momentum balance equations are written below:

$$\nabla.\boldsymbol{U} = 0, \tag{5.1}$$

$$\nabla.\boldsymbol{\Sigma} + \triangle\rho\boldsymbol{g}\phi = 0, \tag{5.2}$$

where, $\boldsymbol{U}$ is the velocity of the bulk suspension, $\boldsymbol{\Sigma}$ is the suspension stress. $\triangle\rho$ is the difference in the densities of the fluid ρ_f and the particle ρ_p and ϕ is the concentration of particles in the fluid. The mass conservation on the particle phase gives:

$$\frac{\partial\phi}{\partial t} + \nabla.\boldsymbol{U^p} = 0, \tag{5.3}$$

where, $\boldsymbol{U^p}$ is the velocity of the particle phase. In the absence of any other external forces apart from gravity, the particle momentum conservation gives:

$$\nabla.\boldsymbol{\Sigma^p} + n_p\langle\boldsymbol{F^H}\rangle_p + \triangle\rho\boldsymbol{g}\phi = 0, \tag{5.4}$$

The second term represents the product of the number density of the particles n_p with the average hydrodynamic force acting on the particle phase. The hydrodynamic force in the above equation is defined as:

$$\langle\boldsymbol{F^H}\rangle_p = -6\pi\eta a f^{-1}(\phi)(u_p - u_s), \tag{5.5}$$

where, $f(\phi)$ is the sedimentation hindrance function. On substituting equation (5.4) in equation (5.3) we arrive at the transport equation of the particle phase in the

suspension which is given by the equation below

$$\frac{\partial \phi}{\partial t} + \boldsymbol{U}.\nabla\phi = -\nabla.\vec{\boldsymbol{j_t}}, \tag{5.6}$$

$$\vec{\boldsymbol{j_t}} = \vec{\boldsymbol{j_\perp}} + \vec{\boldsymbol{j_g}}, \tag{5.7}$$

where $\vec{\boldsymbol{j_\perp}}$ represents the particle migration flux defined as:

$$\vec{\boldsymbol{j_\perp}} = \frac{2a^2}{9\eta_0} f(\phi)[\nabla.\Sigma^p], \tag{5.8}$$

and the additional flux term due to the effect of non-neutrally buoyant particle phase as detailed in [13] is given by:

$$\vec{\boldsymbol{j_g}} = \frac{2a^2}{9\eta_0} f(\phi)[\triangle\rho\boldsymbol{g}\phi], \tag{5.9}$$

The bulk stress of the suspension is obtained by the addition of the contributions from both the particle and the fluid stress.

$$\boldsymbol{\Sigma}_s = -\langle p\rangle_f \boldsymbol{I} + 2\eta_0 \boldsymbol{E} + \boldsymbol{\Sigma}_p, \tag{5.10}$$

where, $\langle p\rangle_f$ is the average pressure of the fluid. The fluid viscosity being η_0, $\boldsymbol{\Sigma}_p$ denotes particle stress. and $\boldsymbol{E} = (1/2)[\nabla u + (\nabla u)^T]$

Morris and Boulay [**?**] put forth an expression for the particle stress as:

$$\boldsymbol{\Sigma}_p = -\eta_0\eta_p(\phi)\dot{\gamma}\boldsymbol{Q} + 2\eta_0\eta_p(\phi)\boldsymbol{E}, \tag{5.11}$$

In the equation given above, the fluid contribution to the shear stress is $2\eta_0\boldsymbol{E}$ whereas the particle contribution is $\eta_0\eta_p\boldsymbol{E}$. The bulk shear viscosity is therefore $2\eta_0\boldsymbol{E}(1+\eta_p) = 2\eta_0\eta_r(\phi)\boldsymbol{E}$ and finally the bulk shear viscosity is $\eta_s = \eta_0(1+\eta_p) = \eta_0\eta_r(\phi)$ For the bulk suspension viscosity, the relation given by Krieger [22]

$$\eta_r(\phi) = (1 - \frac{\phi}{\phi_m})^{-1.82} \tag{5.12}$$

where, ϕ_m is the maximum packing fraction of the particles in the suspension. Contribution of the particle to the normal stress is given by $\eta_n \dot{\gamma} Q$, where η_n is the normal shear stress viscosity given below:

$$\eta_n = 0.75(\frac{\phi}{\phi_m})^2(1 - \frac{\phi}{\phi_m})^{-2} \tag{5.13}$$

The parameter which Q takes into account the anisotropy of the normal stresses is represented as:

$$Q = \begin{pmatrix} 1 & 0 & 0 \\ 0 & \lambda_2 & 0 \\ 0 & 0 & \lambda_3 \end{pmatrix}$$

where, $\lambda_2 = 0.8$ and $\lambda_3 = 0.5$. The principle directions in the expression for Q are flow, gradient and vorticity directions respectively. Therefore, the complete bulk stress is written as,

$$\boldsymbol{\Sigma}_p = -P\boldsymbol{I} + 2\eta_0\eta_s\boldsymbol{E} + \boldsymbol{E}_P^{NS}, \tag{5.14}$$

$\boldsymbol{E}_P^{NS}$ is the particle phase normal stress.

The details of the CFD algorithm used in OpenFOAM are provided here. The system of equations given by the equations 5.1, 5.2 and 5.5 is implemented by modifying the 'buoyantBossinesqPimpleFoam solver' in OpenFOAM to a new solver which represents the modified Suspension Balance Model (SBM) to include the effect of gravity. The equations 5.1 and 5.2 in the thesis which describe the behaviour of the flow are solved iteratively using PIMPLE algorithm.

The steps in the algorithm are given below:

i) Start time loop

ii) Include PISOcontrols and CourantNo

iii) Read input parameter values and calculate values of other parameters like $\eta_0, \eta_s, \eta_p, \Sigma^f, \Sigma^p, \Sigma$, etc.

iv) In the pressure-velocity PIMPLE iterations, solve the Stokes momentum equation and apply velocity-pressure correction to satisfy the continuity equation.

v) At each time step, the transport equation given by equation 5.5 in the thesis is solved.

vi) The process is iterated until steady state is attained.

5.3 Simulation set-up

A representation of the particles suspended in a horizontal cylinder is shown in the diagram in Fig. 5-1 with x-axis being the axis of rotation. Since the particles are positively buoyant, we can see that at the start of the simulation the particle phase is concentrated near the top of the cylinder. It is well known that the Suspension Balance Model (SBM) is applicable only when the system is in the Stokes flow regime. Therefore, simulations are run at low rotational velocities of the cylinder. Though the Stokes equations are deviod of the unsteady term, it was still added to the momentum equation for stability of the simulation and also to increase the diagonal dominance of the matrix. All the simulations were carried out using the open source CFD software OpenFOAM [49]. The modified SBM with the inclusion of gravity effects and to study the occurance of axial banding in settling suspensions was performed initially by Shadab and Singh [13]. The velocity-pressure coupling was done via the PIMPLE algorithm.

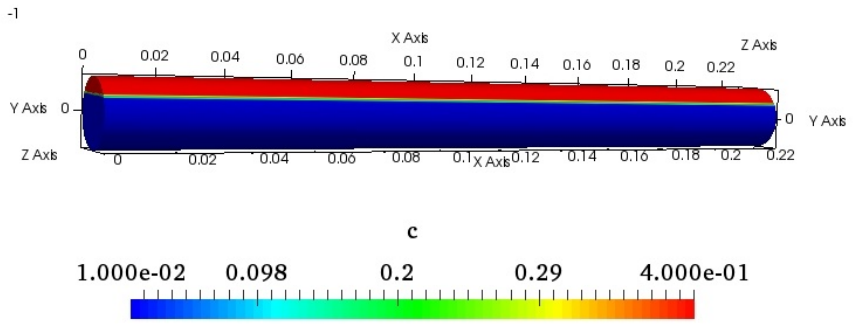

Figure 5-1: Initial concentration distribution of the buoyant particle system in a rotating cylinder.

The rotating cylinder geometry is discretized by a structured mesh which contains

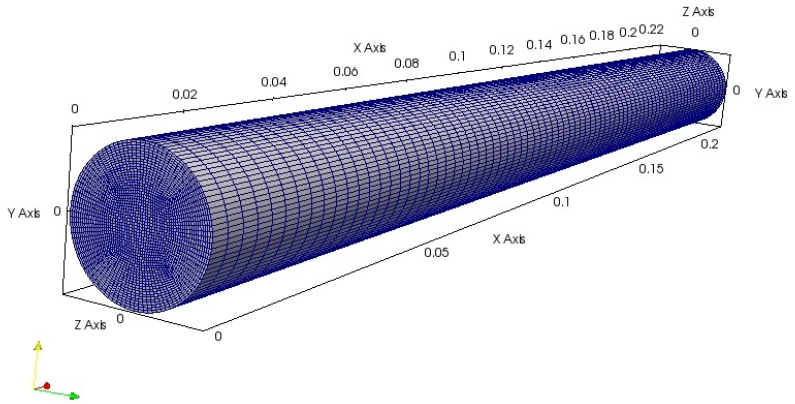

Figure 5-2: Hexahedral mesh of the computational geometry.

189600 hexadral cells as shown in the Fig. 5-2. The geometry is prepared according to the conditions of the experiments done by Kalyankar et al. [18] for a buoyant system as described in Chapter 3. The simulation parameters for the geometry are tabulated below. A rotating wall boundary condition is imposed on the wall of the cylinder. Zero flux condition is applied on the walls and surface of the cylinder. The fixedFluxPressure boundary condition is used for the pressure since the systems experiences body forces in the form of gravitational force. In order to check the evolution of bands for high concentrated suspensions an initial average volume fraction of the suspension was ~ 0.20.

S.No	Parameter	Symbol[Unit]	Value
1	Particle radius	$a[\mu$ m]	100
2	Fluid viscosity	μ_f $[cP]$	55
3	Particle density	ρ_p [g/cc]	0.3
4	Fluid density	ρ_f[g/cc]	1.160
5	Pipe radius	R [cm]	1
6	Pipe Length	L [cm]	22.7

Table 5.1: Geometry details and simulation parameters for buoyant system.

5.4 Results and Discussion

In this section, the results obtained from the numerical simulations for the concentrated suspension system rotating in a horizontal cylinder are discussed. It was established earlier through discrete particle simulations that for the axial banding phenomenon to surface, the distribution along the radial plane should be inhomogeneous. It should also be noted that the validity of the SBM is only in the Stokes flow regime. In that connection, a few simulations were performed along the radial plane to ensure that the particle distribution is non-uniform for a certain rotational velocities of the cylinder. The velocities at which the particle distribution is as desired are noted and applied for the simulations in the axial plane. Possibility of concentrated suspensions to form axial bands is tested in this work.

Fig. 5-3 describes various phase characteristics of a suspension at low rotational velocities of the cylinder. The average concentration of this short cylinder for observations on the radial plane is ~ 0.15 and initially the particle phase is floating near the top section of the cylinder. The concentration contours suggest that the particle phase transits from a segregated state to a mixed state. One can notice that the dynamical centre of the system which initially was on the right section of the cylinder gradually moves leftwards displaying a transition. These contours indicate that the axial concentration bands could be formed around 1.75 rad/s.

For a buoyant particle suspension, the Stable Band (SB) phase occurs after the Homogeneous region (HR) unlike the case of a settling suspension [18, 21]. Therefore, from the above discussion, we can say that if at all there is a possibility of forming axial bands then they would lie in the Low-Transition rate (LT) regime. The LT phase is characterized by axial bands without any form of axial movement. Fig. 5-4 shows the front view of snapshots of the suspension undergoing the axial banding phenomenon. It can also be observed that the particle bands which are formed do not travel along the axial direction. The number of bands become more prominent but the local concentration of each band is reduced as particle phase slowly mixes in the overall suspension.

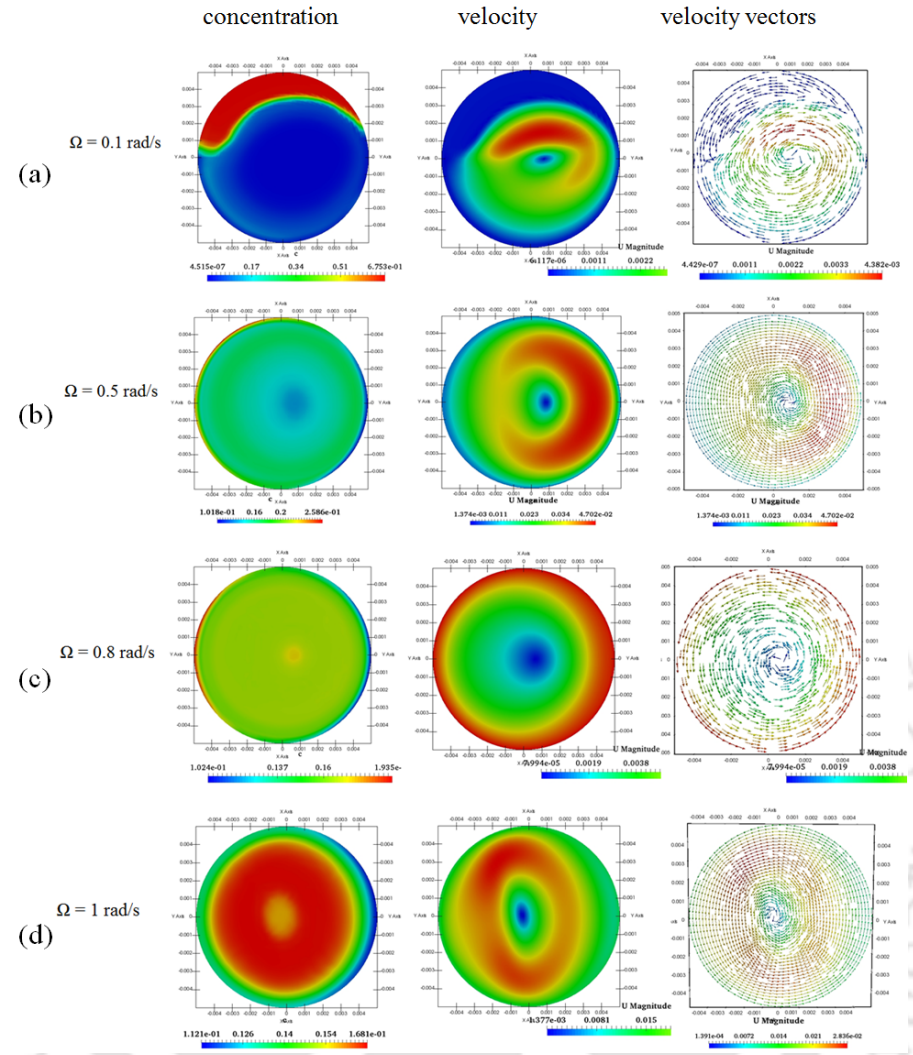

Figure 5-3: Concentration and velocity contours along with the velocity vectors for a 2D cylinder at different rotational velocities. (a) Low rotational velocity of the cylinder pushes the particle phase upwards, (b) Particle bed is absent with dynamical centre of the system in the right section of the cylinder, (c) High concentration region is displaced along the wall but not homogeneously mixed, (d) Almost uniformly mixed suspension at a velocity of 2 rad/s

Fig. 5-5 gives the concentration snapshots of the system from the rear view of the cylinder. It is clearly observable that the concentration bands on the rear side are stronger than those formed on the front side. This is exactly opposite to the observations of a settling system. This can be attributed to the opposing direction of motion of the settling and floating particle phases. As the formed particle bands evolve through time, the rear view bands grow stronger whereas it is vice-versa for

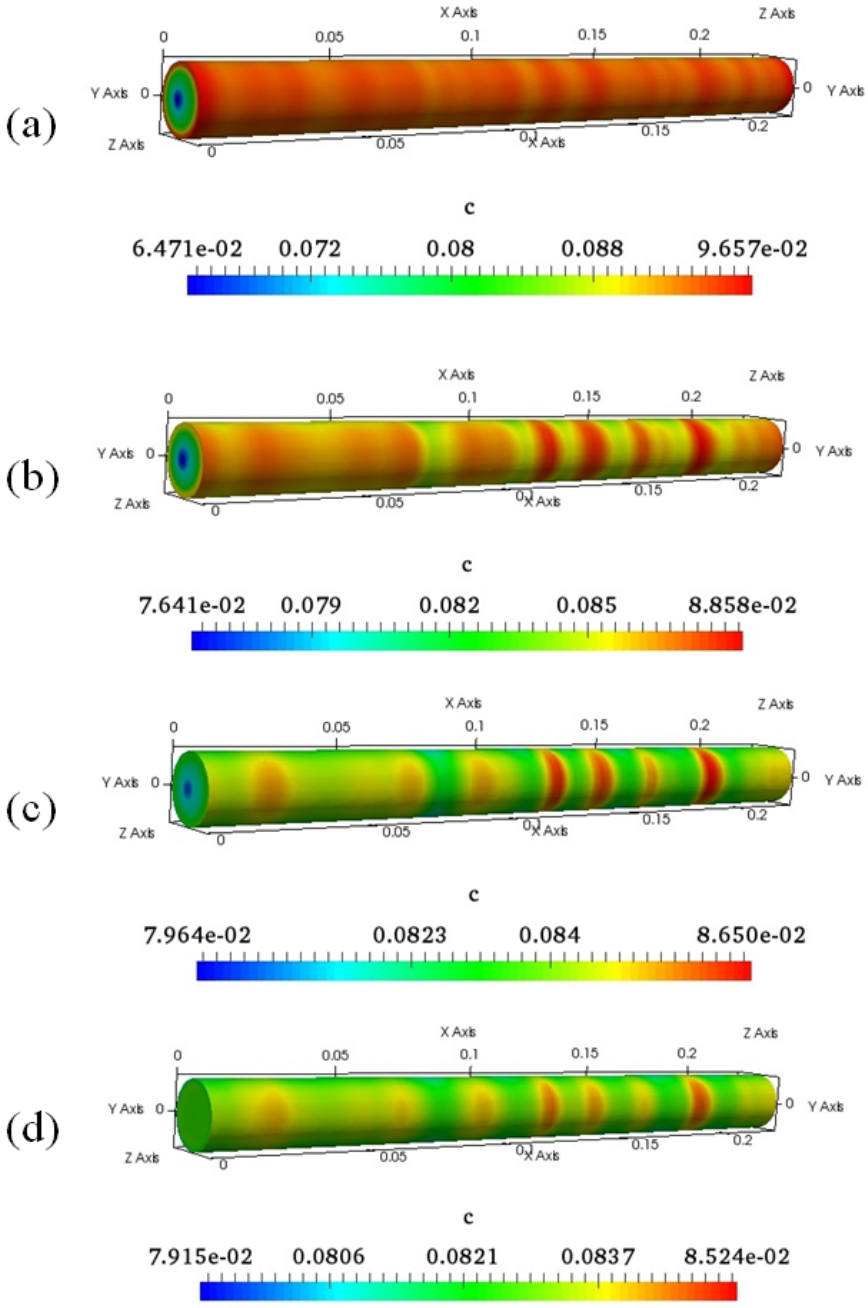

Figure 5-4: Snapshots of the concentration along the axial plane at different rotations of the cylinder n (a) 460 rotations (b) 500 rotations (c) 550 rotations (d) 650 rotations.

the system from the front view.

The concentration profiles in the Fig. 5-6(a) and Fig. 5-7(a) for the front and the rear view respectively provide a quantitative evidence of the formation of axial

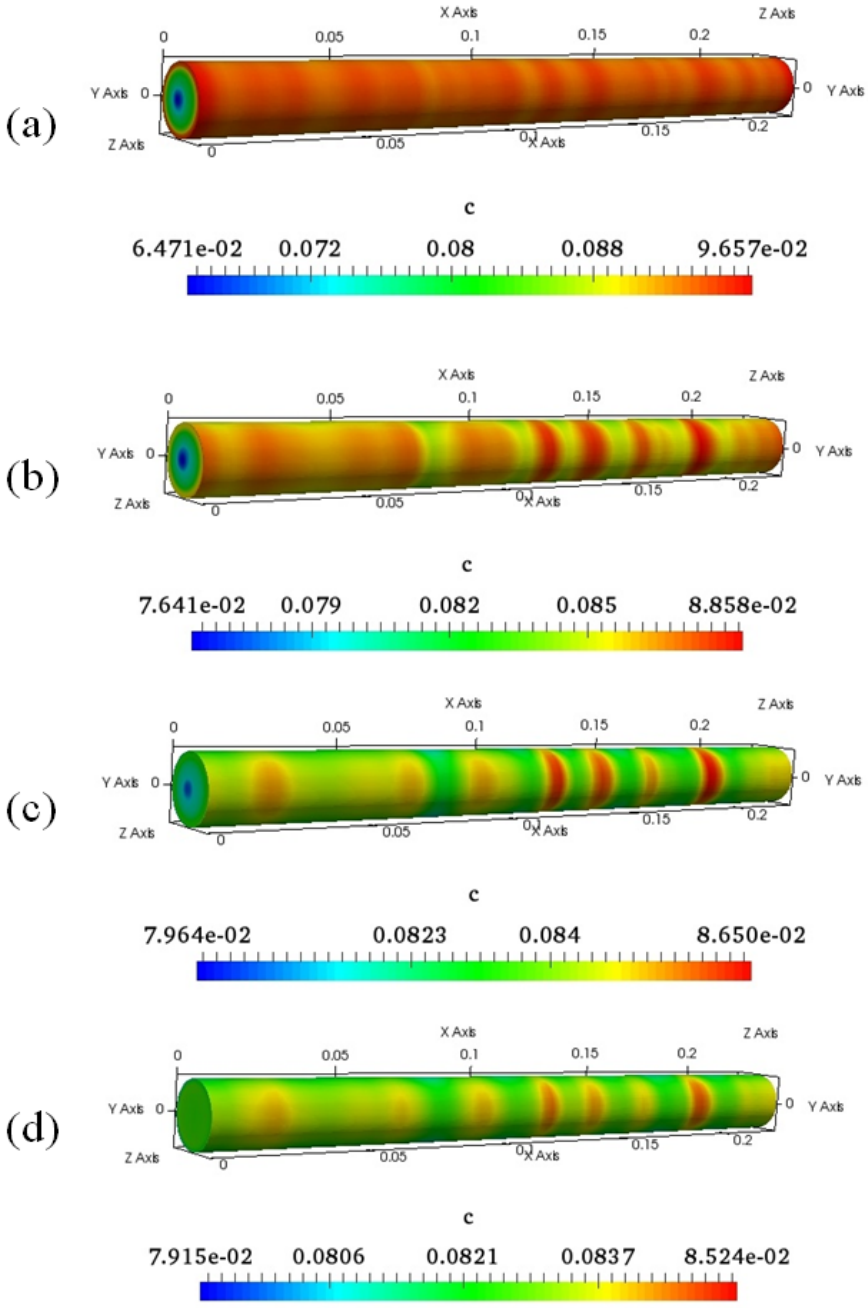

Figure 5-5: Snapshots of the concentration along the axial plane at different rotations of the cylinder n (a) 460 rotations (b) 500 rotations (c) 550 rotations (d) 650 rotations.

bands. The banding phenomena does not take place until nearly 500 rotations of the cylinder. The bands which are formed do not remain with the same concentration over the entire duration of the simulation. It can be observed that the band patterns

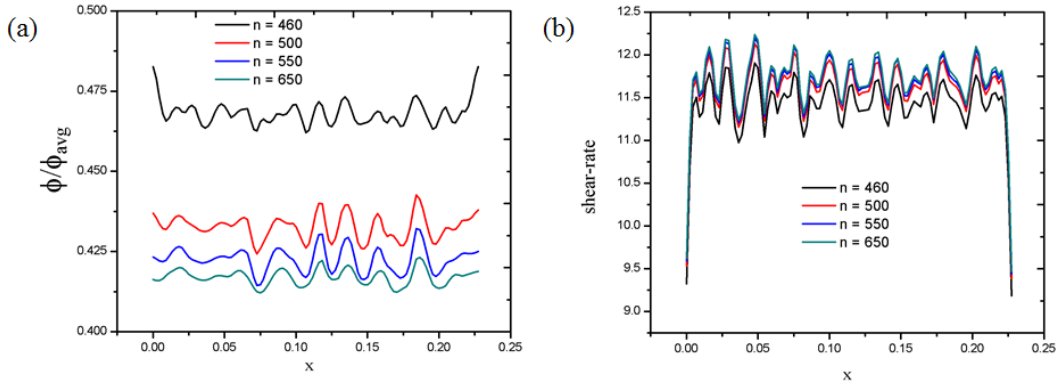

Figure 5-6: concentration and shear-rate profiles of the suspension in the front view for different rotations of the cylinder n(a) concentration profiles (b) shear-rate profiles.

get diluted over time but are not completely destroyed. However, in Fig. 5-7(a) it can be seen that the bands seen from the rear view also decrease in the overall concentration but grow strong locally. The shear-rate profiles shown in Figs. 5-6(b) and 5-7(b) also show the variations of shear-rate along the axial bands.

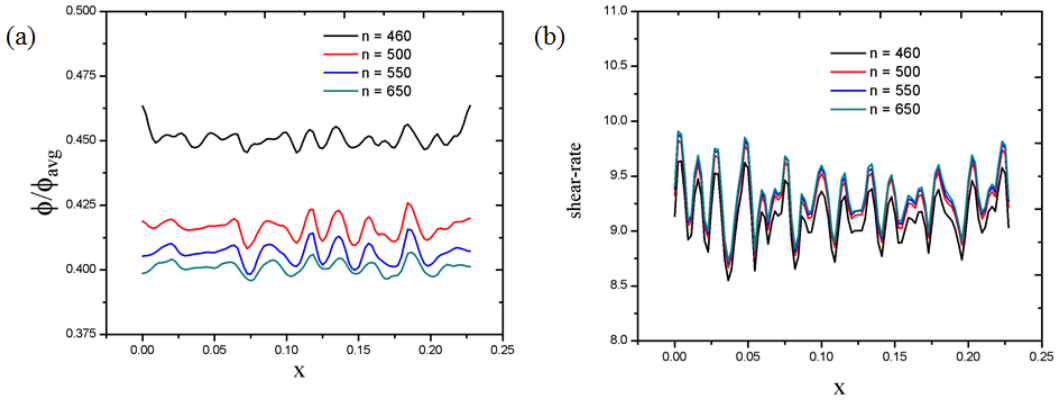

Figure 5-7: concentration and shear-rate profiles of the suspension in the front view for different rotations of the cylinder n(a) concentration profiles (b) shear-rate profiles.

Another interesting observation of the system is the variation of particle phase concentration along the central axis. The geometry is sliced along the z-normal to obtain the necessary view. The different slices correspond to the rotations of the cylinder as shown in Fig. 5-8. As the cylinder rotates, gradually the particle phase is

dragged along just the walls of the cylinder. Due to this the cylinder centre becomes devoid of the particle phase. After certain rotations of the cylinder, particle phase in the top section of the cylinder starts to interact with that in the lower section of the cylinder at various regions along the axis. Fig. 5-8(b) implies that at higher number of rotations of the cylinder, the regions at which the particle phase interacts with itself becomes stronger in concentration. Gradually these concentration fluctuations get amplified into axial bands. We have seen in Fig. 5-4 and Fig. 5-5 that the concentration of the axial bands decreases gradually, but the slices at the centre of the cylinder show an increase in concentration. This could be because the particles are positively bouyant and move towards the cylinder centre at higher rotational velocities.

Since only a few of the axial bands are evenly placed, this region may not belong to the Stable Band regime as discussed in [18]. It can be said that the region is similar to the Low-Transition (LT) phase which appears before the Homogeneous regime.

5.5 Summary

We have performed continuum simulations by applying the SBM proposed by [38]. Most of the simulation parameters are similar to those in the experiments of [18]. However, since knowledge of the axial segregation/mixing phenomenon for concentrated suspensions is not yet provided, the average concentration of the particle phase was maintained to be ~ 0.2. From the simulations done in the radial plane, the range in which there is a possibility for the suspension to form axial bands was investigated. The simulation were able to predict axial banding patterns for concentrated suspensions. The bands were found to grow internally (towards the centre) with the band concentration on the wall diminishing. Further studies by varying particle radius, concentration or even the shape of the outer cylinder could provide better insights into the mechanism of axial patterns.

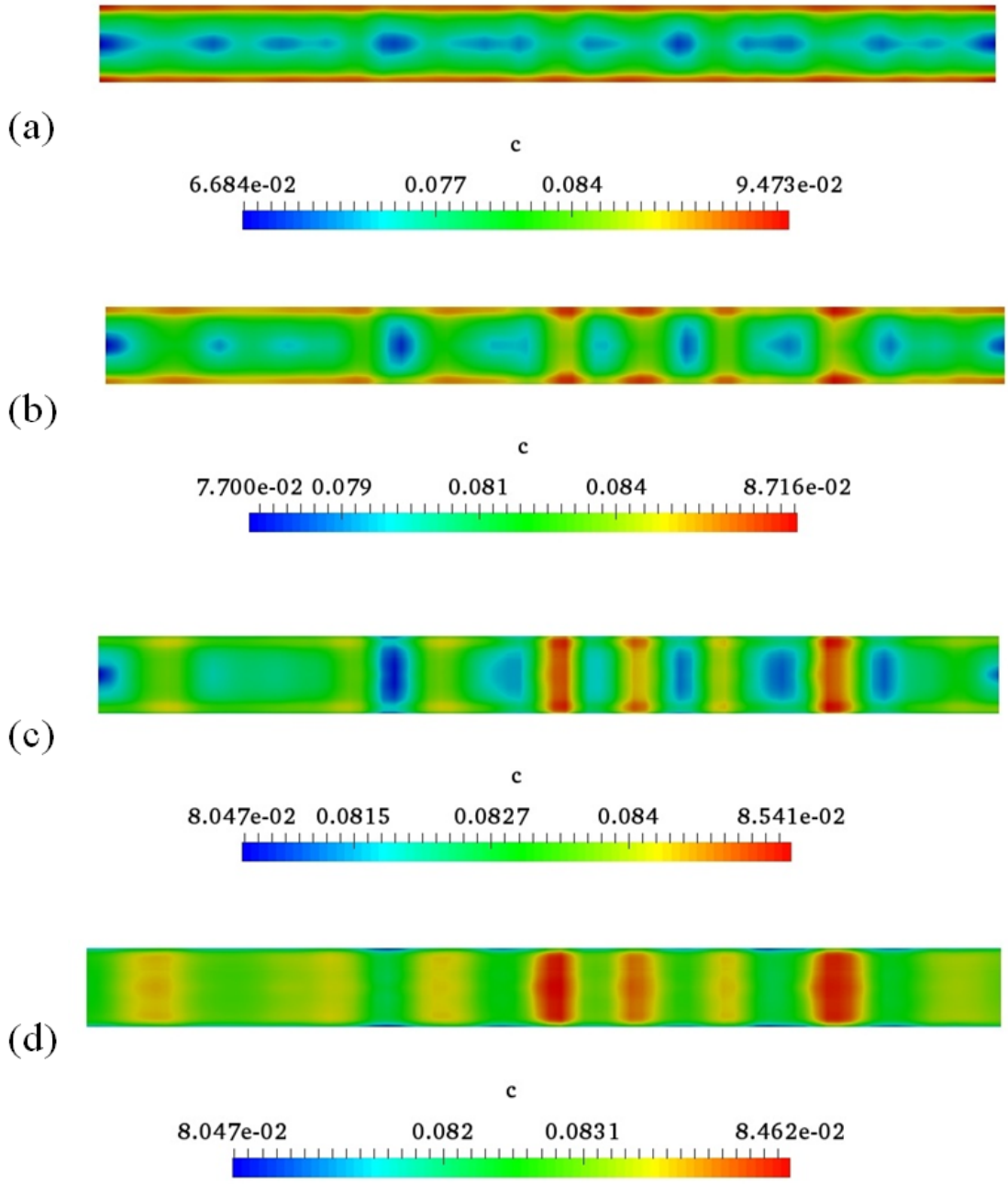

Figure 5-8: Slices of the rotational geometry corresponding to the various rotations of the cylinder n (a) 460 rotations (b) 500 rotations (c) 550 rotations (d) 650 rotations.

भारतीय प्रौद्योगिकी संस्थान गुवाहाटी
Indian Institute of Technology Guwahati

Chapter 6

Conclusions and Future Scope

In this current work, we dealt with comprehending the characteristic behaviour of suspensions in fully filled horizontal rotating cylinders. Initially a monodisperse positively buoyant suspension was investigated. In further study, two kinds of suspensions namely settling and positively buoyant were explored. From the literature one can understand that the reported works are limited to dilute suspensions, the effect of higher concentration of suspensions in fully filled rotating cylinders is also probed in the current work. We have performed both discrete particle and continuum simulations to understand the dynamics of particle laden fluids in horizontal rotating cylinders. The suspension systems studied in this thesis behave like pure fluids in a few cases and like dry granular matter under other conditions.

As detailed in the Chapter 3, the patterns obtained for a positively buoyant suspension in rotating cylinder are in good quantitative and qualitative agreement with the experiments of [18]. Though we could reproduce most of the patterns obtained in the experiments of Kalyankar et al. [18] in the axial and radial direction but the discontinuous banding phase could not be reproduced. This could be becasue in this phase, the concentration increases high as steady state approaches. Exclusion of lubrication interactions along with the finite size effects in the point particle formulation could be a reason for DB phase not getting reproduced.

In the case of bidensity suspension filling the rotating cylinder, we investigated two systems namely settling and floating. As the name of the system indicates, settling

implies that particles are denser than the carrier fluid. In contrast, for the floating system, suspended particles are lighter than the fluid. We could identify as many as eight different phases for the two systems. It can be concluded from our work that the behaviour of both systems is similar in nature when the gravitational force is dominating. However, the systems show opposing behaviour when the centrifugal force is dominating. Also for a bi-dispersed particle suspension, the particle size effects could produce different dynamics than the bi-density suspensions. Therefore, inclusion of lubrication interactions and/or finite size effects of the particle radius could be done though being highly complex. The effect of end-walls on the radial or axial patterns formed was nullified in the simulations with the usage of a periodic boundary condition. However, in dry granular media and for bi-disperse suspensions, it is known that the band formation starts to form from the end-walls. This mechanism of band formation could be altered by the presence of walls.

Using a continuum model developed with the concept of shear induced migration, we could investigate the influence of higher concentration of the suspension in the rotating cylinder. The cylinder had rotating end-walls instead of the periodic boundary condition used in the case of discrete modelling. With the help of the continuum model we can further investigate about the mixing/segregation properties of suspensions in various other geometries like rectangular channel etc., and include the effect of size of the particles too. An interesting investigation would be to find a unifying mechanism for the band formation of the particles in rotating cylinders.

Further studies can be extended to numerically analyse and provide the underlying mechanism for suspensions partially filling the rotating cylinders. The effect of the container shape on axial segregation was reported only in the case of dry granular systems. However, the influence of container shape on the (de)mixing of suspensions is also yet to be explored. Though several experimental investigations as reported in table 2 of Chapter 1 probed in to the axial banding phenomenon not much theoretical or numerical studies are performed. One can easily identify from the work reported earlier that both dry and wet granular matter irrespective of the fill level of the cylinder (under various conditions) exhibit the axial segregation or banding

phenomenon. It would also be interesting to investigate for a unifying mechanism for the band formation in both wet and dry granular matter. Recent advances in understanding the similarity in nature between dry granular matter and suspensions could provide direction in providing a unifying mechanism for the band formation.

भारतीय प्रौद्योगिकी संस्थान गुवाहाटी
Indian Institute of Technology Guwahati

Appendix A

Appendix

भारतीय प्रौद्योगिकी संस्थान गुवाहाटी
Indian Institute of Technology Guwahati

Bibliography

[1] O. A. M. Boote and P. J. Thomas. Effects of granular additives on transition boundaries between flow states of rimming flows. *Phys. Fluids*, 11(8):2020–2029, 1999.

[2] A. P. J. Breu, C. A. Kruelle, and I. Rehberg. Pattern formation in a rotating aqueous suspension. *EPL (Europhys. Lett.)*, 62(4):491, 2003.

[3] A. P. J. Breu, C. A. Kruelle, and I. Rehberg. Oscillatory patterns in a rotating aqueous suspension. *The European Physical Journal E*, 13(2):189–196, 2004.

[4] Hui Chen, Xian qiong Zhao, You gang Xiao, Yi lun Liu, and Ying Liu. Radial mixing and segregation of granular bed bi-dispersed both in particle size and density within horizontal rotating drum. *Transactions of Nonferrous Metals Society of China*, 26(2):527 – 535, 2016.

[5] Huang Decai, Lu Ming, Sun Gang, Feng Yaodong, Sun Min, Wu Haiping, and Deng Kaiming. Ringlike spin segregation of binary mixtures in a high-velocity rotating drum. *Phys. Rev. E*, 85:031305, Mar 2012.

[6] Yi Fan and K. M. Hill. Phase transitions in shear-induced segregation of granular materials. *Phys. Rev. Lett.*, 106:218301, May 2011.

[7] Rama Govindarajan, Prabhu R. Nott, and Sriram Ramaswamy. Theory of suspension segregation in partially filled horizontal rotating cylinders. *Phys. Fluids*, 13(12):3517–3520, 2001.

[8] R. E. Hampton, A. A. Mammoli, A. L. Graham, N. Tetlow, and S. A. Altobelli. Migration of particles undergoing pressure-driven flow in a circular conduit. *J. Rheol.*, 41(3):621–640, 1997.

[9] Minsoo Han, Chongyoup Kim, Minchul Kim, and Soonchil Lee. Particle migration in tube flow of suspensions. *J. Rheol.*, 43(5):1157–1174, 1999.

[10] J. Happel and H. Brenner. *Low Reynolds Number Hydrodynamics*. Prentice Hall Inc., 2004.

[11] K. M. Hill, G. Gioia, and D. Amaravadi. Radial segregation patterns in rotating granular mixtures: Waviness selection. *Phys. Rev. Lett.*, 93:224301, Nov 2004.

[12] Daniel C. Hong, Paul V. Quinn, and Stefan Luding. Reverse brazil nut problem: Competition between percolation and condensation. *Phys. Rev. Lett.*, 86:3423–3426, Apr 2001.

[13] Shadab Ilahi. Numerical simulation of particle migration and axial segregation in rotating suspension. Master's thesis, Indian Institute of Technology, Guwahati, 2017.

[14] Akshat Jain, Anugrah Singh, and John F Brady. Radial segregation of settling suspension in horizontally rotating cylinder. *IUTAM Symposium on Mobile Particulate Systems, Bangalore, India*, 2012.

[15] Nitin Jain, Julio M. Ottino, and Richard M. Lueptow. Combined size and density segregation and mixing in noncircular tumblers. *Phys. Rev. E*, 71:051301, May 2005.

[16] Bo Jin and Andreas Acrivos. Rimming flows with an axially varying viscosity. *Phys. Fluids*, 16(3):633–640, 2004.

[17] D. D. Joseph, J. Wang, R. Bai, B. H. Yang, and H. H. Hu. Particle motion in a liquid film rimming the inside of a partially filled rotating cylinder. *J. Fluid Mech.*, 496:139–163, 2003.

[18] Makrand G. Kalyankar, W. R. Matson, Penger Tong, and Bruce J. Ackerson. Pattern formation in a rotating suspension of non-brownian buoyant particles. *Phys. Fluids*, 20(8):083301, 2008.

[19] D. V. Khakhar, J. J. McCarthy, and J. M. Ottino. Radial segregation of granular mixtures in rotating cylinders. *Phys. Fluids*, 9(12):3600–3614, 1997.

[20] Christopher J. Koh, Philip Hookham, and L. G. Leal. An experimental investigation of concentrated suspension flows in a rectangular channel. *J. Fluid Mech.*, 266:1–32, 1994.

[21] Sudarshan Konidena, Jonghoon Lee, K. Anki Reddy, and Anugrah Singh. Particle dynamics and pattern formation in a rotating suspension of positively buoyant particles. *Phys. Rev. Fluids*, 3:044301, Apr 2018.

[22] Krieger. Rheology of monodisperse lattices. *Adv. Colloid Interface Sci.*, 3:111–136, 1972.

[23] Gokul P. Krishnan, Shannon Beimfohr, and David T. Leighton. Shear-induced radial segregation in bidisperse suspensions. *J. Fluid Mech.*, 321:371–393, 1996.

[24] A. Ashok Kumar and Anugrah Singh. Dynamics of bi-dispersed settling suspension of non-colloidal particles in rotating cylinder. *Advanced Powder Technology*, 21(6):641 – 651, 2010.

[25] Jonghoon Lee and Anthony J. C. Ladd. Axial segregation in a cylindrical centrifuge. *Phys. Rev. Lett.*, 89:104301, 2002.

[26] Jonghoon Lee and Anthony J. C. Ladd. Axial segregation of a settling suspension in a rotating cylinder. *Phys. Rev. Lett.*, 95:048001, Jul 2005.

[27] Jonghoon Lee and Anthony J. C. Ladd. Particle dynamics and pattern formation in a rotating suspension. *J. Fluid Mech.*, 577:183–209, 2007.

[28] S. G. Lipson. Periodic banding in crystallization from rotating supersaturated solutions. *J. Phys. Condens. Matter*, page 5001, 2001.

[29] N. Liron and R. Shahar. Stokes flow due to a stokeslet in a pipe. *J. Fluid Mech.*, 86(4):727–744, 1978.

[30] M. K. Lyon and L. G. Leal. An experimental study of the motion of concentrated suspensions in two-dimensional channel flow. part 1. monodisperse systems. *J. Fluid Mech.*, 363:25–56, 1998.

[31] M. K. Lyon and L. G. Leal. An experimental study of the motion of concentrated suspensions in two-dimensional channel flow. part 2. bidisperse systems. *J. Fluid Mech.*, 363:57–77, 1998.

[32] J. Blawzdziewicz M. Zurita-Gotor and E. Wajnryb. Swapping trajectories: A new wall-induced cross-streamline particle migration mechanism in a dilute suspension of spheres. *J. Fluid Mech.*, 592:447, 2007.

[33] W. R. Matson, B. J. Ackerson, and P. Tong. Pattern formation in a rotating suspension of non-brownian settling particles. *Phys. Rev. E*, 67:050301, May 2003.

[34] W. R. Matson, B. J. Ackerson, and P. Tong. Measured scaling properties of the transition boundaries in a rotating suspension of non-brownian settling particles. *J. Fluid Mech.*, 597:233–259, 2008.

[35] W. R. Matson, M. Kalyankar, B. J. Ackerson, and P. Tong. Concentration and velocity patterns in a horizontal rotating suspension of non-brownian settling particles. *Phys. Rev. E*, 71:031401, Mar 2005.

[36] Shahin Navardi and Sukalyan Bhattacharya. General methodology to evaluate two-particle hydrodynamic friction inside cylinder-bound viscous fluid. *Comput Fluids.*, 76:149 – 169, 2013.

[37] Shahin Navardi, Sukalyan Bhattacharya, and Hanyan Wu. Stokesian simulation of two unequal spheres in a pressure-driven creeping flow through a cylinder. *Comput Fluids.*, 121:145 – 163, 2015.

[38] Prabhu R. Nott and John F. Brady. Pressure-driven flow of suspensions: simulation and theory. *J. Fluid Mech.*, 275:157âĂŞ199, 1994.

[39] Raphael Pesche, Georges Bossis, and Alain Meunier. Numerical simulation of particle segregation in a bidisperse suspension. working paper or preprint, June 1998.

[40] Ronald J. Phillips, Robert C. Armstrong, Robert A. Brown, Alan L. Graham, and James R. Abbott. A constitutive equation for concentrated suspensions that accounts for shear induced particle migration. *Phys. Fluids A: Fluid Dynamics*, 4(1):30–40, 1992.

[41] P. Raiskinmäki, J. A. Åström, M. Kataja, M. Latva-Kokko, A. Koponen, A. Jäsberg, A. Shakib-Manesh, and J. Timonen. Clustering and viscosity in a shear flow of a particulate suspension. *Phys. Rev. E*, 68(6):061403, December 2003.

[42] Arun Ramachandran and David T. Leighton. The influence of secondary flows induced by normal stress differences on the shear-induced migration of particles in concentrated suspensions. *J. Fluid Mech.*, 603:207–243, 2008.

[43] G. Seiden, M. Ungarish, and S. G. Lipson. Formation and stability of band patterns in a rotating suspension-filled cylinder. *Phys. Rev. E*, 76:026221, Aug 2007.

[44] Nina C. Shapley, Robert C. Armstrong, and Robert A. Brown. Laser doppler velocimetry measurements of particle velocity fluctuations in a concentrated suspension. *J. Rheol.*, 46(1):241–272, 2002.

[45] Q. Shi, G. Sun, M. Hou, and K. Lu. Density-driven segregation in vertically vibrated binary granular mixtures. *Phys. Rev. E*, 75:061302, Jun 2007.

[46] Brian D. Timberlake and Jeffrey F. Morris. Concentration band dynamics in free-surface couette flow of a suspension. *Phys. Fluids*, 14(5):1580–1589, 2002.

[47] Mahesh Tirumkudulu, Antonio Mileo, and Andreas Acrivos. Particle segregation in monodisperse sheared suspensions in a partially filled rotating horizontal cylinder. *Phys. Fluids*, 12(6):1615–1618, 2000.

[48] Mahesh Tirumkudulu, Anubhav Tripathi, and Andreas Acrivos. Particle segregation in monodisperse sheared suspensions. *Phys. Fluids*, 11(3):507–509, 1999.

[49] H. G. Weller, G. Tabor, H. Jasak, and C. Fureby. A tensorial approach to computational continuum mechanics using object-oriented techniques. *Computers in Physics*, 12(6):620–631, 1998.

[50] Xin Yao, Marcos, and Teck Neng Wong. Slow viscous flow around two particles in a cylinder. *Microfluidics and Nanofluidics*, 21(10):161, Sep 2017.

[51] Adam Zrehen and Arun Ramachandran. Demonstration of secondary currents in the pressure-driven flow of a concentrated suspension through a square conduit. *Phys. Rev. Lett.*, 110:018306, Jan 2013.

APPENDIX

The solution of the creeping flow equations concerned with the flow past suspended particles in which the fluid is bounded by a cylindrical wall should be derived so as to find out the components of the velocity field in the (ρ, ϕ, z) cylindrical coordinate system. The coordinate system is depicted by the figure below.

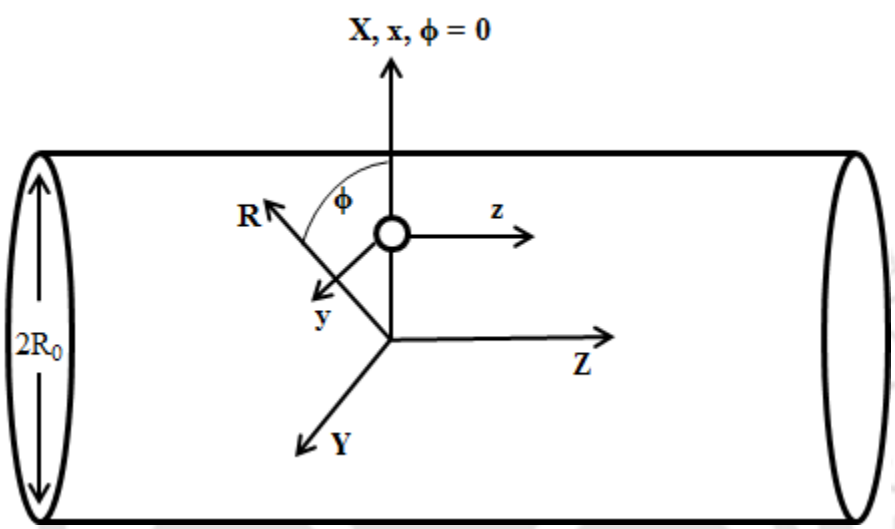

Figure: Coordinate system of a Stokeslet in a cylinder.

The following discussion provides details for the derivation of the components of the velocity from equation 2.16 in Chapter 2 of the thesis.

1. General Solution of Stokes Equation in Cylindrical Coordinates

Here, a detailed derivation is provided for the solution of creeping flow motion and the continuity equation for arbitrary boundary conditions on the surface of a long circular cylinder which is infinitely long.

Let the cylindrical coordinates be denoted by (ρ, ϕ, z), then the velocity vector is represented as

$$v = i_\rho v_\rho + i_\phi v_\phi + i_z v_z \tag{1.1}$$

The unit vectors in the direction of the three cylindrical coordinates described above are given by i_ρ, i_φ, i_z.The governing equations of the creeping flow motion in the three coordinates are

$$\nabla^2 v_z = \frac{1}{\mu}\frac{\partial p}{\partial z} \tag{1.2}$$

$$\nabla^2 v_\rho - \frac{v_\rho}{\rho^2} - \frac{2}{\rho^2}\frac{\partial v_\phi}{\partial \phi} = \frac{1}{\mu}\frac{\partial p}{\partial \rho} \tag{1.3}$$

$$\nabla^2 v_\phi - \frac{v_\phi}{\rho^2} + \frac{2}{\rho^2}\frac{\partial v_\rho}{\partial \phi} = \frac{1}{\mu}\frac{1}{\rho}\frac{\partial p}{\partial \rho} \tag{1.4}$$

The Laplacian is given by

$$\nabla^2 = \frac{\partial^2}{\partial \rho^2} + \frac{\partial}{\rho \partial \rho} + \frac{\partial^2}{\rho^2 \partial \phi} + \frac{\partial^2}{\partial z^2} \tag{1.5}$$

In addition to the above equations, we must also satisfy the continuity equation which is given by

$$\frac{v_\rho}{\partial \rho} + \frac{v_\rho}{\rho} + \frac{\partial v_\phi}{\rho \partial \phi} + \frac{\partial v_z}{\partial z} = 0 \tag{1.6}$$

Firstly, the particular solution to the above equations should be determined. Then the general solution of the homogeneous equations given by equations (1.7) and (1.8) is evaluated to be added to the particular solution.

$$\nabla^2 \dot{v} = 0 \tag{1.7}$$

$$\nabla . \dot{v} = 0 \tag{1.8}$$

1.1 Particular Solution of the Inhomogeneous Equations

It is to be noted here that the pressure field satisfies the Laplace equation. Solution of the Laplacian equation which satisfy any arbitrary boundary conditions on the surface $\rho = const.$ are expressed as:

$$\sum_{n=-\infty}^{\infty} \cos(n\phi)\int_0^{\infty} \eta(\lambda) I_n(\lambda\rho)\cos(\lambda z)d\lambda$$

or

$$\sum_{n=-\infty}^{\infty} \sin(n\phi)\int_0^{\infty} \eta(\lambda) K_n(\lambda\rho)\sin(\lambda z)d\lambda \qquad (1.9)$$

where $\eta(\lambda)$ is an arbitrary function being λ is an arbitrary parameter. This function can be evaluated from the boundary conditions. The functions $I_n(\lambda\rho)$ and $K_n(\lambda\rho)$ are modified Bessel functions of order n of the first and second kinds respectively.

$$I_n^{"}(\lambda\rho) + \frac{1}{\rho} I_n^{'}(\lambda\rho) - (\lambda^2 + \frac{n^2}{\rho^2}) I_n(\lambda\rho) = 0 \qquad (1.20)$$

with a similar expression for $K_n(\lambda\rho)$. The modified Bessel functions satisfy the differential equation (1.20). For the equations in this section, the differentiation is with respect to ρ. In order to find out an appropriate solution for the inhomogeneous equations, we shall first assume that the pressure field is very simple (a restriction which can be relaxed later).

We choose equation (1.21) as a particular solution,

$$p = \mu A_n(\lambda)\cos(n\phi) I_n(\lambda\rho)\sin(\lambda z) \qquad (1.21)$$

The z-component of the velocity is assumed have a solution of the form

$$v_z = F_n(\lambda, \rho)\cos(n\phi)\cos(\lambda z) \qquad (1.22)$$

Introduction of these functions into the equation (1.2)

$$\nabla^2 v_z = \frac{1}{\mu}\frac{\partial p}{\partial z}$$

$$\frac{1}{\mu}\frac{\partial p}{\partial z} = \frac{1}{\mu}.\mu A_n(\lambda)\cos(n\phi)I_n(\lambda\rho)\{\lambda\cos(\lambda z)\}$$

$$\nabla^2 v_z = \frac{\partial^2 v_z}{\partial \rho^2} + \frac{\partial v_z}{\rho\partial\rho} + \frac{\partial^2 v_z}{\rho^2\partial\phi} + \frac{\partial^2 v_z}{\partial z^2}$$

$$\frac{\partial^2 v_z}{\partial \rho^2} = -F_n(\lambda,\rho)\cos(n\phi)\{\lambda^2\cos(\lambda z)\}$$

$$\frac{\partial^2 v_z}{\rho^2\partial\phi} = \frac{1}{\rho^2}[F_n(\lambda,\rho)\{-n^2\cos(n\phi)\}\cos(\lambda z)]$$

$$\frac{\partial v_z}{\rho\partial\rho} = \frac{1}{\rho}F_n^{'}(\lambda,\rho)\cos(n\phi)\cos(\lambda z)$$

$$\frac{\partial^2 v_z}{\partial z^2} = F_n^{''}(\lambda,\rho)\cos(n\phi)\cos(\lambda z)$$

$$\Rightarrow [-F_n(\lambda,\rho)\lambda^2 - \frac{n^2}{\rho^2}F_n(\lambda,\rho) + \frac{1}{\rho}F_n^{'}(\lambda,\rho) + F_n^{''}(\lambda,\rho)]\cos(n\phi)\cos(\lambda z)$$

$$= A_n(\lambda)\lambda I_n(\lambda\rho)\cos(n\phi)\cos(\lambda z)$$

$$\Rightarrow F_n^{''} + \frac{1}{\rho}F_n^{'} - (\lambda^2 + \frac{n^2}{\rho^2})F_n = A_n(\lambda)\lambda I_n(\lambda\rho) \qquad (1.22)$$

As shown by the equation (1.20), the homogeneous part of the equation (1.22) is a Bessel's modified equation. Now, as we know the solution of the homogeneous equations, the method of variation of parameters could be used to influence the solution of inhomogeneous equation (1.22)

$$F_n(\lambda,\rho) = B_n(\lambda)I_n(\lambda,\rho) + A_n(\lambda)\frac{\rho I_n^{'}(\lambda\rho)}{2\lambda} \qquad (1.23)$$

where functions of the second kind are neglected in the solution. We therefore have

$$v_z = [B_n(\lambda)I_n(\lambda,\rho) + A_n(\lambda)\frac{\rho I_n^{'}(\lambda\rho)}{2\lambda}]\cos(n\phi)\cos(\lambda z) \qquad (1.24)$$

Arbitrariness in $B_n(\lambda)$ is removed by satisfying the continuity equation, where $B_n(\lambda)$ is articulated in terms of $A_n(\lambda)$.

For the velocity components v_ρ and v_φ the solutions are of the form

$$v_\rho = G_n(\lambda,\rho)\cos(n\phi)\sin(\lambda z) \tag{1.25}$$

$$v_\phi = H_n(\lambda,\rho)\sin(n\phi)\sin(\lambda z) \tag{1.26}$$

On following the same procedure as derived above, we have

$$G_n^{''} + \frac{1}{\rho}G_n^{'} - (\lambda^2 + \frac{n^2+1}{\rho^2})G_n - \frac{2n}{\rho^2}H_n = A_n(\lambda)I_n^{'}(\lambda\rho) \tag{1.27}$$

$$H_n^{''} + \frac{1}{\rho}H_n^{'} - (\lambda^2 + \frac{n^2+1}{\rho^2})H_n - \frac{2n}{\rho^2}G_n = -A_n(\lambda)I_n(\lambda\rho)\frac{n}{\rho} \tag{1.28}$$

Addition of equations (1.27) and (1.28) yields,

$$(G_n + H_n)^{''} + \frac{1}{\rho}(G_n + H_n)^{'} - [\lambda^2 + \frac{(n+1)^2}{\rho^2}](G_n + H_n) = A_n(\lambda)\lambda I_{n+1}(\lambda\rho) \tag{1.29}$$

The equation (1.29) is similar to that we obtained for F_n but with (n+1) written in place of n. A second expression can be obtained by subtraction.

$$(G_n - H_n)^{''} + \frac{1}{\rho}(G_n - H_n)^{'} - [\lambda^2 + \frac{(n-1)^2}{\rho^2}](G_n - H_n) = A_n(\lambda)\lambda I_{n-1}(\lambda\rho) \tag{1.30}$$

The above expression is similar to that we obtained for F_n but with *(n-1)* written in place of *n*. Recurrence relations given below are used in obtaining the above expressions

$$I_n^{'}(\lambda\rho) - \frac{n}{\rho}I_n(\lambda\rho) = \lambda I_{n+1}(\lambda\rho) \tag{1.31}$$

$$I_n^{'}(\lambda\rho) + \frac{n}{\rho}I_n(\lambda\rho) = \lambda I_{n-1}(\lambda\rho) \tag{1.32}$$

$\Rightarrow$

$$G_n(\lambda,\rho) = A_n(\lambda)\frac{\rho}{4\lambda}[I_{n+1}^{'}(\lambda\rho) + I_{n-1}^{'}(\lambda\rho)] \tag{1.33}$$

$$H_n(\lambda,\rho) = A_n(\lambda)\frac{\rho}{4\lambda}[I'_{n+1}(\lambda\rho) - I'_{n-1}(\lambda\rho)] \tag{1.34}$$

$C_n(\lambda)\,\&\,D_n(\lambda)$ have been set to zero. This is done because similar solutions of the homogeneous equations (1.7) and (1.8) occur later. Alternate expressions for $G_n\,\&\,H_n$ can be arrived at by the use of the differentiation of the recurrence formulae given below

$$I_{n+1}(X) + I_{n-1}(X) = 2I'_n(X)$$
$$I_{n+1}(X) - I_{n-1}(X) = -\frac{2nI_n(X)}{X}$$

Thus, we obtain

$$G_n(\lambda,\rho) = A_n(\lambda)\frac{I''_n(\lambda\rho)}{2\lambda^2} \tag{1.35}$$

$$H_n(\lambda,\rho) = A_n(\lambda)\frac{n}{2\lambda^2}[\frac{I_n(\lambda\rho)}{\rho} - I'_n(\lambda\rho)] \tag{1.36}$$

The expressions for the $\rho\,\&\,\phi$ components of the velocity field are, finally,

$$v_\rho = A_n(\lambda)\frac{I''_n(\lambda\rho)}{2\lambda^2}\rho\cos(n\phi)\sin(\lambda z) \tag{1.37}$$

$$v_\phi = A_n(\lambda)\frac{n}{2\lambda^2}[\frac{I_n(\lambda\rho)}{\rho} - I'_n(\lambda\rho)]\sin(n\phi)\sin(\lambda z) \tag{1.38}$$

These terms along with $v_z\,\&\,p$ constitute the solution of the equation initially considered. Now, the continuity equation shall be considered for further derivation

$$\frac{\partial v_\rho}{\partial\rho} + \frac{v_\rho}{\rho} + \frac{1}{\rho}\frac{\partial v_\phi}{\partial\phi} + \frac{\partial v_z}{\partial z}$$

$$\frac{\partial v_\rho}{\partial \rho} = \frac{A_n(\lambda)}{2\lambda^2}\cos(n\phi)\sin(\lambda z)[\rho I_n'''(\lambda\rho) + I_n''(\lambda\rho)]$$

$$\frac{v_\rho}{\rho} = A_n(\lambda)\frac{I_n''(\lambda\rho)}{2\lambda^2}\cos(n\phi)\sin(\lambda z)$$

$$\frac{1}{\rho}\frac{\partial v_\phi}{\partial \phi} = \frac{n^2 A_n(\lambda)}{2\rho\lambda^2}[\frac{I_n(\lambda\rho)}{\rho} - I_n'(\lambda\rho)]\cos(n\phi)\sin(\lambda z)$$

$$\frac{\partial v_z}{\partial z} = -[B_n(\lambda)I_n(\lambda\rho) + A_n(\lambda)\rho\frac{I_n'(\lambda\rho)}{2\lambda}]\cos(n\phi)\lambda\sin(\lambda z)$$

$$\Rightarrow \frac{A_n(\lambda)}{2\lambda^2}[\rho I_n'''(\lambda\rho) + 2I_n''(\lambda\rho) + \frac{n^2}{\rho^2}I_n(\lambda\rho) - \frac{n^2}{\rho}I_n(\lambda\rho) - \lambda^2\rho I_n'(\lambda\rho)] - B_n(\lambda)I_n(\lambda\rho)\lambda = 0$$

$$\Rightarrow I_n''(\lambda\rho) + \frac{1}{\rho}I_n'(\lambda\rho) - (\lambda^2 + \frac{n^2}{\rho^2})I_n(\lambda\rho) = 0 \qquad (1.39)$$

Multiplying and differentiating with respect to ρ we get,

$$\frac{\partial}{\partial \rho}[\rho I_n''(\lambda\rho) + I_n'(\lambda\rho) - \rho(\lambda^2 + \frac{n^2}{\rho^2})I_n(\lambda\rho)] = 0$$

$$\Rightarrow \rho I_n'''(\lambda\rho) + 2I_n''(\lambda\rho) - (\lambda^2 + \frac{n^2}{\rho^2})I_n'(\lambda\rho) - (\lambda^2 - \frac{n^2}{\rho^2})I_n(\lambda\rho) \qquad (1.40)$$

Comparing the above equation to the continuity equation we have,

$$B_n(\lambda) = \frac{A_n(\lambda)}{2\lambda^2}$$

$$\Rightarrow v_z = \frac{A_n(\lambda)}{2\lambda^2}[I_n(\lambda\rho) + \lambda\rho I_n'(\lambda\rho)]\cos(n\phi)\cos(\lambda z) \qquad (1.41)$$

If we now define a harmonic function Π by the relation,

$$\Pi = \frac{A_n(\lambda)}{2\lambda^2}I_n(\lambda\rho)\cos(n\phi)\sin(\lambda z) \qquad (1.42)$$

Now, using the above derived relations it can be evidenced that,

$$v_\rho = \rho\frac{\partial}{\partial \rho}(\frac{\partial \Pi}{\partial \rho}) \qquad (1.43)$$

$$v_\phi = \rho \frac{\partial}{\partial \rho}\left(\frac{1}{\rho}\frac{\partial \Pi}{\partial \phi}\right) \tag{1.44}$$

$$v_z = \rho \frac{\partial}{\partial \rho}\left(\frac{\partial \Pi}{\partial z}\right) + \frac{\partial \Pi}{\partial z} \tag{1.45}$$

$$p = -2\mu \frac{\partial^2 \Pi}{\partial z^2} \tag{1.46}$$

In vector notation,

$$v = \rho \frac{\partial}{\partial \rho}(\nabla \Pi) + i_z \frac{\partial \Pi}{\partial z} \tag{1.47}$$

The pressure and the velocity fields presented in equations (1.43-1.47) is a simultaneous solution of the creeping flow equations and the continuity equation for any harmonic function Π which is arbitrary.

$$\nabla^2 \Pi = 0 \tag{1.48}$$

1.2 Solution of the Homogeneous Equations

The solution of the homogeneous equations (1.7) and (1.8) is derived below. As earlier, the solutions assume the form,

$$v_z' = f_n(\lambda, \rho)\cos(n\varphi)\cos(\lambda z) \tag{1.49}$$

$$v_\rho' = g_n(\lambda, \rho)\cos(n\varphi)\sin(\lambda z) \tag{1.50}$$

$$v_\phi' = h_n(\lambda, \rho)\sin(n\varphi)\sin(\lambda z) \tag{1.51}$$

These equations are identical in to those used in the derivation of the corresponding particular solution (inhomogeneous case). Now, if $A_n(\lambda) = 0$ we can infer that the equations $\nabla^2 v' = 0$ are solved by choosing

$$f_n(\lambda,\rho) = b_n(\lambda) I_n(\lambda\rho) \tag{1.52}$$

$$g_n(\lambda,\rho) + h_n(\lambda,\rho) = c_n(\lambda,\rho) I_{n+1}(\lambda\rho) \tag{1.53}$$

$$g_n(\lambda,\rho) - h_n(\lambda,\rho) = d_n(\lambda,\rho) I_{n-1}(\lambda\rho) \tag{1.54}$$

On solving the equations (1.52-1.54) simultaneously we can obtain g_n & f_n. Once this is done, and if functions $e_n(\lambda)$ & $f_n(\lambda)$ are defined as,

$$e_n(\lambda) = \frac{c_n(\lambda,\rho) + d_n(\lambda,\rho)}{2\lambda} \tag{1.55}$$

$$f_n(\lambda) = \frac{c_n(\lambda,\rho) - d_n(\lambda,\rho)}{2\lambda} \tag{1.56}$$

then, with the usage of the aforementioned recurrence relations, we obtain

$$v_\rho^{'} = [e_n(\lambda) I_n^{'}(\lambda\rho) - \frac{n}{\rho} f_n(\lambda) I_n(\lambda\rho)] \cos(n\varphi) \sin(\lambda z) \tag{1.57}$$

$$v_\phi^{'} = [f_n(\lambda) I_n^{'}(\lambda\rho) - \frac{n}{\rho} e_n(\lambda) I_n(\lambda\rho)] \sin(n\varphi) \sin(\lambda z) \tag{1.58}$$

$$v_z^{'} = b_n(\lambda,\rho) I_n(\lambda\rho) \cos(n\varphi) \cos(\lambda z) \tag{1.59}$$

If we now introduce these results into the continuity equation given by equation (1.8), we find that

$$e_n(\lambda)[I_n^{''}(\lambda\rho) + \frac{1}{\rho} I_n^{'}(\lambda\rho) - \frac{n^2}{\rho^2} I_n^{'}(\lambda\rho)] - b_n(\lambda,\rho)\lambda I_n(\lambda\rho) = 0 \tag{1.60}$$

the coefficient of $f_n(\lambda)$ being zero. In order to satisfy the continuity equation we choose

$$v_z^{'} = \lambda e_n(\lambda) I_n(\lambda\rho) \cos(n\varphi) \cos(\lambda z) \tag{1.61}$$

Now, we define the functions

$$\Psi = e_n(\lambda) I_n(\lambda\rho) \cos(n\varphi) \sin(\lambda z) \tag{1.62}$$

$$\Omega = -f_n(\lambda) I_n(\lambda\rho)\sin(n\varphi)\sin(\lambda z) \tag{1.63}$$

The component velocities of $\dot{v}$ are of the form

$$v_\rho' = \frac{\partial \Psi}{\partial \rho} + \frac{\partial \Omega}{\rho \partial \phi} \tag{1.64}$$

$$v_\phi' = \frac{\partial \Psi}{\rho \partial \phi} - \frac{\partial \Omega}{\partial \rho} \tag{1.65}$$

$$v_z' = \frac{\partial \Psi}{\partial z} \tag{1.66}$$

A concise form of the velocity field in the vector notation can be written as,

$$v' = \nabla\Psi + \nabla \times (i_z \Omega) \tag{1.67}$$

Here too the result holds true for any harmonic functions,

$$\nabla^2 \Psi = 0 \tag{1.68}$$

$$\nabla^2 \Omega = 0 \tag{1.69}$$

1.2.1 Solution of Boundary Value Problems Involving Circular Cylinders

We can now obtain a solution for the continuity and the creeping flow equations on addition of the solutions of the homogeneous and inhomogeneous equations. Therefore,

$$v = \nabla\Psi + \nabla \times (i_z \Omega) + \rho \frac{\partial}{\partial \rho}(\nabla \Pi) + i_z \frac{\partial \Pi}{\partial z} \tag{1.70}$$

$$p = -2\mu \frac{\partial^2 \Pi}{\partial z^2} \tag{1.71}$$

provided

$$\nabla^2 \{\Pi, \Psi, \Omega\} = \{0, 0, 0\} \tag{1.72}$$

Our concern now is to show how to apply these results to the solution of boundary value problems involving circular cylindrical surfaces. In the derivation that follows, it is assumed that the fluid domain is confined to the interior of an infinitely long circular cylinder. The velocity field assumes arbitrarily prescribed values on the surface of the cylinder. We also assume that the harmonic functions Π, Ψ, Ω can be expressed as,

$$\{\Pi, \Psi, \Omega\} = \sum_{n=-\infty}^{\infty} \{\Pi_n, \Psi_n, \Omega_n\} \tag{1.73}$$

where $\nabla^2\{\Pi_n, \Psi_n, \Omega_n\} = 0$

The method of solution consists in the determination of $\{\Pi, \Psi, \Omega\}$ for each *n*. Solutions of Laplace's equation are of the form

$$\{\Pi_n, \Psi_n, \Omega_n\} = \cos(n\phi + \{\alpha_n, \beta_n, \gamma_n\}) \times \int_0^{\infty} \{\pi_n(\lambda), \psi_n(\lambda), \omega_n(\lambda)\} I_n(\lambda\rho) \cos(\lambda z + \{\delta_\lambda, \xi_\lambda, \zeta_\lambda\}) d\lambda \tag{1.74}$$

Thus, it is necessary to establish the form taken by these functions on application of appropriate boundary conditions, after which the problem is evaluated. This is done by introducing the equation (1.74) into the equation (1.70), the resulting expressions for the component velocities on the cylinder wall are given by

$$[v_\rho]_{\rho=\rho_0} = \sum_{n=-\infty}^{\infty} \cos(n\phi + \sigma_n) \int_0^{\infty} \xi_n(\lambda) \cos(\lambda z + v_\lambda) d\lambda \tag{1.75}$$

with corresponding expressions for other components of the velocity at the cylinder wall. Where,

$$\sigma_n = function(\alpha_n, \beta_n, \gamma_n) \tag{1.76}$$

$$\xi_n(\lambda) = function[\pi_n(\lambda), \psi_n(\lambda), \omega_n(\lambda)] \tag{1.77}$$

$$v_\lambda = function(\delta_\lambda, \xi_\lambda, \zeta_\lambda) \tag{1.78}$$

1.3 Formulation

Our main objective in this case is to find the fundamental singular solutions (velocity and pressure) for the spherical particle situated in the cylinder as described in the general solution case satisfying no-slip boundary conditions on the cylinder wall. Three different sets of solutions exist corresponding to three independent directions of the particle and the directions (x, y, z) were chosen which also correspond to the directions (R, Φ, Z) at the particle. The three different sets of solutions for the pressure and velocity in the (x, y, z) system shall be denoted by

$$P^k, u^k = (u_j^k) \,\&\, j, k = (1, 2, 3) \tag{1.79}$$

where $k = (1, 2, 3)$ corresponds to a point sized particle in the (x, y, z) directions, respectively, and $j = (1, 2, 3)$ corresponds to the components of velocity in the (x, y, z) directions, respectively. On the other hand, if we need the velocities in the (R, Φ, Z) directions, we use the notation (u_R^k, u_Φ^k, u_Z^k) . Whereas, the functions P^k & u^k are the solutions of the Stokes equations with the boundary conditions,

$$u^k = 0 \text{ at } R = R_0 \tag{1.80}$$

$$u^k \rightarrow 0 \text{ as } Z = \pm\infty \tag{1.81}$$

Let us for a moment consider only the contribution from the Stokeslet to the velocity field, i.e. a point force is considered in place of a finite-sized particle. The total velocity field is then represented as

$$u_i = \frac{-3a}{4} U_j^\infty \left(\frac{\delta_{ij}}{r} + \frac{x_i x_j}{r^3}\right) \tag{1.82}$$

In terms of the force from Stokes law, the velocity field is expressed by Oseen-Burger tensor (which is a singularity) given by

$$v_j^k = \frac{1}{8\pi\mu} \left(\frac{\delta_{ij}}{r} + \frac{x_i x_j}{r^3}\right) \tag{1.83}$$

Here emphasis is given to the Oseen-Burger tensor because the idea is to express the full form of the velocity from the Stokes equation in terms of singularities which are higher order derivatives of the Oseen-Burger tensor. Thence the velocity in terms of singularities is

$$\frac{-3a}{4}U_j^{\infty}\left(\frac{\delta_{ij}}{r}+\frac{x_i x_j}{r^3}\right)-\frac{-3a^3}{4}\left(\frac{\delta_{ij}}{r^3}-\frac{3x_i x_j}{r^5}\right) \quad \text{(translation)} \quad (1.84)$$

$$\frac{1}{2}(G_{ij,k}-G_{ik,j})=\frac{1}{r^3}(\delta_{ik}x_j-\delta_{ij}x_k) \quad \text{(rotation)} \quad (1.85)$$

$$\left(1+\frac{a^2}{10}\nabla^2\right)(G_{ij,k}+G_{ik,j})=\frac{-6}{5r^3}(\delta_{ik}x_j+\delta_{ij}x_k-\frac{2}{3}\delta_{jk}x_i) \quad \text{(rate of strain)} \quad (1.86)$$

Finally, the pressure is given by

$$P_1^k=\frac{1}{4\pi}\frac{x_k}{r^3} \quad (1.87)$$

We are now left to solve for the correction due to the presence of the cylinder wall in the flow. Therefore, it is sufficient to solve for the equations

$$\nabla p^k=\mu\nabla^2 g^k \quad (1.88)$$

$$\nabla . g^k=0 \quad (1.89)$$

with the boundary conditions,

$$g^k(R=R_0)=-v^k(R=R_0) \quad (1.90)$$

$$g^k\to 0, Z\to\pm\infty \quad (1.91)$$

Then the complete solution is given by,

$$u^k=v^k+g^k \quad (1.92)$$

$$P^k=P_1^k+p^k \quad (1.93)$$

1.4 Transformation of Singular Solution

In order to use the general solution for the Stokes equations obtained earlier, we need to transform the velocity and the pressure obtained in the preceding section to cylindrical coordinates. This formulation is discussed below.

In terms of preferred coordinates,

$$i_z = i_z \tag{1.94}$$

$$\nabla = i_R \frac{\partial}{\partial R} + i_\Phi \frac{\partial}{\partial \Phi} + i_z \frac{\partial}{\partial Z}$$

Now, our primary objective is the transformation of functions $1/r \,\&\, z/r$ into these coordinates.

$1/r \,\&\, z/r$ are expressed as

$$\frac{1}{r} = (\rho^2 + z^2)^{-1/2} = \frac{2}{\pi}\int_0^\infty K_0(\lambda\rho)\cos(\lambda z)d\lambda \tag{1.95}$$

where K_0 is the modified Bessel function of the second kind of order zero. Noting that,

$$\rho = (R^2 + b^2 - 2bR\cos\Phi)^{1/2} \tag{1.96}$$

Further transformation yields,

$$K_0(\lambda\rho) = \sum_{k=-\infty}^{\infty} K_k(\lambda R) I_k(\lambda b)\cos(k\Phi) \tag{1.97}$$

Here $K_k(\lambda R) \,\&\, I_k(\lambda b)$ are modified Bessel functions of the first and second kinds, being valid for only $R > b$. These expressions add up to

$$\frac{1}{r} = \frac{2}{\pi}\sum_{k=-\infty}^{\infty} \cos(k\Phi)\int_0^\infty K_k(\lambda R) I_k(\lambda b)\cos(\lambda z)d\lambda \tag{1.98}$$

For the second transformation the following identity is valid :

$$ZK_k(\lambda R) I_k(\lambda b)\cos(\lambda z) - \frac{\partial}{\partial\lambda}[K_k(\lambda R) I_k(\lambda b)\sin(\lambda z)] - \sin(\lambda z)\frac{\partial}{\partial\lambda}[K_k(\lambda R) I_k(\lambda b)] \tag{1.99}$$

Thus, if equation (1.95) is multiplied by z, we obtain,

$$\frac{z}{r} = \frac{2}{\pi}\sum_{k=-\infty}^{\infty} \cos(k\Phi)[K_k(\lambda R) I_k(\lambda b)\sin(\lambda z)]_{\lambda=0}^{\lambda=\infty} - \frac{2}{\pi}\sum_{k=-\infty}^{\infty} \cos(k\Phi)\int_0^\infty \frac{\partial}{\partial\lambda}[K_k(\lambda R) I_k(\lambda b)]\sin(\lambda z)d\lambda \tag{1.100}$$

The first term becomes zero at the upper and lower limits, $\lambda = 0 \& \infty$. By differentiating the second expression we have,

$$\frac{z}{r} = -\frac{2}{\pi}\sum_{k=-\infty}^{\infty}\cos(k\Phi)\int_0^{\infty}[RK_k^{'}(\lambda R)I_k(\lambda b) + bK_k(\lambda R)I_k^{'}(\lambda b)]\sin(\lambda z)d\lambda \tag{1.101}$$

Using the relations such as

$$\frac{xz}{r^3} = -\frac{\partial}{\partial x}(\frac{z}{r}), \frac{yz}{r^3} = -\frac{\partial}{\partial y}(\frac{z}{r}), \frac{1}{r} + \frac{z^2}{r^3} = \frac{2}{r} - \frac{\partial}{\partial z}(\frac{z}{r}) \tag{1.102}$$

$$\frac{x}{r} = \int \frac{\partial}{\partial x}(\frac{z}{r})dz, \frac{y}{r} = \int \frac{\partial}{\partial y}(\frac{z}{r})dz \tag{1.103}$$

we can easily deduce that

$$\frac{x}{r} = -\frac{2}{\pi}\sum_{k=-\infty}^{\infty}(\cos\phi\cos k\phi)\int_0^{\infty}[K_k^{'}I_k + \lambda bK_k^{'}I_k^{'} + \lambda RK_k^{''}I_k]\frac{\cos(\lambda z)}{-\lambda}d\lambda$$

$$+\frac{2}{\pi}\sum_{k=-\infty}^{\infty}(\sin\phi\sin k\phi)\int_0^{\infty}\frac{k}{R}[RK_k^{'}I_k + bK_kI_k^{'}]\frac{\cos(\lambda z)}{-\lambda}d\lambda \tag{1.104}$$

$$\frac{y}{r} = -\frac{2}{\pi}\sum_{k=-\infty}^{\infty}(\cos\phi\sin k\phi)\int_0^{\infty}[RK_k^{'}I_k + bK_kI_k^{'}]\frac{\cos(\lambda z)}{-\lambda}d\lambda$$

$$+\frac{2}{\pi}\sum_{k=-\infty}^{\infty}(\sin\phi\cos k\phi)\int_0^{\infty}\frac{k}{R}[K_k^{'}I_k + \lambda bK_k^{'}I_k^{'} + \lambda RK_k^{''}I_k]\frac{\cos(\lambda z)}{-\lambda}d\lambda \tag{1.105}$$

It is to be noted that

$$X^2 + Y^2 = R^2, X = R\cos\Phi, Y = R\sin\Phi, x = X - b$$

which leads to the relations,

$$\frac{\partial}{\partial x} = \cos\phi\frac{\partial}{\partial R} - \frac{\sin\phi}{R}\frac{\partial}{\partial\phi}, \frac{\partial}{\partial y} = \sin\phi\frac{\partial}{\partial R} + \frac{\cos\phi}{R}\frac{\partial}{\partial\phi} \tag{1.106}$$

After some algebraic operations, we obtain the expressions for the velocities:

$$4\pi^2\mu v_j^k = \sum_{k=-\infty}^{\infty} \cos(k\Phi)\int_0^{\infty} f_j^j(\lambda,R,k,b)\cos(\lambda z)d\lambda,\ j=(1,2,3)$$

$$4\pi^2\mu v_2^1 = 4\pi^2\mu v_1^2 = \sum_{k=-\infty}^{\infty} \sin(k\Phi)\int_0^{\infty} f_2^1(\lambda,R,k,b)\cos(\lambda z)d\lambda,$$

$$4\pi^2\mu v_3^1 = 4\pi^2\mu v_1^3 = \sum_{k=-\infty}^{\infty} \cos(k\Phi)\int_0^{\infty} f_3^1(\lambda,R,k,b)\sin(\lambda z)d\lambda,$$

$$4\pi^2\mu v_3^2 = 4\pi^2\mu v_2^3 = \sum_{k=-\infty}^{\infty} \sin(k\Phi)\int_0^{\infty} f_3^2(\lambda,R,k,b)\sin(\lambda z)d\lambda, \qquad (1.107)$$

and for the pressure

$$2\pi^2 P_1^1 = \sum_{k=-\infty}^{\infty} \cos(k\Phi)\int_0^{\infty} t^1(\lambda,R,k,b)\cos(\lambda z)d\lambda,$$

$$2\pi^2 P_1^2 = \sum_{k=-\infty}^{\infty} \sin(k\Phi)\int_0^{\infty} t^2(\lambda,R,k,b)\cos(\lambda z)d\lambda,$$

$$2\pi^2 P_1^3 = \sum_{k=-\infty}^{\infty} \sin(k\Phi)\int_0^{\infty} t^3(\lambda,R,k,b)\sin(\lambda z)d\lambda, \qquad (1.108)$$

where the functions f_j^k, t^k are in terms of Fourier-Bessel coefficients. These functions contain the contribution from the translation, rotation and the rate of strain components of the velocity. Contribution from the translation motion is a second order tensor while those from the remaining two components are third order tensors. Essentially, the auxiliary solution for the velocity field from the general solution for Stokes flow is also a second order tensor. In order to evaluate the unknowns, consistency in dimensions is to be maintained. Contribution from each individual component of the velocity and the necessary steps to be required to compare the transformed solution with the auxiliary solution are discussed below.

Let us first consider the translational velocity component,

$$v_j^k = \frac{1}{8\pi\mu}\left(\frac{\delta_{ij}}{r} + \frac{x_i x_j}{r^3}\right) + \frac{1}{8\pi\mu}\left(\frac{\delta_{ij}}{r^3} - \frac{3x_i x_j}{r^5}\right) \qquad (1.109)$$

From the above expression it is obvious that the terms

$$(\frac{\delta_{ij}}{r}+\frac{x_i x_j}{r^3}),(\frac{\delta_{ij}}{r^3}-\frac{3x_i x_j}{r^5}) \tag{1.110}$$

describe the translation motion. Evaluation of these terms would be the sufficient requisite in this case. Out of the nine components from the second order tensors only six components are independent which are,

$$\begin{aligned}
v^{11} &= (\frac{1}{r}+\frac{x^2}{r^3})+(\frac{1}{r^3}-\frac{3x^2}{r^5}) \\
v^{22} &= (\frac{1}{r}+\frac{y^2}{r^3})+(\frac{1}{r^3}-\frac{3y^2}{r^5}) \\
v^{33} &= (\frac{1}{r}+\frac{z^2}{r^3})+(\frac{1}{r^3}-\frac{3z^2}{r^5}) \\
v^{12} &= v^{21} = \frac{xy}{r^3}-\frac{3xy}{r^5} \\
v^{13} &= v^{31} = \frac{xy}{r^3}-\frac{3xy}{r^5} \\
v^{23} &= v^{32} = \frac{yz}{r^3}-\frac{3yz}{r^5}
\end{aligned} \tag{1.111}$$

These expressions are easily evaluated as shown below,

$$\begin{aligned}
v^{11} &= \frac{2}{r}-\frac{\partial}{\partial x}(\frac{x}{r})-\frac{\partial^2}{\partial x^2}(\frac{x}{r}) \\
v^{22} &= \frac{2}{r}-\frac{\partial}{\partial y}(\frac{y}{r})-\frac{\partial^2}{\partial y^2}(\frac{y}{r}) \\
v^{33} &= \frac{2}{r}-\frac{\partial}{\partial z}(\frac{z}{r})-\frac{\partial^2}{\partial z^2}(\frac{z}{r}) \\
v^{12} &= v^{21} = -\frac{\partial}{\partial x}(\frac{y}{r})+\frac{\partial}{\partial y}\{\frac{\partial}{\partial x}(\frac{1}{r})\} \\
v^{13} &= v^{31} = -\frac{\partial}{\partial x}(\frac{z}{r})+\frac{\partial}{\partial z}\{\frac{\partial}{\partial x}(\frac{1}{r})\} \\
v^{23} &= v^{32} = -\frac{\partial}{\partial z}(\frac{y}{r})+\frac{\partial}{\partial z}\{\frac{\partial}{\partial y}(\frac{1}{r})\}
\end{aligned} \tag{1.112}$$

For the rotation component of the velocity, we have,

$$\frac{1}{2}(G_{ij,k}-G_{ik,j})=\frac{1}{r^3}(\delta_{ik}x_j-\delta_{ij}x_k) \tag{1.113}$$

Since the above expression is a third order tensor, dot product with the normal gives consistency in dimensions. The combinations of terms which add up to produce a second order tensor are

$$\begin{pmatrix} (1,1,1)+(2,1,1)+(3,1,1) & (1,1,2)+(2,1,2)+(3,1,2) & (1,1,3)+(2,1,3)+(3,1,3) \\ (1,2,1)+(2,2,1)+(3,2,1) & (1,2,2)+(2,2,2)+(3,2,2) & (1,2,3)+(2,2,3)+(3,2,3) \\ (1,3,1)+(2,3,1)+(3,3,1) & (1,3,2)+(2,3,2)+(3,3,2) & (1,3,3)+(2,3,3)+(3,3,3) \end{pmatrix}$$

Here (i, j, k) are elements of the third order tensor. Therefore, the elements simplify to

$$\begin{pmatrix} 0 & \frac{x}{r^3}-\frac{y}{r^3} & \frac{x}{r^3}-\frac{z}{r^3} \\ \frac{y}{r^3}-\frac{x}{r^3} & 0 & \frac{y}{r^3}-\frac{z}{r^3} \\ \frac{z}{r^3}-\frac{x}{r^3} & \frac{z}{r^3}-\frac{y}{r^3} & 0 \end{pmatrix}$$

$$\Rightarrow v^{12} = -v^{21} = \frac{x}{r^3}-\frac{y}{r^3}$$
$$v^{13} = -v^{31} = \frac{x}{r^3}-\frac{z}{r^3}$$
$$v^{23} = -v^{32} = \frac{y}{r^3}-\frac{z}{r^3} \qquad (1.115)$$

Rotational component is fully evaluated using the relations,

$$v^{12} = -v^{21} = -\frac{\partial}{\partial x}(\frac{1}{r}) + \frac{\partial}{\partial y}(\frac{1}{r})$$
$$v^{13} = -v^{31} = -\frac{\partial}{\partial x}(\frac{1}{r}) + \frac{\partial}{\partial z}(\frac{1}{r})$$
$$v^{23} = -v^{32} = -\frac{\partial}{\partial y}(\frac{1}{r}) + \frac{\partial}{\partial z}(\frac{1}{r}) \qquad (1.116)$$

Finally, for the rate of strain component,

$$(1+\frac{a^2}{10}\nabla^2)(G_{ij,k}+G_{ik,j}) = \frac{-6}{5r^3}(\delta_{ik}x_j + \delta_{ij}x_k - \frac{2}{3}\delta_{jk}x_i) \qquad (1.117)$$

Since this too is a third order tensor, the same procedure as the rotational velocity is followed. The elements simplify to,

$$\begin{pmatrix} \frac{4}{5}(-2\frac{x}{r^3}+\frac{y}{r^3}+\frac{z}{r^3}) & \frac{-6}{5}(\frac{x}{r^3}+\frac{y}{r^3}) & \frac{-6}{5}(\frac{x}{r^3}+\frac{z}{r^3}) \\ \frac{-6}{5}(\frac{x}{r^3}+\frac{y}{r^3}) & \frac{4}{5}(-2\frac{y}{r^3}+\frac{x}{r^3}+\frac{z}{r^3}) & \frac{-6}{5}(\frac{y}{r^3}+\frac{z}{r^3}) \\ \frac{-6}{5}(\frac{x}{r^3}+\frac{z}{r^3}) & \frac{-6}{5}(\frac{y}{r^3}+\frac{z}{r^3}) & \frac{4}{5}(-2\frac{z}{r^3}+\frac{x}{r^3}+\frac{y}{r^3}) \end{pmatrix} \tag{1.118}$$

$$\Rightarrow v^{11} = \frac{4}{5}\{2\frac{\partial}{\partial x}(\frac{1}{r}) - \frac{\partial}{\partial y}(\frac{1}{r}) - \frac{\partial}{\partial z}(\frac{1}{r})\}$$

$$v^{22} = \frac{4}{5}\{2\frac{\partial}{\partial y}(\frac{1}{r}) - \frac{\partial}{\partial x}(\frac{1}{r}) - \frac{\partial}{\partial z}(\frac{1}{r})\}$$

$$v^{33} = \frac{4}{5}\{2\frac{\partial}{\partial z}(\frac{1}{r}) - \frac{\partial}{\partial y}(\frac{1}{r}) - \frac{\partial}{\partial x}(\frac{1}{r})\}$$

$$v^{12} = v^{21} = \frac{6}{5}\{\frac{\partial}{\partial x}(\frac{1}{r}) + \frac{\partial}{\partial y}(\frac{1}{r})\}$$

$$v^{13} = v^{31} = \frac{6}{5}\{\frac{\partial}{\partial x}(\frac{1}{r}) + \frac{\partial}{\partial z}(\frac{1}{r})\}$$

$$v^{23} = v^{32} = \frac{6}{5}\{\frac{\partial}{\partial y}(\frac{1}{r}) + \frac{\partial}{\partial z}(\frac{1}{r})\} \tag{1.119}$$

Now, since we have all the elements of tensors for translational, rotational and rate of strain components, simple addition of these matrices gives us the exact contribution of the complete velocity field. For instance,

$$v^{11} = \frac{2}{r} - \frac{\partial}{\partial x}(\frac{x}{r}) - \frac{\partial^2}{\partial x^2}(\frac{x}{r}) + \frac{4}{5}\{2\frac{\partial}{\partial x}(\frac{1}{r}) - \frac{\partial}{\partial y}(\frac{1}{r}) - \frac{\partial}{\partial z}(\frac{1}{r})\} \tag{1.120}$$

These terms which are functions of Fourier coefficients can now be compared to the auxiliary solution which already is in terms of Fourier functions.

1.5 Auxiliary solution

From the solution of the boundary value problems involving circular cylinders, we can write

$$\Pi_k = \sum_{k=-\infty}^{\infty} \cos(k\Phi + \alpha_k^1) \int_0^{\infty} \pi_k(\lambda) I_k(\lambda\rho) \cos(\lambda z + \delta_\lambda^1) d\lambda$$

$$\Psi_k = \sum_{k=-\infty}^{\infty} \cos(k\Phi + \alpha_k^2) \int_0^{\infty} \psi_k(\lambda) I_k(\lambda\rho) \cos(\lambda z + \delta_\lambda^2) d\lambda$$

$$\Omega_k = \sum_{k=-\infty}^{\infty} \cos(k\Phi + \alpha_k^3) \int_0^{\infty} \omega_k(\lambda) I_k(\lambda\rho) \cos(\lambda z + \delta_\lambda^3) d\lambda \qquad (1.121)$$

For the velocity components, the contributions from the particular and homogeneous solutions are considered separately and then summed up. The derivation is given below

$$v_\rho = \rho \frac{\partial}{\partial \rho}\left(\frac{\partial \Pi}{\partial \rho}\right), v_\phi = \rho \frac{\partial}{\partial \rho}\left(\frac{\partial \Pi}{\rho \partial \phi}\right), v_z = \rho \frac{\partial}{\partial \rho}\left(\frac{\partial \Pi}{\partial z}\right) + \frac{\partial \Pi}{\partial z}$$

$$v_\rho' = \frac{\partial \Psi}{\partial \rho} + \frac{\partial \Omega}{\rho \partial \phi}, v_\phi' = \frac{\partial \Psi}{\rho \partial \phi} - \frac{\partial \Omega}{\partial \rho}, v_z' = \frac{\partial \Psi}{\partial z}$$

$$g_R = v_\rho + v_\rho', g_\phi = v_\phi + v_\phi', g_z = v_z + v_z' \qquad (1.122)$$

From the above relations, we get

$$\frac{\partial \Pi}{\partial \rho} = \sum_{k=-\infty}^{\infty} \cos(k\Phi + \alpha_k^1) \int_0^{\infty} \pi_k(\lambda) \lambda I_\lambda'(\lambda\rho) \cos(\lambda z + \delta_\lambda^1) d\lambda \qquad (1.123)$$

$$\rho \frac{\partial}{\partial \rho}\left(\frac{\partial \Pi}{\partial \rho}\right) = \sum_{k=-\infty}^{\infty} \cos(k\Phi + \alpha_k^1) \int_0^{\infty} \pi_k(\lambda) \lambda^2 \rho I_\lambda''(\lambda\rho) \cos(\lambda z + \delta_\lambda^1) d\lambda \qquad (1.124)$$

$$\frac{\partial \Psi}{\partial \rho} = \sum_{k=-\infty}^{\infty} \cos(k\Phi + \alpha_k^2) \int_0^{\infty} \psi_k(\lambda) \lambda I_k'(\lambda\rho) \cos(\lambda z + \delta_\lambda^2) d\lambda \qquad (1.125)$$

$$\frac{\partial \Omega}{\rho \partial \phi} = \sum_{k=-\infty}^{\infty} \sin(k\Phi + \alpha_k^3) \int_0^{\infty} \omega_k(\lambda) \left(-\frac{k}{\rho}\right) I_k(\lambda\rho) \cos(\lambda z + \delta_\lambda^3) d\lambda \qquad (1.126)$$

$$\Rightarrow g_R = \sum_{k=-\infty}^{\infty} \cos(k\Phi + \alpha_k^1) \int_0^{\infty} \pi_k(\lambda)(\lambda^2 \rho) I_\lambda''(\lambda\rho) \cos(\lambda z + \delta_\lambda^1) d\lambda$$

$$+ \sum_{k=-\infty}^{\infty} \cos(k\Phi + \alpha_k^2) \int_0^{\infty} \psi_k(\lambda) \lambda I_k'(\lambda\rho) \cos(\lambda z + \delta_\lambda^2) d\lambda$$

$$+\sum_{k=-\infty}^{\infty}\sin(k\Phi+\alpha_k^3)\int_0^{\infty}\omega_k(\lambda)(-\frac{k}{\rho})I_k(\lambda\rho)\cos(\lambda z+\delta_\lambda^3)d\lambda \tag{1.127}$$

Now, for the second component of the velocity,

$$\frac{\partial\Psi}{\rho\partial\phi}=\frac{1}{\rho}\sum_{k=-\infty}^{\infty}(-k)\sin(k\Phi+\alpha_k^2)\int_0^{\infty}\psi_k(\lambda)I_k(\lambda\rho)\cos(\lambda z+\delta_\lambda^2)d\lambda \tag{1.128}$$

$$\frac{\partial\Omega}{\partial\rho}=\sum_{k=-\infty}^{\infty}\cos(k\Phi+\alpha_k^3)\int_0^{\infty}\lambda\omega_k(\lambda)I_\lambda^{'}(\lambda\rho)\cos(\lambda z+\delta_\lambda^3)d\lambda \tag{1.129}$$

$$\frac{\partial\Pi}{\rho\partial\phi}=\frac{1}{\rho}\sum_{k=-\infty}^{\infty}(-k)\sin(k\Phi+\alpha_k^1)\int_0^{\infty}\pi_k(\lambda)I_k(\lambda\rho)\cos(\lambda z+\delta_\lambda^1)d\lambda \tag{1.130}$$

$$\frac{\partial}{\partial\rho}(\frac{\partial\Pi}{\rho\partial\phi})=\frac{1}{\rho}\frac{\partial}{\partial\rho}(\frac{\partial\Pi}{\partial\phi})-\frac{1}{\rho^2}\frac{\partial\Pi}{\partial\phi} \tag{1.132}$$

$$\rho\frac{\partial}{\partial\rho}(\frac{\partial\Pi}{\rho\partial\phi})=\rho[\frac{1}{\rho}\frac{\partial}{\partial\rho}(\frac{\partial\Pi}{\partial\phi})-\frac{1}{\rho^2}\frac{\partial\Pi}{\partial\phi}]$$

$$=\sum_{k=-\infty}^{\infty}\sin(k\Phi+\alpha_k^1)\int_0^{\infty}\pi_k(\lambda)\{\frac{k}{\rho}I_k(\lambda\rho)-k\lambda I_\lambda^{'}(\lambda\rho)\}\cos(\lambda z+\delta_\lambda^1)d\lambda \tag{1.133}$$

$$\Rightarrow g_\phi=\sum_{k=-\infty}^{\infty}\sin(k\Phi+\alpha_k^1)\int_0^{\infty}\pi_k(\lambda)\{\frac{k}{\rho}I_k(\lambda\rho)-k\lambda I_\lambda^{'}(\lambda\rho)\}\cos(\lambda z+\delta_\lambda^1)d\lambda$$

$$-\sum_{k=-\infty}^{\infty}\cos(k\Phi+\alpha_k^3)\int_0^{\infty}\lambda\omega_k(\lambda)I_\lambda^{'}(\lambda\rho)\cos(\lambda z+\delta_\lambda^3)d\lambda$$

$$+\frac{1}{\rho}\sum_{k=-\infty}^{\infty}(-k)\sin(k\Phi+\alpha_k^2)\int_0^{\infty}\psi_k(\lambda)I_k(\lambda\rho)\cos(\lambda z+\delta_\lambda^2)d\lambda \tag{1.134}$$

For the last component of the velocity,

$$\frac{\partial\Pi}{\partial z}=\sum_{k=-\infty}^{\infty}\cos(k\Phi+\alpha_k^1)\int_0^{\infty}\pi_k(\lambda)I_k(\lambda\rho)(-\lambda)\sin(\lambda z+\delta_\lambda^1)d\lambda \tag{1.135}$$

$$\rho\frac{\partial}{\partial\rho}(\frac{\partial\Pi}{\partial z}) = \sum_{k=-\infty}^{\infty}\cos(k\Phi+\alpha_k^1)\int_0^{\infty}\pi_k(\lambda)I_k^{'}(\lambda\rho)(-\lambda^2\rho)\sin(\lambda z+\delta_\lambda^1)d\lambda \tag{1.136}$$

$$\frac{\partial\Psi}{\partial z} = \sum_{k=-\infty}^{\infty}\cos(k\Phi+\alpha_k^2)\int_0^{\infty}\psi_k(\lambda)I_k(\lambda\rho)(-\lambda)\sin(\lambda z+\delta_\lambda^2)d\lambda \tag{1.137}$$

$$\Rightarrow g_z = \sum_{k=-\infty}^{\infty}\cos(k\Phi+\alpha_k^1)\int_0^{\infty}\pi_k(\lambda)\{-\lambda I_k(\lambda\rho)-\lambda^2\rho I_k^{'}(\lambda\rho)\}\sin(\lambda z+\delta_\lambda^1)d\lambda$$

$$+\sum_{k=-\infty}^{\infty}\cos(k\Phi+\alpha_k^2)\int_0^{\infty}\psi_k(\lambda)I_k(\lambda\rho)(-\lambda)\sin(\lambda z+\delta_\lambda^2)d\lambda \tag{1.138}$$

For the pressure, we obtain

$$p = 2\mu\sum_{k=-\infty}^{\infty}\cos(k\Phi+\alpha_k^1)\int_0^{\infty}\pi_k(\lambda)(\lambda^2)I_k(\lambda\rho)\cos(\lambda z+\delta_\lambda^1)d\lambda \tag{1.139}$$

In order to match the boundary conditions, we must match the corresponding velocities. Here we choose to transform

$$\begin{aligned} g_x &= g_R\cos\Phi - g_\Phi\sin\Phi \\ g_y &= g_R\sin\Phi + g_\Phi\cos\Phi \\ g_z &= g_z \end{aligned} \tag{1.140}$$

After transforming and rearranging, the boundary conditions can now be satisfied by comparing term by term in the Fourier sum. We get three different solutions for three possible directions of the particle.

Validation of CFD code implemented in OpenFOAM

The cfd code which is implemented in the open source software OpenFOAM is validated with the experimental results of Hampton et al. (1997) and also the personal code of Miller and Morris (2005). In either of the above works the suspension flows through a pipe with the suspended solids volume fraction being 0.3. Grid independence tests are also conducted with two different grid sizes, Grid A contains 189600 mesh cells whereas Grid B has 379200 cells. The figure given below gives a comparison of the experimental, theoretical and the current works.

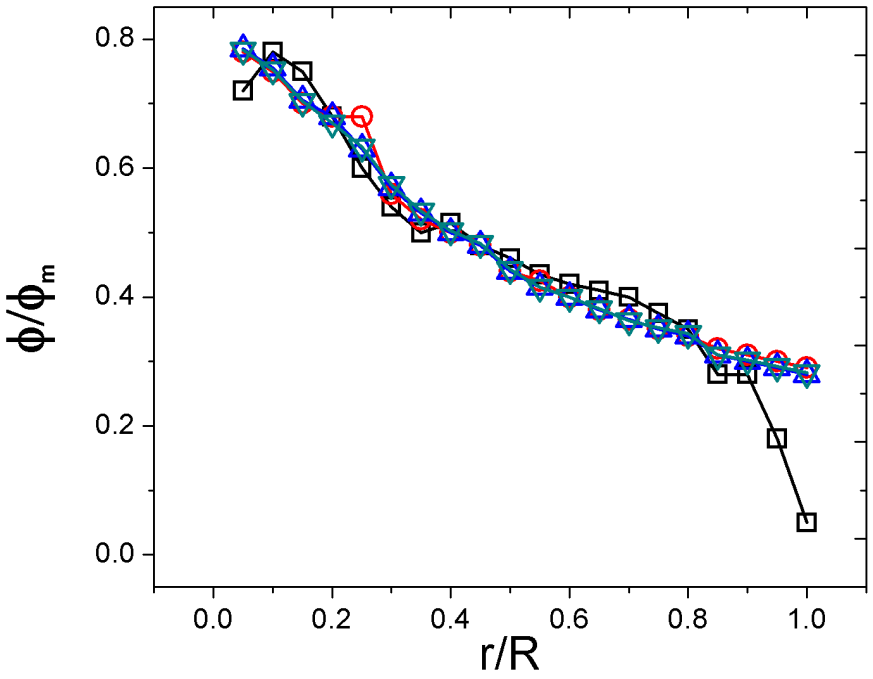

Fig: 30% suspension steady state concentration profile. Open squares represent the experimental work of Hampton et al. (1997), open circles indicate Miller and Morris (2005), open triangles are with present code Grid A and open inverted triangles are with Grid B (present code).

List of Symbols

a	radius of particle
d	mean interparticle separation
g	acceleration due to gravity
$\mathscr{G}$	Green's function for the Stokes equation
L	length of the cylinder
m	mass of the particle
m_B	buoyancy corrected mass of the particle
n	number of particles
n_0	average particle concentration
n_p	number of particles at steady state
N_0	number of particles at t = 0
R	radius of the cylinder
Re_f	flow based Reynolds number
Re_p	particle based Reynolds number
u_0	settling velocity of the particle
u_f	floating velocity of the particle
$u_{r,}$	radial velocity of the particle
u_θ	and angular velocity of the particle
s_i	particle surface
V	volume of spherical particle

μ	viscosity of the fluid
ν	kinematic viscosity of the fluid
Ω	rotational velocity of the cylinder
ρ_f	density of the fluid
ρ_p	density of particle
ρ_{p2} , ρ_{p1}	density of two types of particles in case of bidensity system